AMPEROMETRIC DETECTION OF NITRITE USING Co_3O_4 THIN FILM

by

ARIEL MPUKUTA NDALA

Thesis submitted in fulfilment of the requirements for the degree

Masteri n Engineering in Chemical Engineering

in the Faculty of Engineering and the Built Environment

at the Cape Peninsula University of Technology

Supervisor: Dr. Mahabubur Rahman Chowdhury
Co-supervisor: Dr. Christopher Edozie Sunday

Bellville
November 2021

DECLARATION

I, Ariel Mpukuta Ndala, declare that the contents of this thesis represent my own unaided work, and that the thesis/dissertation has not previously been submitted for academic examination towards any qualification. Furthermore, it represents my own opinions and not necessarily those of the Cape Peninsula University of Technology.

Signed: **Date: 3rd July 2021**

ABSTRACT

In this MSc thesis, Co_3O_4 thin film was prepared by metal-organic decomposition on FTO substrate and hydrothermal treatment in the presence of L-Arginine. The conditions for hydrothermal treatment were optimized with respect to time, temperature, L-Arginine concentration, and pH. The L-Arginine-treated Co_3O_4 thin film (L-Arginine/Co_3O_4/FTO) was used for the electrochemical detection of nitrite under neutral pH condition. Several physical (i.e., XRD, XPS, SEM, and Raman spectroscopy) and electrochemical (i.e., CV, CA, and EIS) techniques were used to elucidate the role and effect of L-Arginine on Co_3O_4 film as well as to determine the sensor performance. It is demonstrated that the L-Arginine-treated electrode exhibited enhanced electrochemical nitrite detection compared to pristine Co_3O_4 electrode. The proposed nitrite sensor also showed a combination of ultralow limit of detection (1.95 nM), fast response time (< 2 s), wide linear range (10 – 16 000 µM), high sensitivity (158 µM/mM.cm^{-2}) and selectivity compared to the reported literature.

Key Words: Amino acid functionalisation; Co_3O_4; Electrochemical sensor; L-Arginine; Nitrite detection; Nitrogen doping.

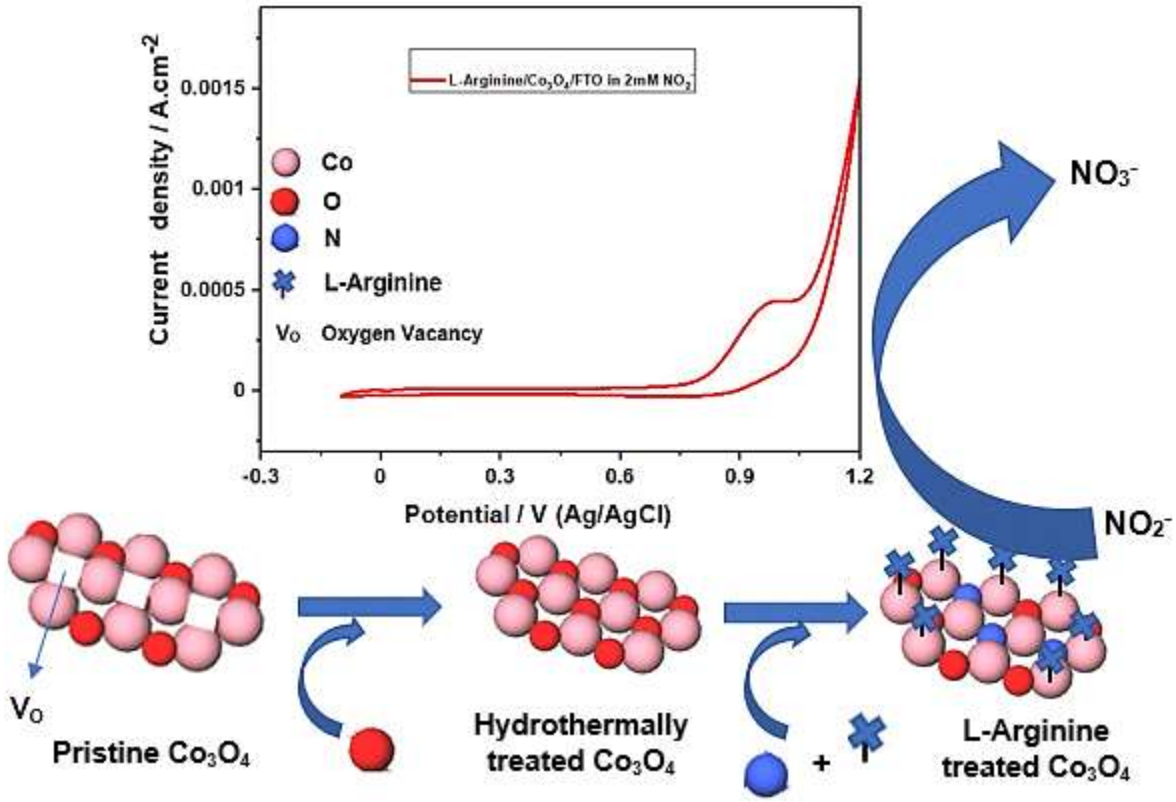

<u>Graphical Abstract</u>

ACKNOWLEDGEMENTS

I wish to thank:

- Dr. Mahabubur Rahman Chowdhury for all his guidance, support, and advice.
- Dr. Christopher Edozie Sunday for his guidance and help.
- Prof Sekhar Ray and Dr. Jessica Chamier for their feedback on my proposal and research paper.
- All research group members of the Functional Materials for all the valuable discussion and exchange of ideas during this project.

The financial assistance of the National Research Foundation and Cape Peninsula University of Technology towards this research is acknowledged. Opinions expressed in this thesis and the conclusions arrived at, are those of the author, and are not necessarily to be attributed to the National Research Foundation or Cape Peninsula University Technology.

DEDICATION

One love, one heart

To my family

PUBLICATION

- Ndala, A., Itota, B., Chamier, J., Ray, S., Sunday, C. & Chowdhury, M. 2021. Novel ($CH_6N_3^+$, NH_3^+)-functionalized and nitrogen doped Co_3O_4 thin film electrochemical sensor for nanomolar detection of nitrite in neutral pH. *Electrochimica Acta*, 388:138556 (IF: 6.901). Doi: 10.1016/j.electacta.2021.138556.

Table of Contents

List of Figures

List of Schemes

List of Tables

ABBREVIATIONS AND ACRONYMS

ACS	American Chemical Society
C	Concentration range
CA	Chronoamperometry
CL	Chemiluminescence
CNT	Carbon nanotube
CPE	Constant phase element
CT	Charge transfer
CSD	Chemical solution deposition
CV	Cyclic voltammetry
DI	Deionized water
DL	Double-layer
ECSA	Electrochemical surface area
EIS	Electrochemical impedance spectroscopy
FET	Field-effect transistor
Fig.	Figure
FTO	Fluorine doped tin oxide
GCE	Glassy carbon electrode
Hetero.	Heterogeneous
HRP	Horseradish peroxidase
HT	Hydrothermally treated
IEC	Ion-exchange chromatography
Int.	Interface
IUPAC	International Union of Pure and Applied Chemistry
LCMC	Long-chain metal carboxylate

LOD	Limit of detection
Log.	Logarithm
MOD	Metal-organic decomposition
PBS	Phosphate buffered saline
QD	Quantum dot
rGO	Reduced graphene oxide
S	Sensitivity
SEM	Scanning electron microscopy
Surf.	Surface
UNISA	University of South Africa
W	Warburg
WHO	World Health Organization
XPS	X-ray photoelectron spectroscopy

CHAPTER 1: INTRODUCTION

1.1. Project background

Nitrite is predominantly used as corrosion inhibitor (Wachter, 1945), bleaching agent (Hosoya, 1999), and food additive (Honikel, 2008). Recently, researchers have reported the environmental risks (Kroupova, Machova and Svobodova, 2005) and health implications (Brender *et al.*, 2004) of human exposure to elevated concentrations of nitrite. The World Health Organization (WHO) has set the maximum limit of nitrite in drinking water at 65 µM (Sayato, 1989). Quantitative analysis of nitrite is therefore necessary for quality control using an adequate detection method. Various techniques for the determination of nitrite, including chromatography (Li, Meininger and Wu, 2000), catalytic-spectrophotometry (Mubarak *et al.*, 2007), chemiluminescence (He *et al.*, 2007), and so forth have been implemented. These methods require expensive instrumentation and skilled personnel to operate. Electrochemical techniques are cost-effective, simple, effective and favour highly sensitive and selective detection of nitrite (Wang and Hu, 2009).

Owing to their small size (1 – 100 nm), conductivity, and chemical reactivity, nanomaterials have been widely used in catalysis (Rossi *et al.*, 2014) and sensors (Bochenkov and Sergeev, 2007). Over the past two decades, scientists have developed a panel of electrochemical nitrite sensors using carbon (Chen *et al.*, 2008), enzymes (Astier *et al.*, 2005), metals (Cui *et al.*, 2007), metal oxides (Ma *et al.*, 2017), and polymers (Lamine *et al.*, 2020) as modifiers. Among the metal oxide modifiers, cobalt oxide (Co_3O_4) is of interest in this study because of its mixed valance state, availability, chemical stability, high electrocatalytic activity, selectivity, and extensive application in different areas of research and industry, such as catalysis (Gangarajula and Gopal, 2012), lithium batteries (Xu *et al.*, 2009), and sensors (Cao *et al.*, 2006). Spinel Co_3O_4, written as $Co^{2+}[Co^{3+}]_2O_4^{2-}$, contains Co^{2+} and Co^{3+} ions located each in the tetrahedral and octahedral sites, respectively (Roth, 1964). Tuning the ratio of Co^{3+}/Co^{2+} provides the means to tailor reactive properties of cobalt oxide (Hou *et al.*, 2019). Also, the synthetic approach of cobalt oxide materials has profound influence on their performance (Zhu *et al.*, 2013). Electrodeposition (Nakaoka, Nakayama and Ogura, 2002), atomic layer deposition (Han *et al.*, 2012), and plasma sputtering (Schumacher *et al.*, 1990) are among the numerous preparation methods for the direct growth of Co_3O_4 nanomaterials on conductive substrates. However, the non-uniformity of the plated material in electrodeposition, and high vacuum requirement in atomic layer deposition and plasma sputtering have prompted the chemical solution deposition of Co_3O_4 (Jeon *et al.*, 2015) on substrates for catalytic oxidation processes. Based on different film morphology requirements, three variants of chemical solution deposition technique, i.e., sol-gel method, chelate process, and metal-organic decomposition (MOD) can be distinguished (Biswas and Su, 2017). Of these three methods, MOD is the simplest as no precise control over hydrolysis and condensation is needed during growth of nanoparticles. The technique has been widely used for the synthesis of ferroelectric materials (Schwartz, 1997). To improve their electronic conductivity and extend their application for sensors, MOD-grown thin films of doped Co_3O_4 have been synthesized recently for the detection of biomarkers, such as glucose (Chowdhury, Ossinga, *et al.*, 2017), . However, the doping method used in these studies was limited to the incorporation of cationic impurities into the cobalt oxide precursor solution, and the possibility of altering the surface properties of MOD-synthesized Co_3O_4 thin films was not explored. Recently, Plasma assisted nitrogen doping of MOD-synthesized CuO/Cu_2O thin film has been achieved and the beneficial role of nitrogen doping in glucose sensing was highlighted (Palmer *et al.*, 2021). However, plasma-assisted surface treatment requires high vacuum equipment, which increases capital cost.

Several efforts have been made to functionalize metal oxide surfaces by organic ligands to improve their electrochemical performance for sensing applications (Hua, Swihart and Ruckenstein, 2005). Yet, most of those organic ligands used for surface functionalization are toxic and possess only one type of functional groups. Amino acids are eco-friendly, benign and have both amino and carboxyl groups in their molecular structure. These desirable characteristics, among others, have promoted research activities in amino acid-functionalized metal oxides (Patel, Chang and Lee, 2009). L-Arginine is an attractive surface modifier as it is green, non-toxic, water soluble, and its side chain (guanidinium, $pK_A = 12.5$) has a delocalized positive charge which remains protonated over a wide pH range (Lewis *et al.*, 2016). The delocalized positive charge on the guanidino group of L-arginine enables the formation of multiple hydrogen bonds and has favoured the use of guanidinium-bearing molecules as anion receptors (Houk, Tobey and Anslyn, 2005). The nitrogen content in L-Arginine molecule is 32.1 % (w/w), which makes L-Arginine a nitrogen-rich source for chemical doping (Kim *et al.*, 2018). Recently, Li and co-authors (Li *et al.*, 2020) confirmed the electron doping of a MoS_2 monolayer (n-type semiconductor) using Arginine. In other words, the amino acid induced n-type functionalization of the MoS_2 monolayer. The modified MoS_2 monolayer showed good performance as field effect transistor (FET). Bora and co-authors (Bora *et al.*, 2011) have converted an undoped hematite film into faceted superstructures with excellent photocurrents after hydrothermal treatment of the film in aqueous solution of $FeCl_3{\cdot}6H_2O$ and L-Arginine.

However, Bora and co-authors, like others (Cao *et al.*, 2008), only highlighted the role of L-Arginine as a size and morphology director of nanostructures during the hydrothermal reaction. Moreover, the possibility of L-Arginine dissociation during hydrothermal treatment and its effect on the chemical and physical properties of the material were not analysed in depth.

1.2. Project novelty, aim, and objectives

In this study, we successfully ($CH_6N_3^+$, NH_3^+)-functionalized and nitrogen-doped a pristine MOD-derived Co_3O_4 thin film in one-pot hydrothermal treatment with L-Arginine. The aim was to improve the electrochemical properties of the film via a new platform for post-deposition element doping and surface functionalization of metal oxides. To the best of our knowledge, this is the first study to show that: a) hydrothermal treatment of Co_3O_4 thin film in the presence of L-Arginine can alter the physico-electrochemical properties of the film by simultaneous surface functionalization and nitrogen doping and b) the functionalized Co_3O_4 thin film exhibits enhanced electrochemical behaviour towards nitrite detection in neutral pH. The specific objectives were then to:

1. To synthesize Co_3O_4 thin film with rich oxygen vacancies;
2. To study the effect of hydrothermal treatment with and without L-Arginine on the physico-electrochemical properties of the Co_3O_4 thin film;
3. To determine the optimum treatment conditions of the film in the presence of L-Arginine;
4. To demonstrate the application of L-Arginine treated Co_3O_4 thin film for nitrite detection in neutral pH.

1.3. Overview of thesis

Chapter 2 discusses the current techniques for nitrite detection, provides a brief review of previously reported Co_3O_4-based electrochemical nitrite sensors, and describes the various stages involved in the deposition and post-deposition of a MOD-derived film. Chapter 3 encompasses experimental details about the synthesis of Co_3O_4 precursor, the deposition and post-deposition annealing of Co_3O_4 precursor on fluorine-doped tin oxide (FTO) substrate, the hydrothermal treatment of pristine Co_3O_4 thin film in the presence and absence of L-Arginine, and the optimization of hydrothermal treatment conditions. The chapter finally closes with a concise description of each characterization technique used in this study. Chapter 4 compiles the results and discussion of all the performed experiments except for those of the optimization studies, which have been relegated to APPENDIX A. Chapter 5 summarizes this thesis and suggests future research directions.

CHAPTER 2: LITERATURE REVIEW

2.1. Nitrite detection methods

Current techniques for nitrite detection include spectrophotometry, chromatography, capillary electrophoresis, spectrofluorometry, electrochemistry, and electro/chemiluminescence (Q. H. Wang *et al.*, 2017). A summary discussion of each technique is given in Table 2.1 below.

Table 2.1. Comparative study of current techniques for nitrite detection (Q. H. Wang *et al.*, 2017)**,** (Yilong, Dean and Daoliang, 2015)

Detection methods	**Detection principle**	**Advantages**	**Shortcomings**
Spectrophotometry	The absorbance of the reaction product (measured by UV/VIS detectors) can be correlated with nitrite concentration.	Quick analysis ability, and easy to use.	Carcinogenicity of some reagents, derivitization (samples cannot be recovered), and interferents (Cu^{2+}, Fe^{3+}, S^{2-}, Cl^{-}, and I^{-}).
Chromatography	Here, the sample is injected into a glass tube containing an absorbent through which each component of the sample moves at different speeds. UV/VIS detectors are then used to probe the various band colors produced.	Highly selective compared to spectroscopic methods, direct sample analysis using IEC, and simultaneous determination of two or more analytes.	Sample derivitization using GC, need for skilled individuals due to process complexity, and high cost of equipment.
Capillary electrophoresis	Detection occurs using UV/VIS detectors after a separation stage. The separation process is based on differences in ionic mobility resulting	Higher separation efficiency than chromatography, short run time, small injection volumes of samples, and	Confined diameter of the capillary tube, and high risk of contamination to proteinaceous materials.

	from an applied electric field.	simultaneous analysis of various chemical species.	
Spectrofluorometry	The fluorescence intensity resulting from the reaction between fluorescent probes and nitrite is related to the nitrite concentration.	Selective detection of nitrite is feasible based on its chemical specificity to undergo nitrosation and diazotization.	Carcinogenicity of N-nitroso derivatives, and fluoerescence self-quenching of probes due to stokes shift.
Electrochemistry	Detection takes place by relating the nitrite concentration in the redox reaction to current (amperometry), potential (potentiometry), or impedance (impedimetry). .	Low cost, simplicity, effectiveness, and portability of electroanalytical devices. Ease of electrode miniaturization and availability of research data using amperometry.	Potential drift and unfeasible electrode miniaturization using potentiometry. Lack of extensive research data and complexity of data interpretation using impedimetry.
Chemiluminescence (CL)	The chemiluminescence intensity is proportional to the concentration of nitrite.	Simple, cost-effective, and controllable CL emission rate.	High temperature requirement, tedious procedure, and lack of direct sample analysis.
Electrochemiluminescence	detection of nitrite is based on the quenching effect of nitrite on the anodic ECL intensity of semiconductor quantum dots (QDs).	Simple instrumentation.	Toxicity of QDs

Comparing all these techniques, electrochemical determination of nitrite is a convenient and cost-effective option for developing efficient nitrite sensors as the technique provides electroanalytical devices that are easily portable and suitable for field use. Of all three electrochemical methods mentioned for detection of nitrite (i.e., amperometry, potentiometry, and impedimetry), the amperometric method is the most relevant to this study because of feasible electrode miniaturization and availability of research data.

2.2. Performance characteristics of amperometric nitrite sensors

The criteria for performance evaluation of amperometric nitrite sensors are shaped by:

- **Sensitivity**

Sensitivity can be understood as the ratio of output signal (faradaic current) to measured variable (concentration of analyte). The slope of the analytical calibration curve (see Figure 1) is a measure of the electrode sensitivity (Butler, Laqua and Strasheim, 1986). Sensitivity can be affected by the pH of the solution (i.e., it can influence the formation of un/protonated species and promote certain redox processes at the electrode surface) and temperature (i.e., it can speed up the kinetics and thermodynamics of the reactions occurring at the electrode surface). A constant temperature of 25 ºC is recommended for electrode characterization.

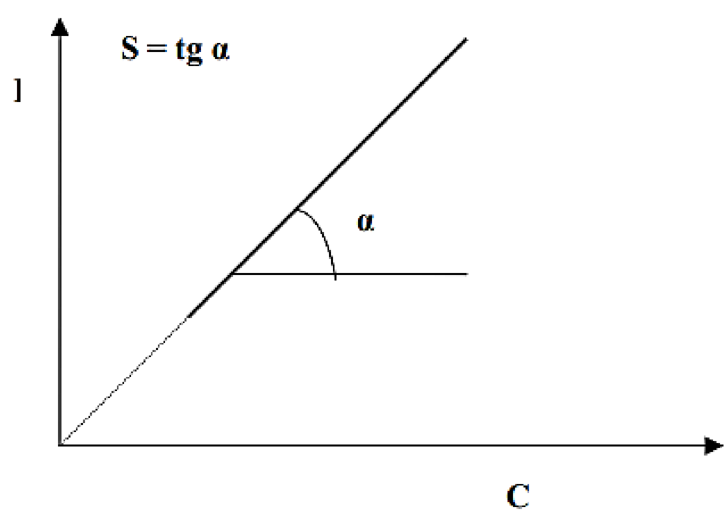

Figure 2.1. Analytical calibration curve (Najem, 2004)

- **Linear concentration range**

This can refer to the range of concentration of the analyte within which the electrode sensitivity is measured and constant with a specific variation (usually ± 5%). Factors that influence the reproducibility of the linear range include stirring rate, solution composition, solution pH, temperature, composition of the solution where the electrode was exposed before the measurement, and the preconditioning of the amperometric electrode (Coşofreţ and Buck, 2018).

- **Selectivity**

Selectivity can be defined as the ability of the electrode to respond specifically to a group of analytes or a single analyte. There are two types of interferences that affect amperometric electrodes (Najem, 2004): electrode/electrochemical interferences point to substances of which current responses are similar to that of the target analyte or electrolyte present at high concentration level; chemical interferences refer to species that interact with the target analyte so as to decrease its activity or apparent concentration or substances that interact with the electrode surface.

- **Limit of detection**

The limit of detection (LOD) is defined by the American Chemical Society (ACS) and International Union of Pure and Applied Chemistry (IUPAC) as the lowest quantity or concentration of the analyte that can be reliably detected with a given analytical method (Butler, Laqua and Strasheim, 1986), (McCormick and Karger, 1980). LOD can be influenced by sensitivity, background noise, and interferences.

- **Response time**

The response time has to do with the length of time taken for the electrode to react or respond to the injection of the target analyte into the electrochemical system during potentiostatic current-time analysis. The following are true about the response time of amperometric electrodes (Najem, 2004):

a) It hinges on the kinetics of the reactions that take place at the electrode surface;
b) It increases with a decrease in concentration of the analyte of interest;
c) It is influenced by the presence of other interfering species.

2.3. Structure and properties of Co_3O_4

Co_3O_4 has a normal spinel structure written as $Co^{2+}[Co^{3+}]_2O_4^{2-}$ (space group $Fd\bar{3}m$) and a close-packed face-centred cubic (fcc) lattice formed by oxygen anions (see Figure 2.2). Co^{2+} and Co^{3+} are situated in interstitial tetrahedral (8*a*) and octahedral (16*d*) sites, respectively. Both cobalt oxidation states have five degenerate atomic *d* orbitals split into e_g and t_{2g} groups. Previous studies have linked the ratio of Co^{2+}/Co^{3+} to the electro-catalytic activity of Co_3O_4 (J. Wang *et al.*, 2017), which hinges on different preparation methods of the p-type semiconductor (Zhu *et al.*, 2013).

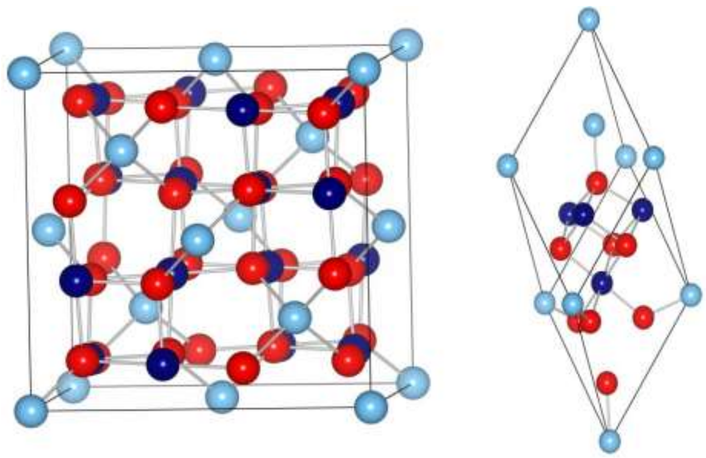

Figure 2.2. Simplified picture of unit (on the left) and primitive (on the right) cells of Co_3O_4. Co^{2+}, Co^{3+}, and O^{2-} are represented by light cyan, navy blue, and red balls, respectively (Chen, Wu and Selloni, 2011)

Co^{2+} and Co^{3+} possess d7 and d6 electronic configurations, respectively, as shown in Figure 2.3. All the electrons in the *d* orbitals of Co^{3+} are paired (low spin) while those in the *d* orbitals of Co^{2+} contain 3 unpaired electrons (high spin). Co_3O_4 is a semiconductor with p-type conductivity and band gap around 1.6 eV (Shinde *et al.*, 2006). The p-type conductivity can be improved by increasing the number of charge carriers (holes in this case) through element doping.

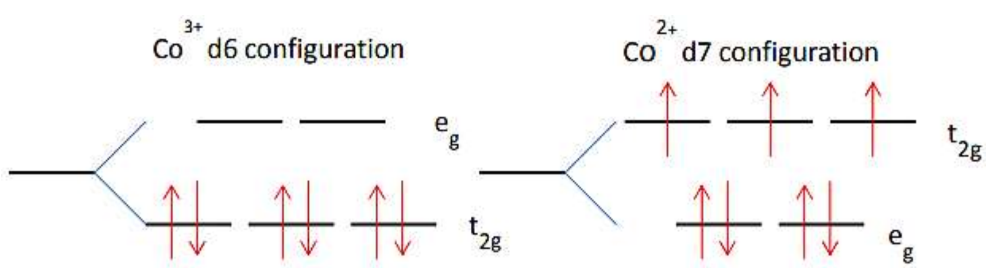

Figure 2.3. Atomic *d* orbitals of Co^{3+} (on the left) and Co^{2+} (on the right) (Chen, Wu and Selloni, 2011)

The valence band of p-type semiconductor oxides is populated with electrons from the fully occupied 2*p* orbitals of oxygen ions (O^{2-}) whereas their empty conduction band is made of orbitals of metal cations. When a cationic impurity (with less valence electrons) substitutes a metal cation (with more valence electrons) of a p-type semiconductor oxide, it increases the number of holes and therefore the conductivity of the p-type semiconductor oxide and introduces new electronic states that fall into the band gap close to the conduction band edge (the band gap is reduced as a result). Similarly, heteroatomic doping using, e.g., nitrogen will substitute oxygen in the anionic sub-lattice of the p-type semiconductor oxide, thereby increasing the number of holes (nitrogen has one valence electron less than oxygen), inserting new states not far from the valence band edge, and reducing the band gap.

2.4. Co_3O_4-based amperometric nitrite sensors

Up to date, the field of Co_3O_4-based amperometric nitrite sensors is still under-explored judging by the insignificant number of existing reports, as summarized in Table 2.2 and discussed in the next paragraphs of this section.

Haldorai and co-authors (Haldorai *et al.*, 2016) hydrothermally prepared an enzyme-free composite of Co_3O_4 nanospindles and reduced graphene oxide (rGO), of which a suspension was drop-casted onto GCE (Co_3O_4/rGO/GCE). The sensor showed high sensitivity (2065 µA/mM) attributed to the excellent electrocatalytic activity of Co_3O_4 and large surface area of rGO.

Liu and co-authors (Liu *et al.*, 2017) developed a nitrite biosensor using a suspension of horseradish peroxidase (HRP) immobilized on porous and rGO-entrapped Co_3O_4 hexagonal nanosheets drop-casted onto GCE (Co_3O_4-HRP/rGO/GCE). The porous Co_3O_4 hexagonal nanosheets were synthesized via hydrothermal reaction followed by calcination. The biosensor exhibited good performance, such as a wide linear range (1-5400 µM) due to high concentration of HRP, porous Co_3O_4, and high surface area of rGO.

Sudha and co-authors (Sudha, Mohanty and Thangamuthu, 2018) synthesized Co_3O_4 disordered circular sheet via precipitation followed by drop casting onto GCE and thermal drying (Co_3O_4/GCE). The proposed sensor was highly selective towards nitrite in the presence of twelve interfering ions.

Zhao and co-authors (Zhao *et al.*, 2019) fabricated a nitrite sensor with Co_3O_4 nanocrystals at its core. The Co_3O_4 nanocrystals were synthesized using precipitation and subsequent annealing.

The synergistic combination of Co_3O_4 nanocrystals, rGO, and carbon nanotubes was dropped onto GCE (Co_3O_4-rGO/CNTs/GCE) and resulted in a low limit of detection (0.016 µM).

Most recently, Qiu and co-authors (Qiu *et al.*, 2019) prepared porous nanododecahedron of Co_3O_4 and carbon composite via precipitation followed by pyrolysis. The nanocomposite was drop-casted onto GCE to complete the electrode fabrication process (Co_3O_4/C/GCE). This electrode achieved a nanomolar limit of detection (1.21 nM) and a wide detection range (0.002-8000 µM) owing to the synergy of Co_3O_4 and carbon.

Table 2.2. Summary of reported literature on Co_3O_4-based amperometric nitrite sensors

Modified Electrode	Preparation methods of Co_3O_4	Electrode modification technique	C/µM	S/µA mM^{-1}	LOD/µM	Reference
Co_3O_4/rGO/GCE	Hydrothermal	Drop-cast	1 - 380	2065	0.14	(Haldorai *et al.*, 2016)
Co_3O_4-HRP/rGO/GCE	Hydrothermal	Drop-cast	1 - 5400	1.67	0.21	(Liu *et al.*, 2017)
Co_3O_4/GCE	Precipitation	Drop-cast	6.6 - 3000	0.318	0.22	(Sudha, Mohanty and Thangamuthu, 2018)
			3000 - 13830	0.6		
Co_3O_4-rGO/CNTs/GCE	Precipitation	Drop-cast	0.1 - 8000	80	0.016	(Zhao *et al.*, 2019)
			8000 - 56000	30		
Co_3O_4/C/GCE	Precipitation	Drop-cast	0.002 - 8000	7.35	1.21×10^{-3}	(Qiu *et al.*, 2019)

In case of Co_3O_4-HRP/rGO/GCE, the enzymatic modification promotes high selectivity though it is often avoided due to instability and environment-sensitive bioactivity of enzymes. Also, most enzymes used in nitrite biosensors catalyse nitrite electroreduction (Salimi, Hallaj, *et al.*, 2008) of which the current signal may suffer from interferences caused by NO_3^- and O_2.

The preparation methods of Co_3O_4 nanomaterials for nitrite detection in all the cited studies are limited to precipitation and hydrothermal synthesis with or without thermal post-treatment. These synthetic strategies allow the production of Co_3O_4 nanostructures with various morphologies but consume a lot of reagents.

The extensive use of glassy carbon as substrate can be associated with its large-scale production, which is costly (Sharma, 2018). Drop casting is the only electrode modification technique used for Co_3O_4-based electrode fabrication in the reported literature. However, this method lacks stability, control over film thickness, reproducibility, and prevents homogeneous coating compared to the direct growth technique for electrode modification (Lu *et al.*, 2013).

2.5. Mechanism of nitrite electro-oxidation

For sensing applications, electrochemical oxidation of nitrite is usually preferred to avoid interferences (nitrate and molecular oxygen) and complex reaction mechanism associated with the cathodic detection of nitrite (Wang, Laborda and Compton, 2012).

According to the reported literature (Wang, Laborda and Compton, 2012), nitrite electro-oxidation occurs via a second-order catalytic mechanism involving an electron transfer (E) followed by a chemical reaction (C), as illustrated in Equation 2.1-2.2.

$$NO_2^- \underset{k_{Red}}{\overset{k_{Ox}}{\rightleftarrows}} NO_2 + e^- \tag{2.1}$$

$$2\,NO_2 + H_2O \xrightarrow{k_{EC}} NO_3^- + NO_2^- + 2\,H^+ \tag{2.2}$$

This type of mechanism is referred to as an EC mechanism. When only the electron-transfer step is involved, it is known as an E mechanism (Figure 2.4a). If the rate constant of Equation 2.2 (k_{EC}) is very large ($k_{EC} \gg k_{Red}$), the chemical step suppresses the reverse electron transfer as it consumes NO_2 immediately after it is formed. In this case, the resulting cyclic voltammogram will resemble Figure 2.4b.

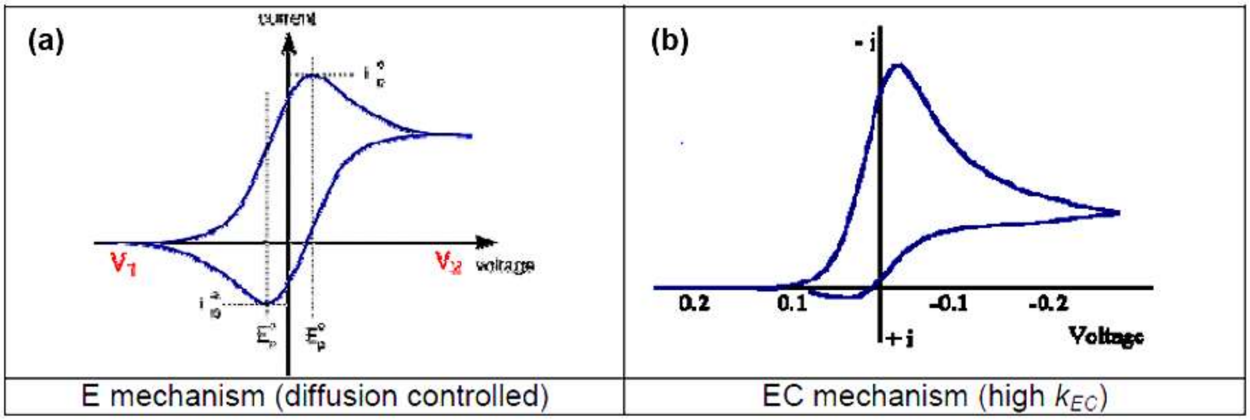

Figure 2.4. Cyclic voltammograms of (a) E and (b) EC mechanisms (Fisher, 2010)

If, however, k_{EC} is low, CV will depend on the scan rate such that high scan rates (>10 mVs^{-1}) will be needed to observe the reverse electron transfer, as seen in Figure 2.5.

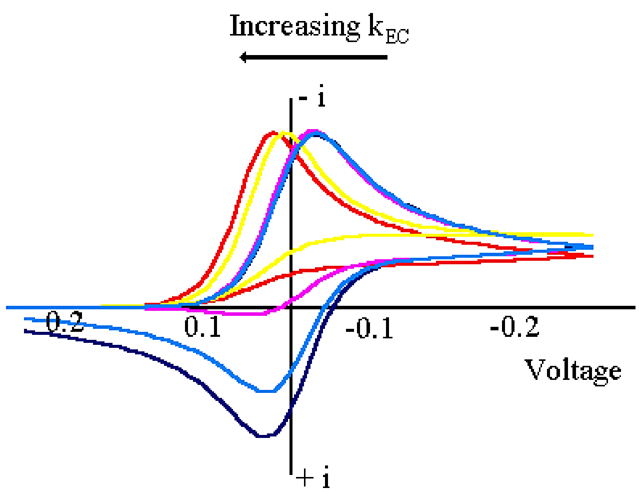

Figure 2.5. Cyclic voltammogram at various scan rates: case of low k_{EC} (Fisher, 2010)

Table 2.3 compiles the proposed mechanisms for nitrite electro-oxidation at Co_3O_4-based electrodes under various pH conditions. The pH influence is seen on the electrochemically oxidized product of Co_3O_4.

At highly basic pH, Co_3O_4 is first electro-oxidized to CoOOH, which then reacts with nitrite to regenerate Co_3O_4 and yield nitrate (Haldorai *et al.*, 2016). In acidic conditions, however, Co_3O_4

oxidizes to Co^{3+} with the formation of water molecules. These reaction products then interact with nitrite to regenerate Co_3O_4 and form NO_2, which further undergoes disproportionation to finally produce NO_3^- (Qiu *et al.*, 2019). The acidic pH threshold for this mechanism to hold true is 3.3, at and below which nitrite exists predominantly as unstable HNO_2 (pKa = 3.3 at 25 ºC) (Wang, Laborda and Compton, 2012) leading to a different reaction pathway (Braida and Ong, 2000).

Furthermore, the reported reaction pathway in basic conditions follows an E mechanism whereas that at acidic pH-value is in good agreement with the second-order catalytic mechanism. This discrepancy results from different cobalt oxidation states between the electro-oxidized products of Co_3O_4 in both pH conditions. The basic electro-oxidized product CoOOH may contain Co^{3+} and Co^{4+} oxidation states (Morishita *et al.*, 2009). The latter is a more powerful oxidizing agent that can convert nitrite directly into NO_3^- rather than NO_2 as is the case with Co^{3+} in acidic medium.

Table 2.3. Mechanism of nitrite electro-oxidation at Co_3O_4-modified electrodes under various electrolyte pH

Electrolyte pH	Mechanism	Reference
Basic	$OH^- + H_2O + Co_3O_4 \rightarrow 3\ CoOOH + e^-$ $6\ CoOOH + NO_2^- \rightarrow 2\ Co_3O_4 + NO_3^- + 3\ H_2O$	(Haldorai *et al.*, 2016)
Near-neutral	$2\ Co_3O_4 + 2\ NO_2^- \leftrightarrow 2\ [Co_3O_4(NO_2^-)]$ $2\ [Co_3O_4(NO_2^-)] \leftrightarrow 2\ Co_3O_4 + 2\ NO_2 + 2e^-$ $2\ NO_2 + H_2O \leftrightarrow NO_3^- + NO_2^- + 2\ H^+$ $NO_2^- + H_2O \leftrightarrow NO_3^- + 2\ H^+ + 2e^-$	(Sudha, Mohanty and Thangamuthu, 2018), (Zhao *et al.*, 2019)
Acidic	$Co_3O_4 + 8\ H^+ \rightarrow 3\ Co^{3+} + 4\ H_2O + e^-$ $3\ Co^{3+} + 4\ H_2O + NO_2^- \leftrightarrow Co_3O_4 + NO_2 + 8\ H^+$ $2\ NO_2 + H_2O \leftrightarrow NO_3^- + NO_2^- + 2\ H^+$	(Qiu *et al.*, 2019)

In near-neutral pH environments, nitrite electro-oxidation at Co_3O_4 modified electrode has been reported previously to proceed by the formation of an adduct between Co_3O_4 and nitrite (Sudha, Mohanty and Thangamuthu, 2018), (Zhao *et al.*, 2019). This reaction is followed by an inner-sphere electron transfer as opposed to outer-sphere electron transfers (i.e., no complex formation occurs for the electron-transfer reaction) in acidic and basic conditions. Yet, one aspect of the complexation reaction remains unexplored, i.e., it is unclear whether nitrite bonds to Co^{2+} or Co^{3+} oxidation state of Co_3O_4 for the formation of the adduct.

The amperometric detection of nitrite in neutral medium is of interest in this project for practical application of the proposed sensor in drinking water.

2.6. Metal-organic decomposition (MOD)

MOD is a straightforward chemical solution deposition (CSD) technique for precursor synthesis via the dispersion of long-chain metal carboxylates (LCMCs) such as metal neodecanoate and metal oleate into inert solvents (e.g., xylene, toluene, and hexane). These LCMCs can be synthesized through an ion-exchange reaction as previously reported (Park *et al.*, 2004). The bulky and nonpolar hydrocarbon chains of LCMCs cause steric hindrance and are responsible for their water-insensitivity and very low reactivity. Hence, a LCMC-based solution is a simple and noninteracting mixture (i.e., LCMCs do not undergo intermolecular interactions, chelation, hydrolysis, or condensation) for which change in process chemistry is limited to variations in solvent and solution concentration. MOD has been widely used for the synthesis of ferroelectric materials (Schwartz, 1997).

2.7. Coating techniques

A precursor solution can be transferred onto a substrate to produce a thin film (i.e., two-dimensional layer with thickness range below 1 micron (Abegunde *et al.*, 2019)) via three most widely used coating techniques, precisely spin-coating, dip-coating, and spray-coating (Biswas and Su, 2017), as illustrated in Figure 2.6. The following paragraphs will be discussing each of these coating strategies.

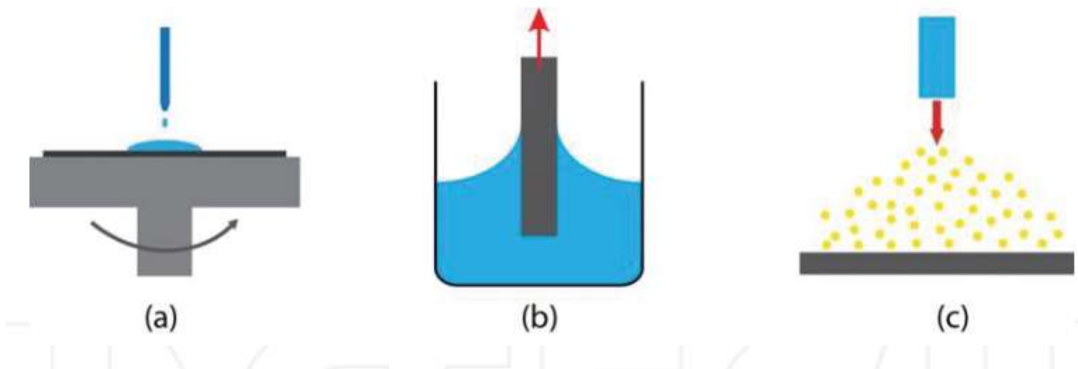

Figure 2.6. (a) Spin-coating, (b) Dip-coating, and (c) Spray-coating (Biswas and Su, 2017)

2.7.1. Spin-coating

Spin-coating is a simple and cost-effective process whereby a precursor solution is deposited onto a flat substrate that is held in place by vacuum chuck and spun at desired rotation speed and duration to produce a thin and uniform film after the excess liquid is evenly spread out from the substrate by centrifugal force. The film thickness depends on the solution viscosity, rotation speed, and spin time. The film thickness (t) varies proportionally with the reciprocal of the square root of the spin speed (ω) according the semi-empirical formula shown in Equation 2.3 (Willis, 2003).

$$t \propto \frac{1}{\sqrt{\omega}} \qquad (2.3)$$

The spin-coating technique has relatively low throughput and lacks flexibility in the choice of the substrate to be coated since it strictly requires smooth and planar surfaces.

2.7.2. Dip-coating

Contrastingly, one can choose various shaped substrates and needs no special equipment to undertake dip-coating. Hence, dip-coating is a flexible and inexpensive technique based on the immersion of a substrate into a precursor solution and its subsequent coating on both sides simultaneously upon withdrawal from the solution. The dip-coated substrate may present a non-uniform film thickness along the withdrawal direction due to the gravitational force acting on the entrained liquid film as the substrate is being removed from the coating fluid. The film thickness (t) is influenced, according to the Landau-Levich equation (see Equation 2.4) (Brinker *et al.*, 1991), by solution viscosity (η) and density (ρ), withdrawal speed (U), surface tension (γ), and gravity (g).

$$t = 0.94 \frac{\eta U^{2/3}}{\rho \gamma^{1/6} g^{1/2}} \tag{2.4}$$

Although dip-coating offers higher throughput than spin-coating, it is not suitable for application in cases where only one face of the substrate is required for thin-film deposition.

2.7.3. Spray-coating

Spray-coating involves the deposition of fine droplets of a coating solution on a substrate by an atomizer nozzle. Both nozzle and substrate can be stationary or one moving and the other static. The substrate can be at room temperature or above, and the atomization may be driven by an electrostatic field or a pressurized gas (Beckel *et al.*, 2007). The thickness and surface uniformity of the deposited film hinge on several spray-coating parameters such as flow rate, deposition time, nozzle-substrate distance, and substrate temperature. Spray-deposition enables uniform coating on substrates of different morphologies, but the process can be expensive depending upon the methods of atomization.

In the interest of depositing thin and uniform liquid film of Co_3O_4, spin-coating is a suitable and cost-effective technique for implementation to achieve such purpose.

2.8. Post-deposition annealing of MOD-derived liquid film

Schmidt (Schmidt, 1981) described several phenomena that occur during heat treatment of thin films prepared by the sol-gel process. Those phenomena include hydrolysis, drying, condensation, gelation, and densification. Excluding hydrolysis and condensation, similar processes can be deemed to occur during post-deposition annealing of MOD-grown thin films. One should recall that MOD-related precursors are not susceptible to hydrolysis or condensation.

Two essential phase transformation processes take place during heat treatment of a MOD-derived liquid film, as illustrated in Figure 2.7 (Biswas and Su, 2017). In the first phase transformation process, the MOD-derived liquid film is converted into an amorphous film with increasing temperature via drying, pyrolysis or thermolysis of long-chain carboxylates, gelation, and partial densification. The last phase transformation process involves the crystallization of the amorphous film through nucleation and growth.

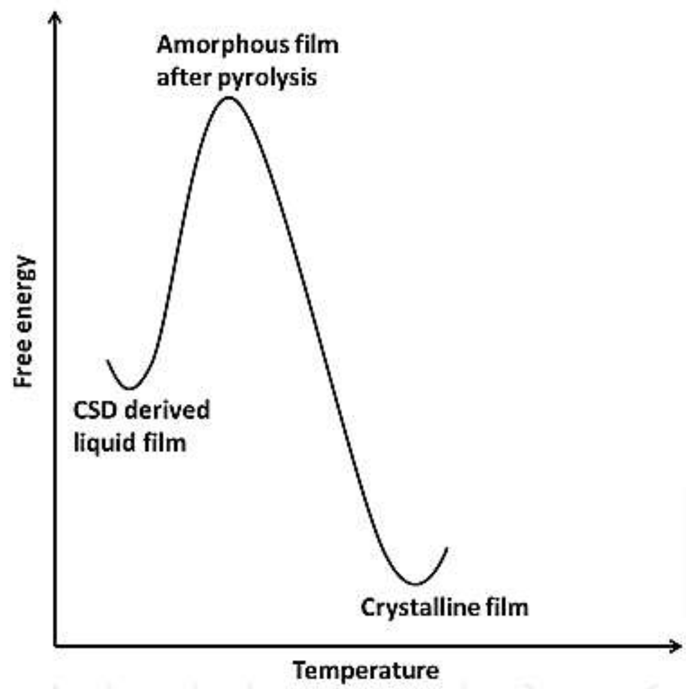

Figure 2.7. Variation of thermodynamic driving force for phase transformation with temperature (Biswas and Su, 2017)

2.8.1. Formation of amorphous thin film

Drying already starts by evaporation of the organic solvent during spin-coating of the MOD-derived liquid film and continues with the heat treatment. The thermal decomposition of Co(II) oleate has already been reported (Herrera *et al.*, 2013). The first oleate ligand starts to decompose by CO_2 elimination at about 200 ºC, leading to the formation of metastable nuclei and M-O-M network (gelation). With rising temperatures (200-300 ºC), more M-O-M linkages and partial densification may occur in the amorphous phase. M refers here to the metal while O to the oxygen.

2.8.2. Formation of crystalline thin film

The remaining oleate ligand decomposes at higher temperatures (>300 ºC), which allows the formation of more stable nuclei for the crystallization process. Nucleation is the initial stage of the crystallization process and can be homogeneous or heterogeneous in nature. Homogeneous nucleation happens in the absence of any surface such as impurity, substrate, and so forth. Heterogeneous nucleation, on the other hand, occurs at nucleation sites on surfaces and is applicable to this study. Those available sites on surfaces cause the activation energy for heterogeneous nucleation to be lower than that for homogeneous nucleation. In case of heterogeneous nucleation, the energy barrier ($\Delta G_{hetero}{}^{*}$) to be overcome for the formation of stable nucleus is given by (Biswas and Su, 2017) (Schwartz *et al.*, 1997):

$$\Delta G_{hetero}{}^{*} = \frac{16\pi\sigma^3}{3(\Delta G_v)^2} f(\theta) \qquad (2.5)$$

Where ΔG_v and σ are Gibb's free energies for a unit volume and surface, respectively. $f(\theta)$ is a factor that hinges on the contact angle (θ) between the substrate surface and the crystal. $f(\theta)$ is given by:

$$f(\theta) = \frac{2 - 3\cos\theta + \cos^3\theta}{4} \qquad (2.6)$$

2.8.2.1. Effect of crystallization temperature on heterogeneous nucleation events

Crystallization occurs through nucleation at the substrate interface ($\Delta G_{1\,int}{}^{*}$ in Figure 2.8) and film surface ($\Delta G_{1\,surf}{}^{*}$ in Figure 2.8) (Schwartz *et al.*, 1997). At identical heating rates (T vs t in Figure 2.8), both nucleation events (i.e., at the substrate interface and surface of the film) are more likely to occur for films with lower crystallization temperatures, and the resultant microstructure of the film may exhibit small, interface-nucleated grains and large semispherical grains nucleated at the surface.

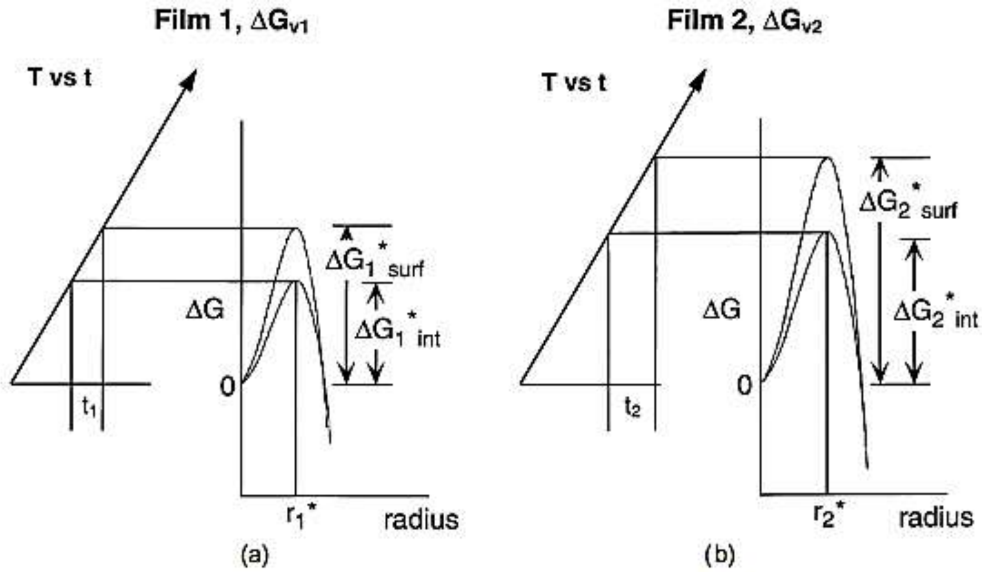

Figure 2.8. Thermodynamic driving force for phase transformation: (a) film with lower crystallization temperature and (b) film with higher crystallization temperature at identical heating rates (Schwartz *et al.*, 1997)

For higher crystallization temperatures (as is the case with long-chain metal carboxylate precursors), nucleation at the interface occurs first, followed by columnar growth, and then surface nucleation if the thermal input overcomes the energy barrier for this nucleation event. As a result, the film microstructure may be composed of interface-nucleated columnar grains with very low density of tiny surface-nucleated grains. A higher density of these grains can be obtained with increasing number of deposited layers (Schwartz *et al.*, 1997).

2.8.2.2. Temperature dependence of nucleation and growth rates

The variation of nucleation and growth rates with temperature is shown in Figure 2.9. As the temperature increases, the nucleation rate rises to a maximum value as high energy is provided to surmount the nucleation barrier. With further increase in temperature, the nucleation rate declines since the driving force for crystallization decreases when the material approaches its melting temperature (Biswas and Su, 2017). This results in a bell-shaped plot of nucleation rate versus temperature. A similar trend can be observed for the variation of growth rate with temperature.

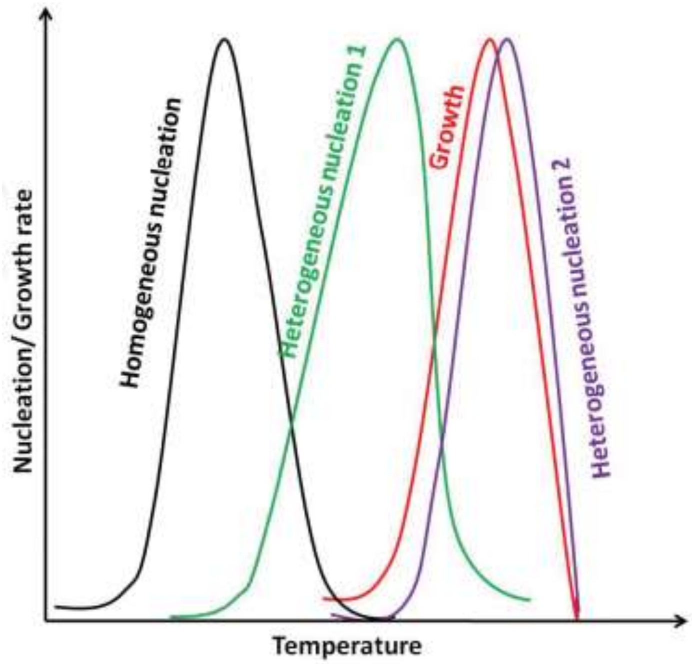

Figure 2.9. Nucleation/growth rate vs temperature (Biswas and Su, 2017)

2.9. Organic surface modifiers: amino acids

Amino acids are attractive surface modifiers as they are green and environmentally benign. Amino acids are building blocks of proteins. The basic structure of an amino acid includes an amino group (─NH_2), a hydrogen atom (─H), a carboxyl group (─COOH), and a side chain (─R) that are all attached to one carbon atom, known as α-C-atom. Amino acids can be identified by their side chains which often bear a functional group specific to different amino acids. The solution pH and isoelectric point (IEP) of amino acids are two determining factors of their net electric charge. In solution, an amino acid may be in cationic (pH < IEP), zwitterionic (pH = IEP), or anionic (pH > IEP) form, as illustrated in Figure 2.10. The charge and pKa-value of each functional group of amino acids strongly depends on its type (Kumar and Rai, 2010).

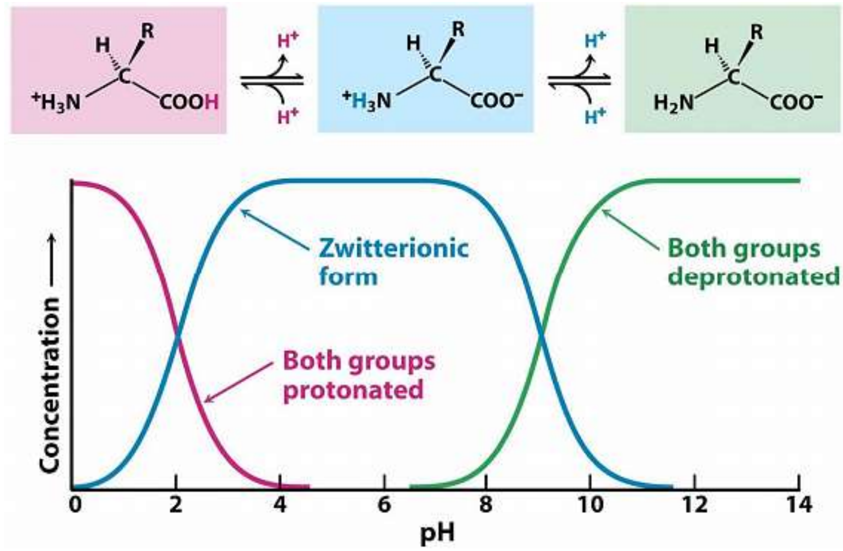

Figure 2.10. Occurrence of cationic, zwitterionic, and anionic form of amino acids at various pH-values (Kumar and Rai, 2010)

One example of amino acids is L-Arginine. This semi-essential amino acid (i.e., it is made by the body and comes from food also) has a linear side chain with guanidine as a functional group located in δ-positon to the α-C-atom (see Figure 2.11).

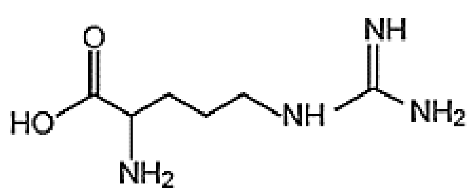

Figure 2.11. Structure of L-Arginine

The highly basic guanidine group ensures that L-Arginine remains protonated at neutral pH-values, which will greatly benefit its application as nitrite receptor in neutral medium. L-Arginine is a precursor for nitric oxide (a signaling molecule for blood pressure regulation) and creatine (muscle's energy booster).

2.9.1. Amino acid-surface interactions

Surface modification by amino acids can be achieved through physical and chemical methods. Physical methods are non-specific and involve electrostatic interactions, hydrogen bonding, and weak Van der Waals forces. Chemical methods, on the other hand, are specific and describe the formation of a covalent or non-covalent chemical bond during amino acid-surface interaction. Physical methods have poor thermal and solvolytic stability compared to chemical methods due to weak forces. The modification process by amino acids may confer new surface properties, such as stability (Morishita *et al.*, 2009). The amino acid can either be added during synthesis of the material to prevent particle agglomeration and control particle size and shape or introduced post synthetically, which offers more versatility (An *et al.*, 2009).

2.9.2. Post-deposition amino acid-assisted hydrothermal treatment

During 1980s to 1990s, the hydrothermal method emerged as an efficient route to synthesize fine powdered metal oxides from metal-based precursors in the presence of high temperature and high pressure aqueous solutions (Jiang *et al.*, 2002). Hard templating and template-free hydrothermal synthesis have been used to synthesize different cobalt oxide-based nanoarchitectures (Jiang *et al.*, 2002), (Rumplecker *et al.*, 2007), (L. Sun *et al.*, 2009), (Mansournia and Rakhshan, 2016), (Eskalen, Kerli and Özgan, 2017). However, controlling the size and morphology of nanomaterials has always been a major challenge (Wu *et al.*, 2009). Tuning the size and shape of nanoparticles is of paramount importance to tailor their physical, optical, and electronic properties. The amino acid-assisted hydrothermal synthesis allows control over the microstructure of nanoscale materials (Wu *et al.*, 2009). A variant of this method consists of preparing a seed layer then hydrothermally treating it in the presence of an amino acid and metal salt precursor. This amino acid-assisted hydrothermal technique has been applied to synthesize superstructures in highly basic conditions (Bora *et al.*, 2011). While many researchers have widely explored the aforementioned hydrothermal routes, no attempt has been made to simultaneously functionalize and element-dope a pristine Co_3O_4 thin film in one-pot hydrothermal treatment with amino acid. The novelty in this approach is evidenced by the rare application of post-deposition element doping and functionalization of metal oxides under hydrothermal conditions.

2.9.3. Summary of identified research gaps

- Up to date, post-deposition element doping and functionalization of Co_3O_4 thin film in one-pot hydrothermal treatment with amino acid have not been studied, nor has been the potential practical application of the amino acid-treated Co_3O_4 film for electrochemical nitrite detection.
- Lack of in-depth spectral evidence on how hydrothermal treatment can reduce oxygen vacancy and how nitrogen atoms can compete for substitution into Co_3O_4 crystal lattice.
- No attempt has been made to provide a comprehensive explanation of the mechanism of nitrite electro-oxidation at Co_3O_4-modified electrodes in neutral pH environments.
- Current Co_3O_4-based sensors for amperometric nitrite detection at neutral pH have LODs restricted in the micromolar range between 0.016-0.22 µM, needing to be improved.

2.9.4. Objectives and hypothesis

It is hypothesized that post-deposition functionalization and nitrogen doping of Co_3O_4 thin film in the presence of L-Arginine under optimal hydrothermal conditions can improve the electrochemical properties of the film towards nitrite detection. The specific objectives which drive this project are those listed in Chapter 1 under section 1.2.

CHAPTER 3: SAMPLE PREPARATION AND EXPERIMENTAL TECHNIQUE

3.1. Materials

All reagents were purchased from Sigma-Aldrich South Africa and used without further purification. All chemicals were reagent grade. A phosphate buffer (PBS) with a concentration of 0.1 M and a pH of 7.4 was used as electrolyte and wash buffer. Deionized (DI) water was used throughout the experiment.

3.2. Synthesis of Co_3O_4 precursor

In a typical synthesis, cobalt oleate was prepared by ion exchange reaction between cobalt (II) chloride hexahydrate and sodium oleate as illustrated in Equation 3.1 and previously reported (Wang *et al.*, 2016). For this reaction, 2.38 g of cobalt (II) chloride hexahydrate and 6.09 g of sodium oleate were dissolved into a solvent mixture of 40 mL of ethanol, 70 mL of hexane, and 30 mL of distilled water in a 200 mL beaker. This solution was then poured into a three-neck round-bottom flask, sealed, and refluxed at 70 ºC for 4 h. Thereafter, the reaction mixture was transferred with utmost care into a separatory funnel. The supernatant organic layer of cobalt oleate was washed three times with 15 mL of distilled water. While washing, the mixture was cautiously shaken to evaporate hexane off. The oleate precursor was then drained out of the funnel into a petri dish after the underlying inorganic liquid was discarded. The petri dish was placed in an oven at 60 ºC until dry waxy cobalt oleate was obtained.

$$CoCl_2.6H_2O + 2Na(C_{18}H_{33}O_2) \underset{\Delta}{\rightarrow} \mathbf{Co(C_{18}H_{33}O_2)_2} + 2NaCl + 6H_2O \qquad (3.1)$$

3.3. Co_3O_4 Electrode fabrication

Co_3O_4 thin film was prepared by using methods reported in literature (Dupin, J. C. *et al*., 2000), (Eby, D. M. *et al.*, 2012). An amount of 0.126 g of cobalt oleate was dispersed into 0.7 mL of toluene. The mixture was sonicated for 45 min in a 45 kHz ultrasonic bath for homogeneity. Three pieces of FTO-coated glass were cut to size followed by ultrasonic cleaning for 15 min in ethanol and DI water, respectively. The cleaned FTO substrates were oven dried at 60 ºC and then allowed to cool to room temperature. Subsequently, the three air-cooled FTO slides (geometric area = 1 cm^2) were spin-coated each at 4000 rpm for 1 min with 50 µL of the homogeneous cobalt oleate solution prior to calcination at 350 ºC for 10 min. The spin coating and calcination of the slides were repeated alternately until four layers of deposition were reached. A univariate study was conducted to determine the number of deposited layers for optimum response current of nitrite oxidation (Figure A.1a in APPENDIX A). XRD data (Figure B.1 in APPENDIX B) and cross-sectional SEM image (Figure B.2 in APPENDIX B) confirm the presence of Co_3O_4 crystal structure without any other phase presents and deposition of Co_3O_4 thin film, respectively, as reported by our earlier work (Gangarajula and Gopal, 2012), (Gota, Chowdhury and Ojumu, 2017).

3.4. Hydrothermal treatment of Co_3O_4

One of the three Co_3O_4 modified FTO slides, labelled Co_3O_4/FTO, was stored in pristine condition, and the other two were hydrothermally treated each with a different reacting medium at 90 ºC for 24 h in a Teflon-lined stainless-steel autoclave. Hydrothermal treatment time and temperature were determined from the optimization study in Figure A.1c & d (APPENDIX A). HT-Co_3O_4/FTO and L-Arginine/Co_3O_4/FTO were formed after treatment with 60 mL water and 60 mL of 0.15 M L-Arginine solution (unadjusted pH of the solution = 11), respectively. Various concentrations and pH conditions of L-Arginine were used; however, 0.15 M L-Arginine at pH 11 resulted in the best performing electrode in terms of anodic peak current (Figure A.1e in APPENDIX A). The hydrothermally treated electrodes were washed repeatedly with PBS and dried at room temperature overnight. The resulting slides, specifically, Co_3O_4/FTO, HT-Co_3O_4/FTO, and L-Arginine/Co_3O_4/FTO were physically and electrochemically characterized thereafter. The complete fabrication process is summarized in Scheme 3.1.

3.5. Treatment of Co_3O_4 under dipping and reflux conditions

Dipping and reflux experiments were performed using Co_3O_4/FTO in the presence of L-Arginine. Typically, a fresh Co_3O_4/FTO was dipped into a beaker containing 60 ml of 0.15 M L-Arginine solution (unadjusted pH = 11) at room temperature for 24 h. The influence of dipping time and pH on anodic peak current was studied and discussed (APPENDIX A). Another Co_3O_4/FTO was refluxed under similar conditions (i.e., time, temperature, L-Arginine concentration, and pH) to those for the optimized hydrothermal treatment. The dipped and refluxed Co_3O_4/FTOs were compared with L-Arginine/Co_3O_4/FTO based on their oxidation peak currents (Figure A.1b in APPENDIX A). In this way, we were able to investigate the effect of different treatment processes on anodic peak current and bring out the advantage of hydrothermal treatment over the dipping and reflux processes.

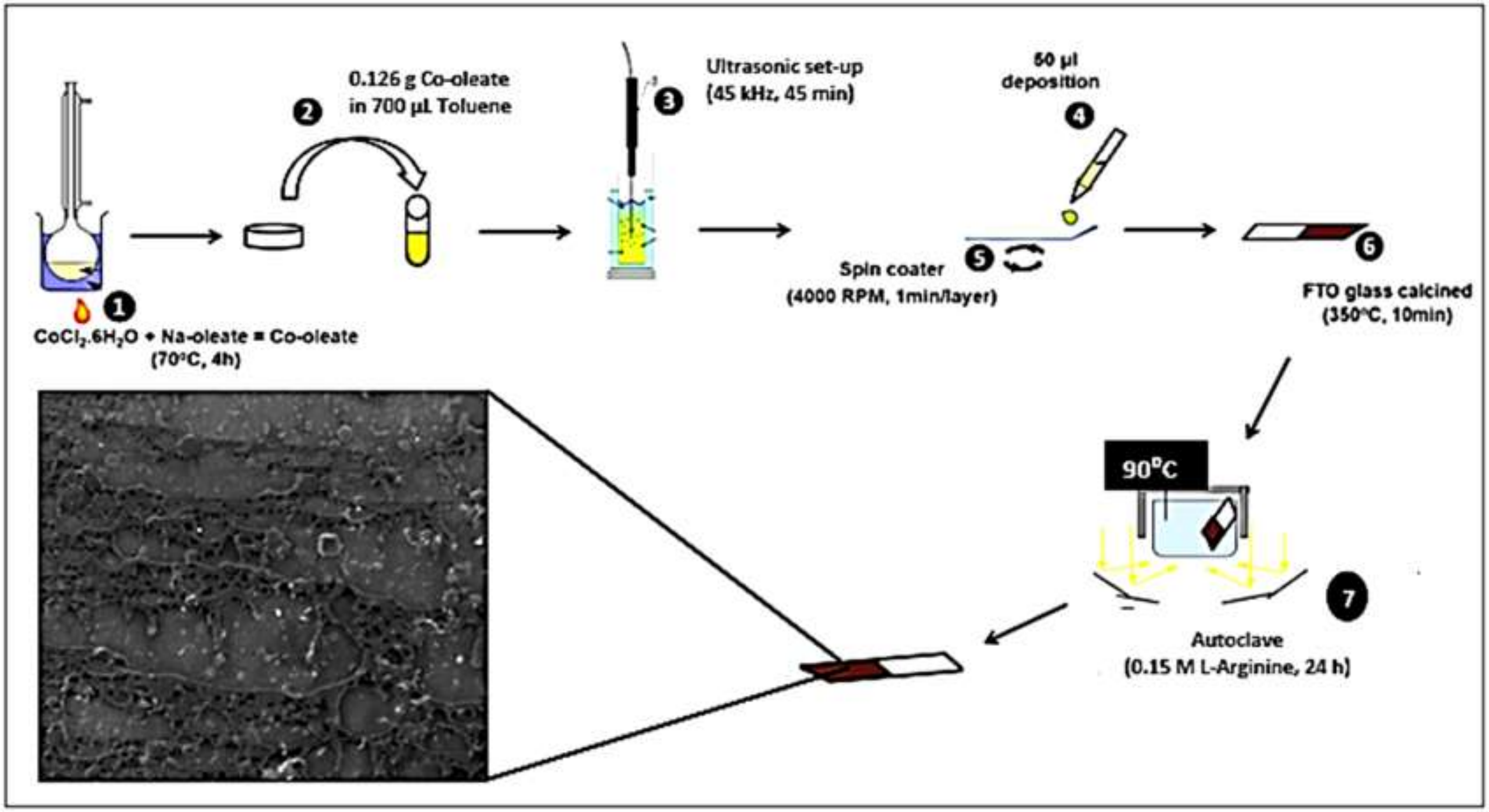

Scheme 3.1: Schematic illustration for the fabrication of L-Arginine modified Co_3O_4 thin film for nitrite detection

3.6. Physical characterization

3.6.1. Scanning electron microscopy (SEM)

SEM is a physical characterization technique which provides graphical information about the surface morphology of a specimen. During SEM analysis, the specimen is bombarded with a beam of electrons, and part of the incident beam energy is lost as heat, light, or other alternative forms of energy. The resultant emission illuminates the specimen and allows viewing of its microstructure. SEM micrographs of the surface texture of Co_3O_4/FTO, HT-Co_3O_4/FTO, and L-Arginine/Co_3O_4/FTO were obtained by using Tescan MIRA3 RISE SEM, a high-resolution Field Emission SEM combining low kV imaging Nova NanoSEM.

3.6.2. Raman spectroscopy

Raman spectroscopy is an analytical technique based on different light-scattering behaviors of the chemical bonds within a material. During Raman analysis, a monochromatic light focused on a specimen is dispersed in all directions, a small fraction of the dispersed light occurs at different wavelengths (colors) due to molecular vibrations within the specimen. If the emitted light has a longer wavelength (lower frequency) than the incident radiation, it is called Stokes scattering. If on the other hand the dispersed radiation is of higher frequency, it is then named anti-Stokes scattering. Two types of molecular vibrations of a molecule can take place, precisely stretching and deformation (bending) vibrations. Stretching vibrations are symmetric and asymmetric while deformation vibrations are scissoring (bending), twisting, wagging, and rocking vibrations, as illustrated in Figure 3.1 (Kumar and Rai, 2010). Raman spectra for Co_3O_4/FTO, HT-Co_3O_4/FTO, and L-Arginine/Co_3O_4/FTO were obtained using the Witec Confocal Raman Microscope (alpha300).

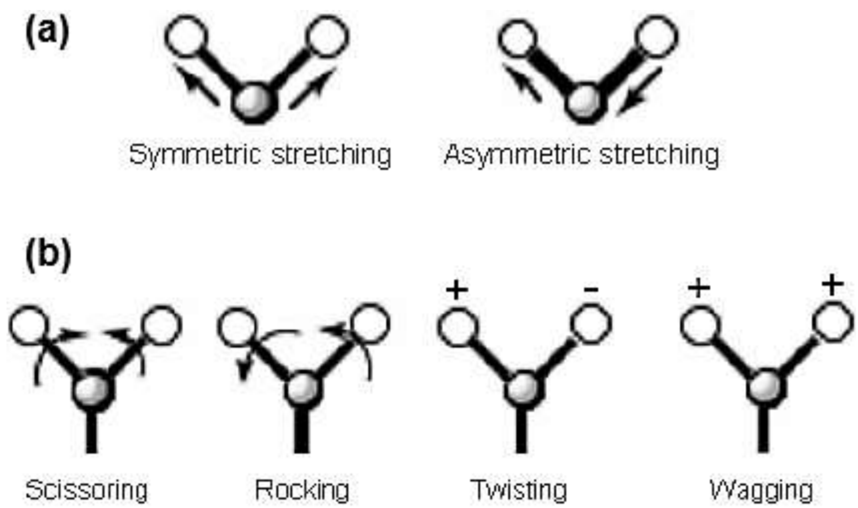

Figure 3.1. (a) Stretching vibrations and (b) deformation vibrations (Kumar and Rai, 2010)

3.6.3. X-ray photoelectron spectroscopy (XPS)

XPS is a technique for analyzing the composition, chemical and electronic states of the elements on the surface of a material. The XPS analysis provides information about the surface chemistry of the top 1-10 nm of the material being analyzed. When a high-energy beam of X-rays is focused on a specimen, it ejects electrons from the atomic core levels of all surface elements, excluding hydrogen as it has no core electrons. The ejected electrons are counted over a range of their measured kinetic energies for identification and quantification of the surface elements. X-ray photoelectrons from different chemical elements, energy levels, or oxidation states of an element possess different kinetic energies. The XPS measurements were carried out on Co_3O_4/FTO, HT-Co_3O_4/FTO, and L-Arginine/Co_3O_4/FTO with spatial resolution of < 3 µm using KRATOS AXIS X-ray photoelectron spectrometer at UNISA (Florida Science Campus), South Africa.

3.7. Electrochemical evaluation

All electrochemical measurements were carried out using Autolab PGSTAT302N potentiostat. The conventional three-electrode setup was adopted in which Ag/AgCl (3 M KCl) acted as the reference electrode, Pt wire as counter electrode, and the as prepared electrodes as working electrode.

3.7.1. Cyclic voltammetry (CV)

CV is a potential dynamic method whereby the current is recorded by cycling the potential of a working electrode within an assigned range. CV analysis is useful to study the electrochemical properties of redox reactions that may occur at the working electrode during the potential sweep. CV experiments were performed in 0.1 M PBS solution (pH = 7.4) in the presence of 2 mM NO_2^- at a scan rate of 10 mV/s. Scan rate and concentration studies were also conducted using the CV method.

3.7.2. Electrochemical impedance spectroscopy (EIS)

EIS measures the impedance of an electrolytic cell at various frequencies of an applied alternating current voltage. The recorded impedance spectrum may indicate the occurrence of resistance, capacitance, diffusion, and inductance in the electrolytic cell. The electrochemical impedance study was conducted at room temperature, at the ac voltage amplitude of 10 mV, and within the frequency range of 0.01–10^5 Hz in 0.1 M KCl + 5 mM $K_3[Fe(CN)_6]$ solution. The Randles equivalent circuits were obtained using EIS Spectrum Analyser in Newton algorithm mode.

3.7.3. Chronoamperometry (CA)

CA is a potentiostatic current-time technique that can be used to unlock information about the sensor performance characteristics. CA experiments were carried in 0.1 M PBS solution (pH = 7.4) in the presence of varying NO_2^- concentrations at a constant applied potential of 0.96 V. Long-term stability and interference studies were also conducted using the CA technique.

CHAPTER 4: RESULTS AND DISCUSSION

4.1. Physical characterization

The as prepared electrodes, i.e., Co_3O_4/FTO, HT-Co_3O_4/FTO, and L-Arginine/Co_3O_4/FTO were characterized using SEM, Raman spectroscopy, and XPS. It can be seen from SEM images that there is no change in the rough and compact surface of pristine Co_3O_4/FTO (Figure 4.1a) after hydrothermal treatment (HT-Co_3O_4/FTO thin film in Figure 4.1b). However, the hydrothermal treatment of pristine Co_3O_4/FTO thin film in the presence of L-Arginine (Figures 4.1c & d) caused a drastic modification of its surface texture. The difference in surface structure between HT-Co_3O_4/FTO and L-Arginine/Co_3O_4/FTO arises through chelation of cobalt oxide surface by the amino acid in basic environment (pH = 11), causing the dissolution of some cobalt from the electrode surface into adsorbate solution. This is consistent with the depleted cobalt content in L-Arginine/Co_3O_4/FTO, as per XPS analysis in Table C.1 (APPENDIX C). The porous nature of the surface of L-Arginine/Co_3O_4/FTO can potentially allow easy access to active sites and improve mass transport kinetics.

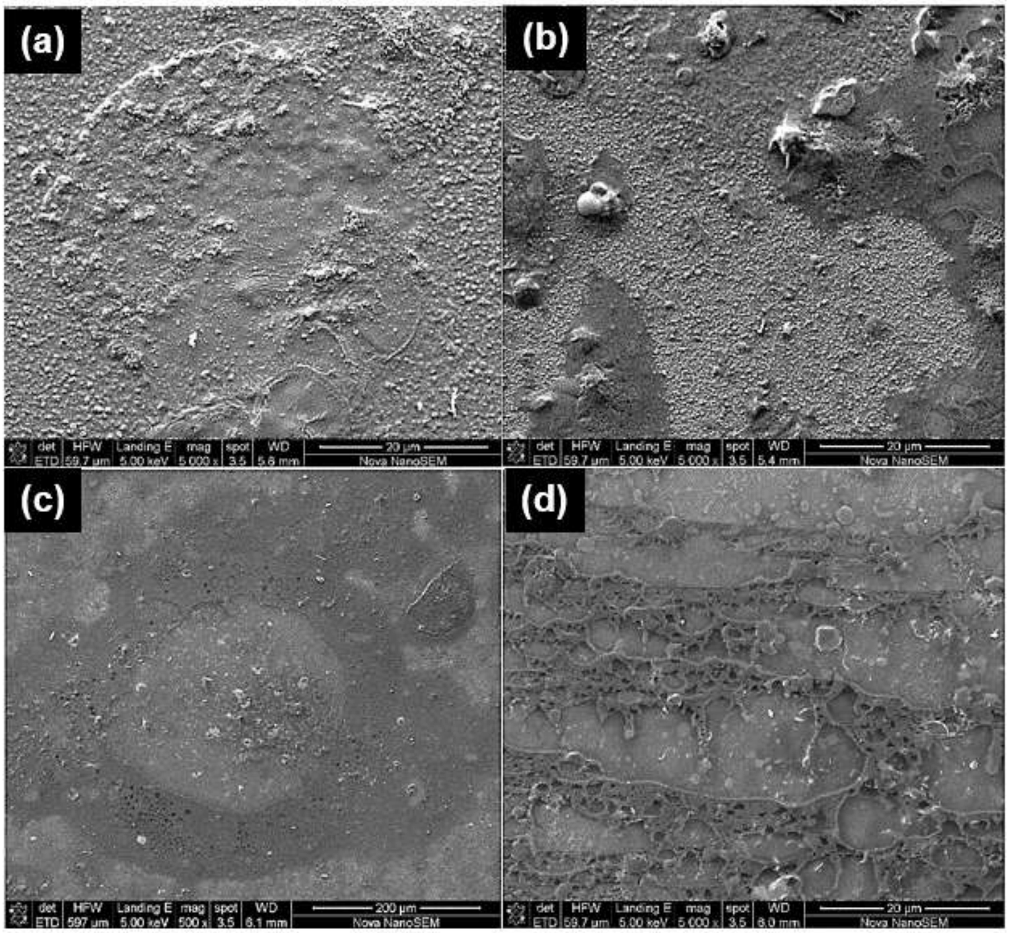

Figure 4.1: SEM images of (a) Co_3O_4/FTO, (b) HT-Co_3O_4/FTO, (c) L-Arginine/Co_3O_4/FTO thin films, and (d) Magnified view of (c)

Figure 4.2a shows five Raman-active modes of Co_3O_4/FTO thin film at 192(F_{2g}), 470(E_g), 514(F_{2g}), 605 (F_{2g}), and 674(A_{1g}) cm^{-1}, which compare well with those of pure Co_3O_4 (Diallo *et al.*, 2015). Hence, the Raman-active modes as detected confirm the presence of spinel Co_3O_4 structure. The Raman-active bands for HT-Co_3O_4/FTO and L-Arginine/Co_3O_4/FTO thin films are narrower and appear at higher wavenumbers than those for Co_3O_4/FTO, highlighting a decrease in oxygen vacancies (De Rivas *et al.*, 2011). However, the A_{1g} line for L-Arginine/Co_3O_4/FTO is significantly blue shifted. Previous studies reported the unusual upshift of A_{1g} mode as a sensitive indication of heteroatomic doping (Ouyang, Wang and Wang, 2015). In this case, the formation of a Co-N bond is plausible after hydrothermal treatment of Co_3O_4/FTO in L-Arginine environment since the amino acid is a potential nitrogen source. The additional upshifts of F_{2g} + E_g + F_{2g} + F_{2g} modes for L-Arginine/Co_3O_4/FTO compared with those for HT-Co_3O_4/FTO may be the result of nitrogen incorporation into Co_3O_4 lattice. Because N (ionic radius of N^{3-} = 1.46 Å) is bigger than O (ionic radius of O^{2-} = 1.36 Å), substitutional N doping can cause compressive forces to the lattice near N^{3-} (i.e., Co-O), thereby reducing the mean bond length of Co-O bond and increasing its vibration frequency. Thus, the more significant shift of A_{1g} mode for L-Arginine/Co_3O_4/FTO suggests that N substituted O in octahedral coordination, since the site in the vicinity of N^{3-} experiences stronger squeezing forces than that further away. No other phases were detected in the Raman spectra for Co_3O_4/FTO, HT-Co_3O_4/FTO, and L-Arginine/Co_3O_4/FTO, as shown in Figure 4.2a. The enhancement in Raman emission for HT-Co_3O_4/FTO could be the result of hole doping after exposure of Co_3O_4/FTO to hole-donors, such as hydroxyl groups (-OH) in the hydrothermal medium (Hao *et al.*, 2013). The increased hole content in HT-Co_3O_4/FTO can promote high field emission properties. The hole doping effect is, however, less acute in the Raman spectrum for L-Arginine/Co_3O_4/FTO certainly because of the amino groups introduced by the amino acid, which can act as electron-donors.

In Figure 4.2b, the Raman peaks for Co_3O_4/FTO, HT-Co_3O_4/FTO, and L-Arginine/Co_3O_4/FTO at 1090, 1119/1126, 1220, 1345/1582 cm^{-1} are ascribed to C-O(H), asymmetric aliphatic C=O, C-O-C, and C-C bond, respectively [83], accounting for adventitious carbon during the preparation procedure and carbon from the oleate precursor. The broad bands (one small and the other strong) at 1753 cm^{-1} and 2845 cm^{-1} are attributed, respectively, to the Raman stretching of carboxylic C=O and alcoholic or carboxylic -OH involved in hydrogen bonding interactions (Long, 2004), (Larkin, 2011). The weak broad band at 3586 cm^{-1} can be assigned to the hydrogen bonded hydroxyl group of water molecule (Kolesov, 2006). The peak around 1190 cm^{-1} is attributed to stretching vibration of CO group of the amino acid molecule (Kumar and Rai, 2010). It is worth mentioning that this peak (1190 cm^{-1}) is less intense and occurs at lower frequencies (by 2-3 cm^{-1}) than that in the cited literature. This could mean coordination of L-Arginine to Co_3O_4 surface. The Raman signals at 1167 cm^{-1} and 1264 cm^{-1} are also signatures, respectively, of NH_3^+ rocking (Freire *et al.*, 2017) and Cδ-twist (Zhu *et al.*, 2011) in the amino acid.

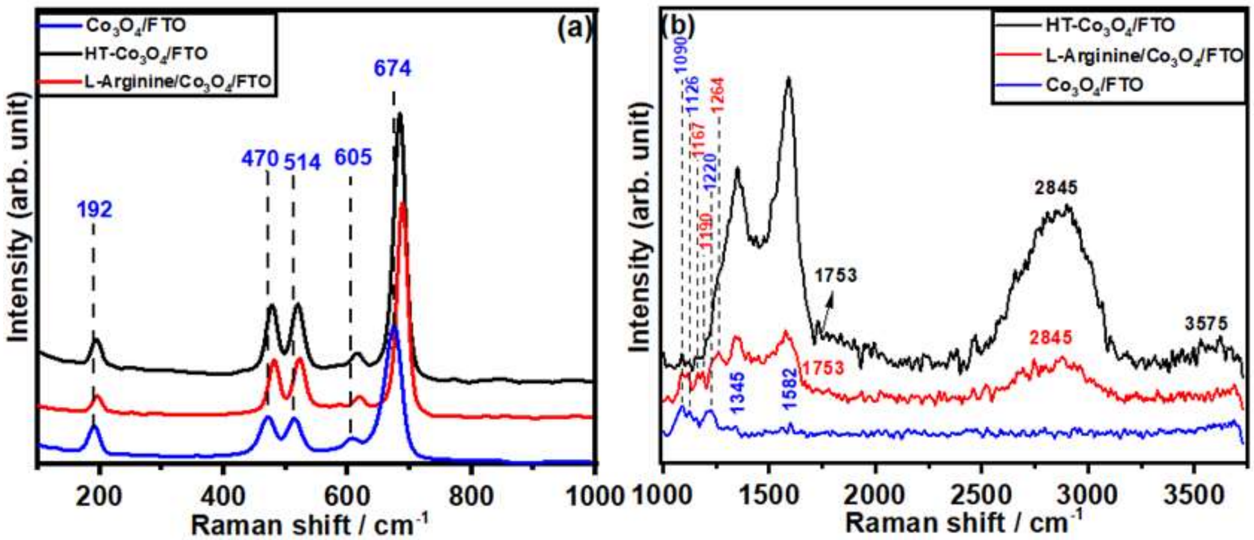

Figure 4.2: Raman spectra for Co_3O_4/FTO, HT- Co_3O_4/FTO, and L-Arginine/Co_3O_4/FTO thin films within wavenumber ranges of (a) 100 – 1000 cm^{-1} and (b) 1000 – 3750 cm^{-1}

All the XPS spectra (C 1*s*, O 1*s*, Co 2*p,* and N 1*s*) were referenced at 284.8 eV for adventitious carbon and deconvoluted using OriginPro software. Figure 4.3a displays various levels of contamination of Co_3O_4/FTO, HT-Co_3O_4/FTO, and L-Arginine/Co_3O_4/FTO to carbon. The C 1*s* spectrum for Co_3O_4/FTO in Figure 4.3b was deconvoluted into four Gaussian peaks (linear baseline) centered each at 284.8 eV for C-C, 286.1 eV for C-O, 288.6 eV for C=O, and 292.5 eV for mixed O-C=O, CO_3^{2-}, and ester groups (Smirnova *et al.*, 2019). A notable decrease in peak intensities of C-O and C=O can be detected in the C 1*s* spectra for HT-Co_3O_4/FTO and L-Arginine/Co_3O_4/FTO compared with C 1*s* deconvolution for Co_3O_4/FTO. This could be associated with the generation of higher oxidation states of carbon observed in Figures 4.3c & d at 292.5 eV (for mixed O-C=O, CO_3^{2-}, and ester groups) and 295.3 eV (for physisorbed CO_2 (Betancur *et al.*, 2018)). The negative shift of C=O (by 0.5 eV) in Figures 4.3c & d, relative to its binding energy position in Figure 4.3b, probably results from a decrease in the double-bond character of the carbonyl group which is also in accordance with Raman. The C 1*s* spectral lines for HT-Co_3O_4/FTO and L-Arginine/Co_3O_4/FTO show similar trends but differ with the appearance of a small peak at 292.9 eV in Figure 4.3c, ascribed to the carbon in the protonated side chain of L-Arginine (Xu *et al.*, 2017).

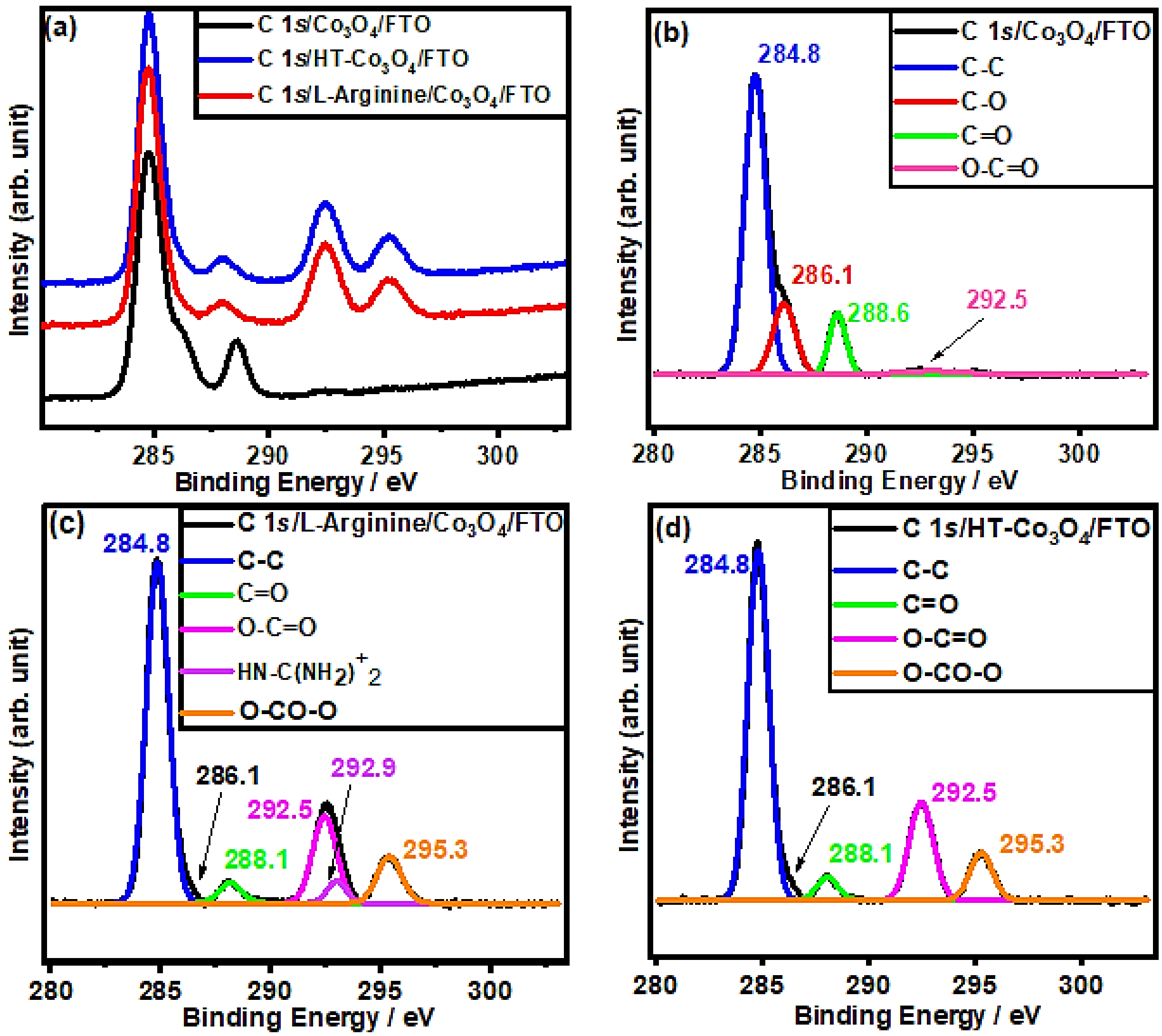

Figure 4.3: (a) C 1s XPS spectrum for Co_3O_4/FTO, HT-Co_3O_4/FTO, and L-Arginine/Co_3O_4/FTO thin films; deconvolution of C 1*s* XPS spectra for (b) Co_3O_4/FTO, (c) L-Arginine/Co_3O_4/FTO, and (d) HT-Co_3O_4/FTO

Figure 4.4a exhibits an obvious redshift (by 1 eV) in the binding energy of the O 1*s* XPS main peak for HT-Co_3O_4/FTO and L-Arginine/Co_3O_4/FTO relative to that for Co_3O_4/FTO. Also, the second prominent peak of the O 1*s* spectrum for Co_3O_4/FTO in Figure 4.4a seems to be absent in the spectrum for HT-Co_3O_4/FTO and L-Arginine/Co_3O_4/FTO. These changes are further investigated with the decomposition of individual O 1*s* XPS spectral lines. In Figure 4.4b, the Gaussian peaks (linear baseline) at 531.7, 533.1, and 530.3 eV are ascribed to lattice oxygen (O^{2-}), adsorbed oxygen (O^{-}), and loosely bound surface oxygen, respectively (Dupin *et al.*, 2000),(Deng *et al.*, 2018). The corresponding peaks emerge, respectively, at 530.7/8, 532.1, and 529.3/4 eV in Figures 4.4c & d. Adsorbed water molecules (or hydroxyl group) and physisorbed CO_2 can be assigned the XPS bands at 533.3 eV (Halim *et al.*, 2016) and 535.2/3 eV (Rao and Nozoye, 2003), respectively. The spectral weight ratio of $O_{Latt}/(O_{Latt}+O_{Ads})$ for Co_3O_4/FTO, L-Arginine/Co_3O_4/FTO, and HT-Co_3O_4/FTO was calculated to be 0.42, 0.69 and 0.72, respectively, showing chemical state changes of lattice oxygen from non-stoichiometric to stoichiometric amount. This is consistent with the binding energy peak position of the O 1*s* main band for Co_3O_4/FTO (531.7 eV), L-Arginine/Co_3O_4/FTO (530.8 eV), and HT-Co_3O_4/FTO (530.7 eV).

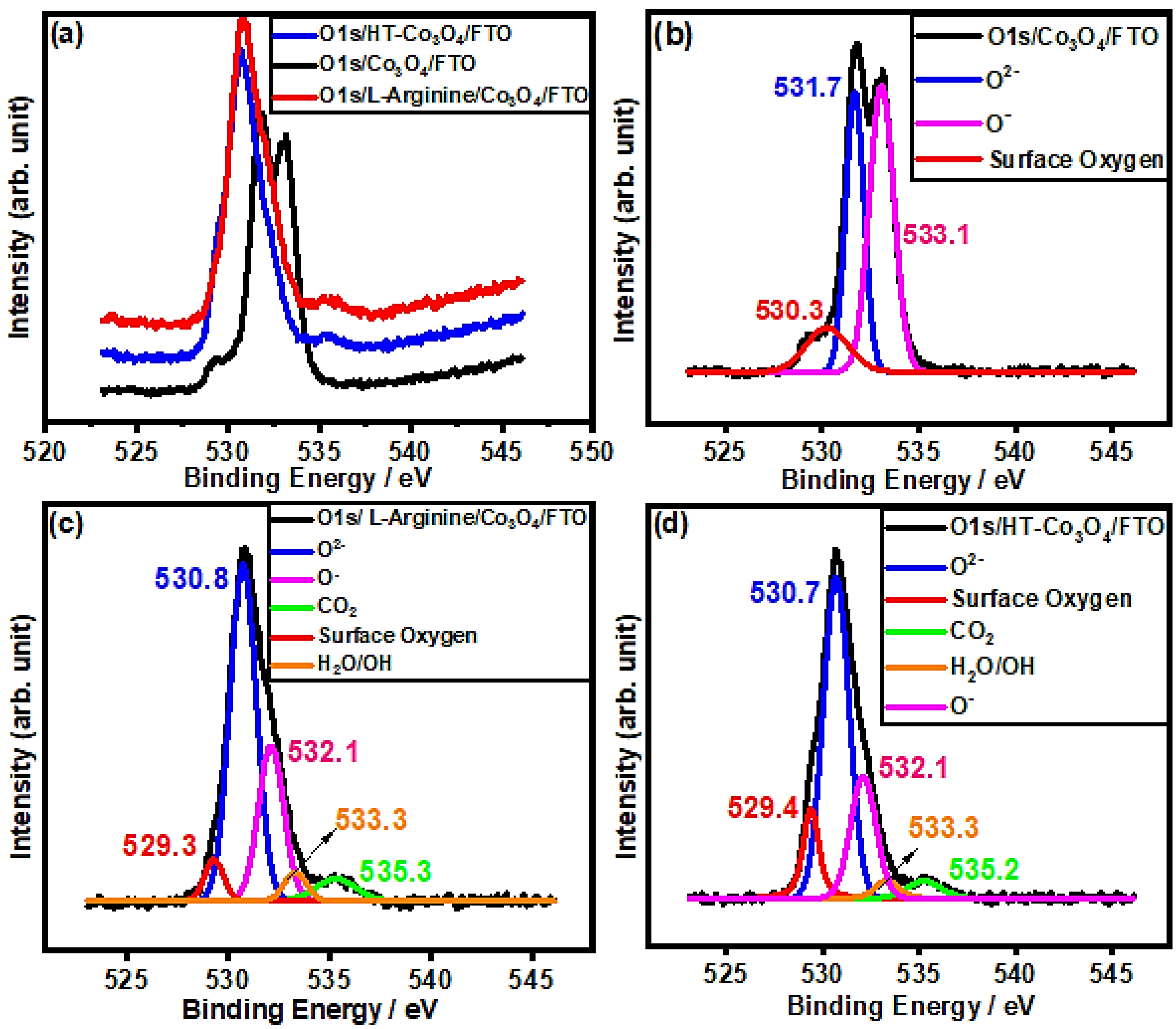

Figure 4.4: (a) O 1s XPS spectral lines for Co_3O_4/FTO, HT-Co_3O_4/FTO, and L-Arginine/Co_3O_4/FTO thin films; deconvoluted O 1*s* XPS peaks for (b) Co_3O_4/FTO, (c) L-Arginine/Co_3O_4/FTO, and (d) HT-Co_3O_4/FTO

It is important to stress out that we only considered Co 2$p_{3/2}$ (Figure 4.5a-d) for spectral deconvolution as usually reported for Co_3O_4 (Zheng *et al.*, 2017). Co 2$p_{3/2}$ XPS main peak for Co_3O_4/FTO can be seen at 779.1 eV, with a spin orbit splitting (Co 2$p_{1/2}$ –Co 2$p_{3/2}$) of 15.1 eV as confirmation of mixed Co (II and III) in Co_3O_4 (Zhu *et al.*, 2013). The XPS peak at 779.1 eV is assigned to low coordinated octahedral Co^{3+} whereas the peak at 780.1 eV is ascribed to low coordinated tetrahedral Co^{2+}. These two peaks appear at lower binding energies (by 0.4 eV) than expected (Finkler *et al.*, 2018) due to higher electron density resulting from oxygen vacancies . The peak area ratio of octahedral Co^{3+} to tetrahedral Co^{2+} (Co^{3+}/Co^{2+}) for Co_3O_4/FTO was calculated to be 2.27, which is in good agreement with recently published results (Zheng *et al.*, 2020). The XPS signals at 780.8/782.4 and 781.8 eV are attributed, respectively, to Co^{2+} (X. Sun *et al.*, 2009) and Co^{3+} (Zhan *et al.*, 2020) at the surface or subsurface. The two satellite peaks at 784 eV and 788.3 eV are associated with paramagnetic Co^{2+} (Amri *et al.*, 2013). Notable XPS spectral changes can be observed for HT-Co_3O_4/FTO in Figure 4.5d with respect to the spectrum for Co_3O_4/FTO. In particular, the blueshift (by 0.2 eV) of Co 2$p_{3/2}$ main peak (779.3 eV), consequently the lower spin-orbit spacing (14.9 eV) for HT-Co_3O_4/FTO suggests an increase in Co^{3+} content due to oxygen filling. To confirm this, we further calculated the Co^{3+}/Co^{2+} ratio (2.70) and found it to be higher than that for Co_3O_4/FTO. When oxygen fills the vacancy (forward direction of Equation 3.1), it introduces partially filled 2*p* orbitals that drive out the two electrons trapped in cationic sites (this is reflected by the upshift of Co 2*p* XPS main peak and increase in Co^{3+} concentration) then becomes completely filled (O^{2-}).

$$Co^{2+}\text{-}V_O\text{-}Co^{2+} + \tfrac{1}{2}\, O_2 \leftrightarrow Co^{3+}\text{-}O^{2-}\text{-}\ Co^{3+} \qquad (3.1)$$

The higher Co^{3+}/Co^{2+} ratio can also be linked to an increased amount of hole in HT-Co_3O_4/FTO since Co^{3+} has one electron less than Co^{2+} in its electronic configuration. The hole doping has an enhancing effect on the photoemission of Co 2*p* XPS spectrum for HT-Co_3O_4/FTO. These observations affirm the oxidation of Co^{2+} to Co^{3+} took place after oxygen filling of Co_3O_4/FTO during treatment with water. Based on Sensor and Electrochemical Characterizations (following section), the performance of Co_3O_4/FTO for nitrite detection at neutral pH seems to decrease with an increase in Co^{3+} concentration, suggesting Co^{2+} as the active site for nitrite electrooxidation in neutral PBS solution.

In contrast, decomposition of Co2$p_{3/2}$ XPS spectrum for L-Arginine/Co_3O_4/FTO reveals the presence of a metallic phase of cobalt (Co^0) at 778.8 eV as proof of Co-N bond formation (Pan *et al.*, 2019) which corroborates the Raman and O 1*s* XPS. The Co-N bond formation has been reported to promote metallic conductivities (Cho *et al.*, 2018) and may be responsible for the superior electrochemical activity of L-Arginine/Co_3O_4/FTO towards nitrite oxidation compared with Co_3O_4/FTO and HT- Co_3O_4/FTO. The ratio of [(Co^0+Co^{3+})/Co^{2+}] was found to be 2.14 which is close to that of Co^{3+}/Co^{2+} 2.27 for Co_3O_4/FTO suggesting partial substitution of oxygen in octahedral coordination by nitrogen. Co $2p_{3/2}$ XPS main band (779.5 eV) for L-Arginine/Co_3O_4/FTO, with a spin-orbit splitting of 14.6 eV, experiences a much larger blueshift than that for HT-Co_3O_4/FTO. Also, a higher A/B ratio can be observed in Figure 4.5a for L-Arginine/Co_3O_4/FTO compared with that for HT-Co_3O_4/FTO and Co_3O_4/FTO. These spectral behaviours assuredly stem from the presence of doping N atoms in L-Arginine treated Co_3O_4 lattice. Explicitly, similarly to oxygen filling, nitrogen filling of oxygen vacancies can unleash two electrons from the 3*d* states of two Co(II) cations, forming N^{2-}. However, as opposed to O^{2-}, N^{2-} has one unfilled 2*p* orbital and can cause additional electron transfer from the 3*d* orbitals of most likely Co(II) (it is easier to eject an electron from Co(II) than Co(III)) to produce N^{3-} species, as illustrated by Equation 4.1-4.2.

$$Co^{2+}\text{-}V_O\text{-}Co^{2+} + \tfrac{1}{2} N_2 \rightarrow Co^{3+}\text{-}N^{2-}\text{-}Co^{3+} \quad (4.1)$$

$$Co^{3+}\text{-}N^{2-}\text{-}Co^{3+} + \text{-}Co^{2+}\text{-} \rightarrow Co^{3+}\text{-}N^{3-}\text{-}Co^{3+} + \text{-}Co^{3+}\text{-} \quad (4.2)$$

While substitutional nitrogen doping of Co_3O_4 will cause a redshift of Co $2p_{3/2}$ XPS peak center (Yu *et al.*, 2017), nitrogen filling the oxygen vacancies will induce its blueshift (Xiao *et al.*, 2017). Therefore, the observed giant upshift of the Co $2p_{3/2}$ XPS main line for L-Arginine/Co_3O_4/FTO was proposed to be the result of the synergistic effect of nitrogen and oxygen filling.

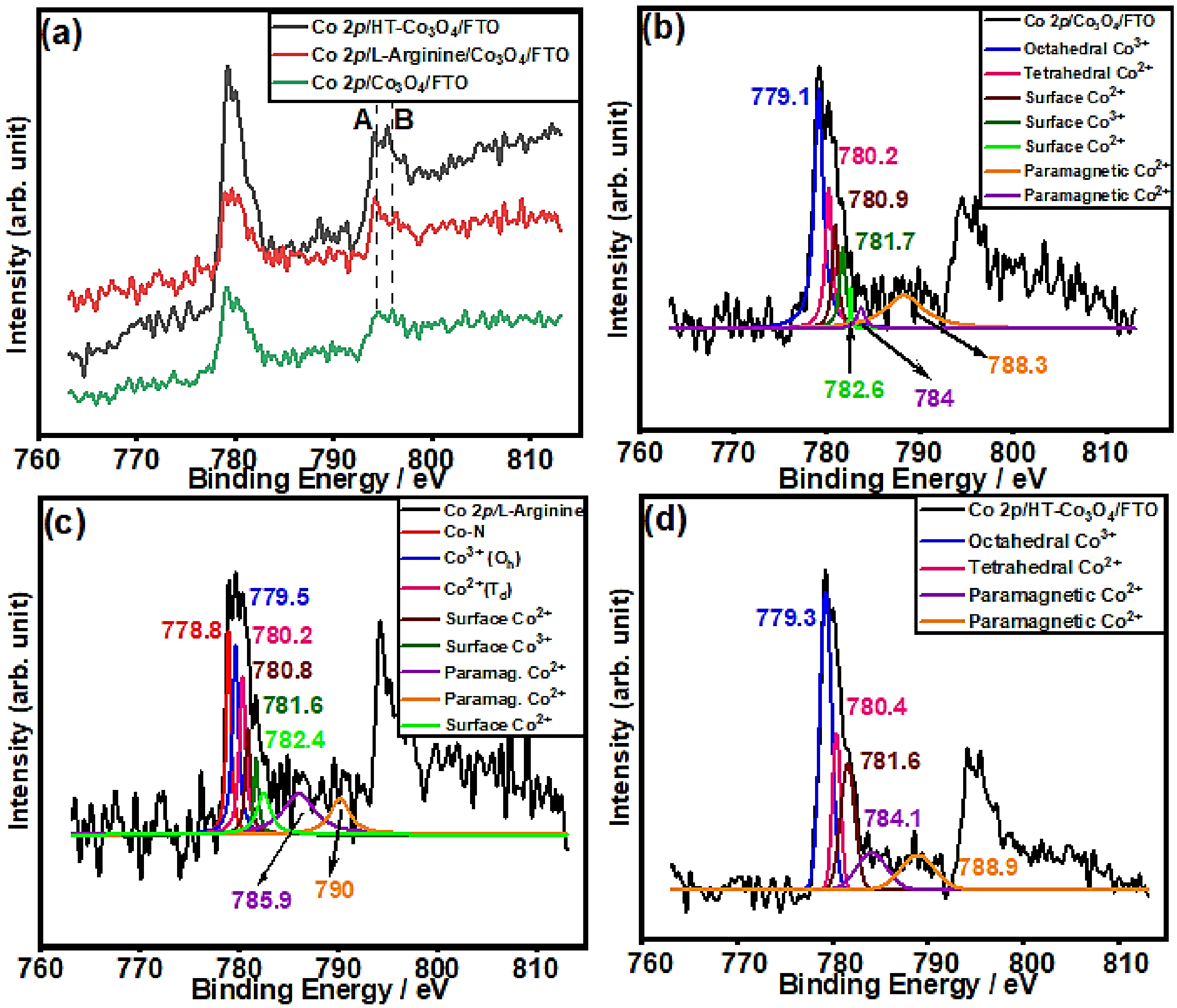

Figure 4.5: (a) Co 2*p* XPS spectral peaks for Co_3O_4/FTO, HT- Co_3O_4/FTO, and L-Arginine/ Co_3O_4/FTO thin films. Lorentzian and Gaussian Co 2*p* XPS peaks for (b) Co_3O_4/FTO, (c) L-Arginine/ Co_3O_4/FTO, and (d) HT- Co_3O_4/FTO

To further understand the role of L-Arginine, the N1s XPS spectrum for L-Arginine/Co_3O_4/FTO was evaluated to confirm the presence of L-Arginine on Co_3O_4 surface (Figures 4.6a & c). The deconvoluted spectrum showed peaks at 398.6, 399.2, 399.7, 400.4, and 401.5 eV, as seen in Figure 4.6c. The peak at 398.6 eV was ascribed to Co-N bond (Dou *et al.*, 2016) while the peaks at 399.2 and 401.5 eV were assigned to coordinated (or basic) α-amine group (Lynne and Kay, 1982) and protonated (or acidic) α-amine group (Eby *et al.*, 2012), respectively. The high ratio of basic α-amine to acidic α-amine (N/N^+ = 4.1) confirmed the coordination of L-Arginine α-amine group to Co_3O_4. Coupling Co 2*p* and N 1*s* XPS results with Raman spectroscopic study for L-Arginine/Co_3O_4/FTO, coordination of the amino acid to Co_3O_4 through carboxylate and α-amine groups was established. We assigned the photoemission at 400.4 eV (which would appear at 400.6 eV if C 1*s* were referenced at 285 eV) to the guanidinium group of L-Arginine with delocalized positive charge on the three nitrogen atoms (Santos, Blundell and Licence, 2015), but the area ratio of unprotonated α-amine group to guanidinium group was calculated to be 1:2, significantly lower than the stoichiometric value of 1:3. This led to the conclusion that some molecules of L-Arginine were decomposed via their side chains, of which the decomposition product was the nitrogen dopant. The protonated guanidinium on the surface of L-Arginine/Co_3O_4/FTO can increase its affinity for negatively charged species. The binding energy peak at 399.7 eV was attributed to chemically adsorbed dinitrogen (N_2) (Shi *et al.*, 2012), which can also be observed at 399.8 eV in Figure 4.6b. The presence of highly oxygenated nitrogen species was also noticed near 409 eV in the N 1*s* XPS spectrum for L-Arginine/Co_3O_4/FTO in Figure 4.6a.

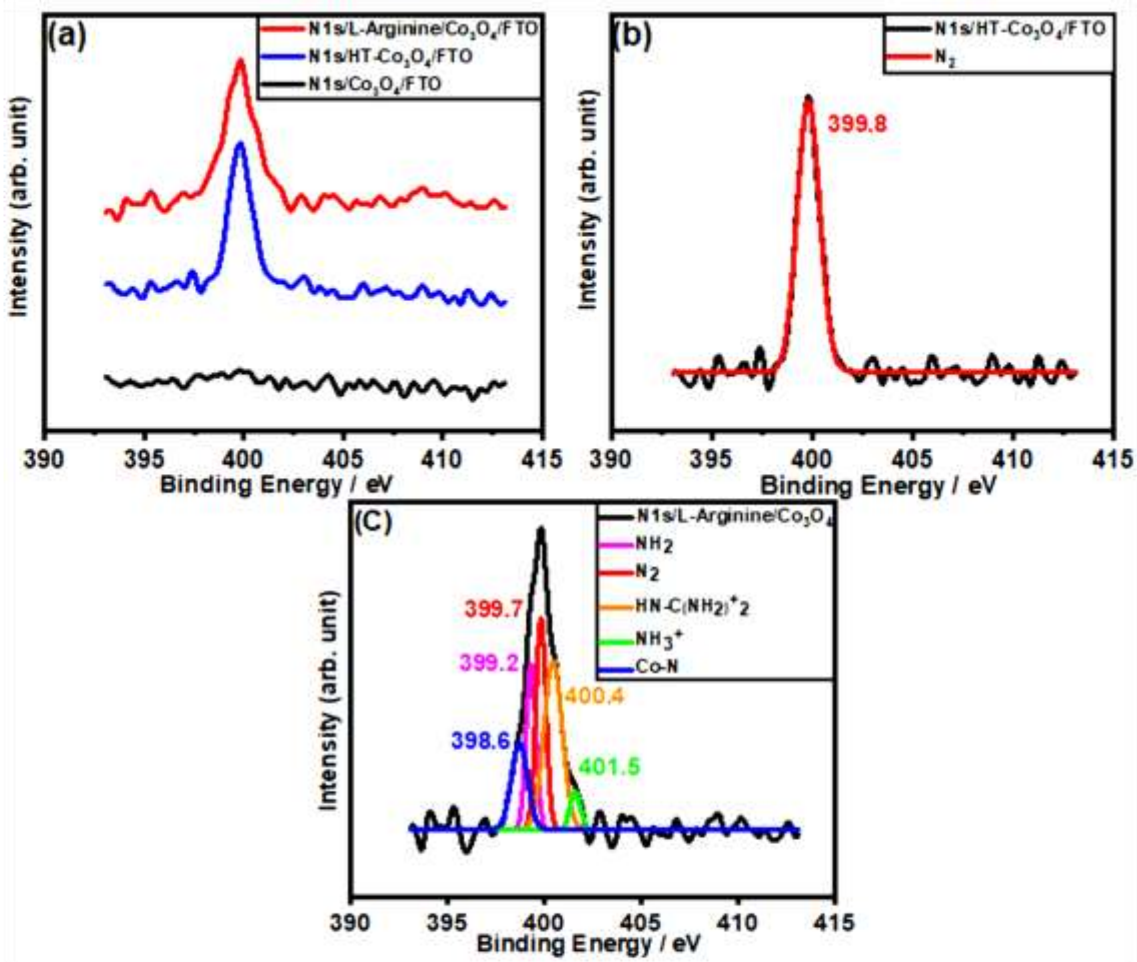

Figure 4.6: (a) N 1*s* XPS spectral emissions for Co_3O_4/FTO, HT- Co_3O_4/FTO, and L-Arginine/ Co_3O_4/FTO thin films. Gaussian N 1*s* XPS peaks; (b) HT- Co_3O_4/FTO, and (c) L-Arginine/ Co_3O_4/FTO

Hence, it can be postulated that the decomposition pathway of L-Arginine is similar to the hydrolysis of methylguanidine, reported in (Lewis and Wolfenden, 2014). Hence, the nitrogen doping mechanism was proposed in Scheme 4.1. A summary of the binding energy peak positions for the Co 2*p* XPS analysis of each electrode and their respective peak assignments is presented in Table C.2 (APPENDIX C). The spectral weight ratio results of O 1*s* and Co $2p_{3/2}$ XPS for the three electrodes are presented in Table C.3 (APPENDIX C).

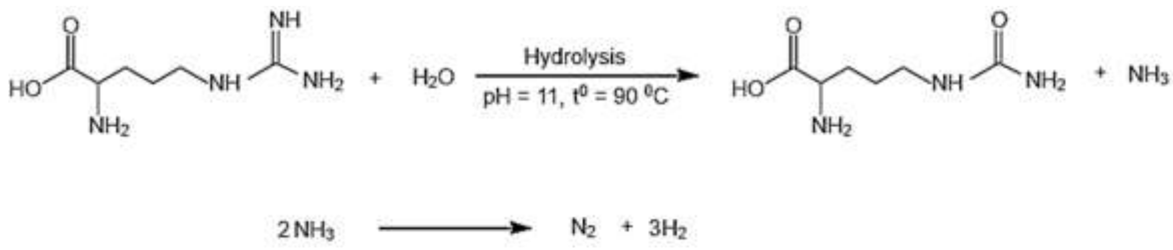

Scheme 4.1: Possible nitrogen doping mechanism

4.2. Electrochemical behaviour of the as prepared electrodes

4.2.1. Cyclic Voltammetry studies of the as prepared electrodes

Cyclic voltammograms (CV) in Figure 4.7a show the electrochemical response of the various electrodes to 2 mM NO_2^-. The L-Arginine/Co_3O_4/FTO electrode exhibited the best electrochemical activity, i.e., the highest anodic peak current response centered at 0.989 V compared to other electrodes studied. The enhanced CV response of L-Arginine/Co_3O_4/FTO towards nitrite oxidation is favoured by its metallic conductivity resulting from nitrogen doping after hydrothermal treatment of Co_3O_4/FTO with L-Arginine as was shown from XPS analysis. Also, the surface modification with cationic functional groups can possibly induce preconcentration effect on nitrite followed by a sharp increase of anodic peak current density (Zhao *et al.*, 2007). These highlights the role of L-Arginine as a nitrogen doping source and surface functionalizing agent.

A reversible redox reaction near the nitrite oxidation peak potential was observed on the L-Arginine/Co_3O_4/FTO electrode in the absence of nitrite (Figure 4.7b). The reversible peak can be attributed to the Co(II)/Co(III) redox couple, according to the following equation (Salimi, Mamkhezri, *et al.*, 2008):

$$Co_3O_4 + H_2O + OH^- \rightarrow 3\ CoOOH + e^- \qquad (4.3)$$

No current response (Figure 4.7a) was observed for bare FTO and L-Arginine/FTO in nitrite suggesting the absence of a redox-active species, i.e., Co_3O_4.

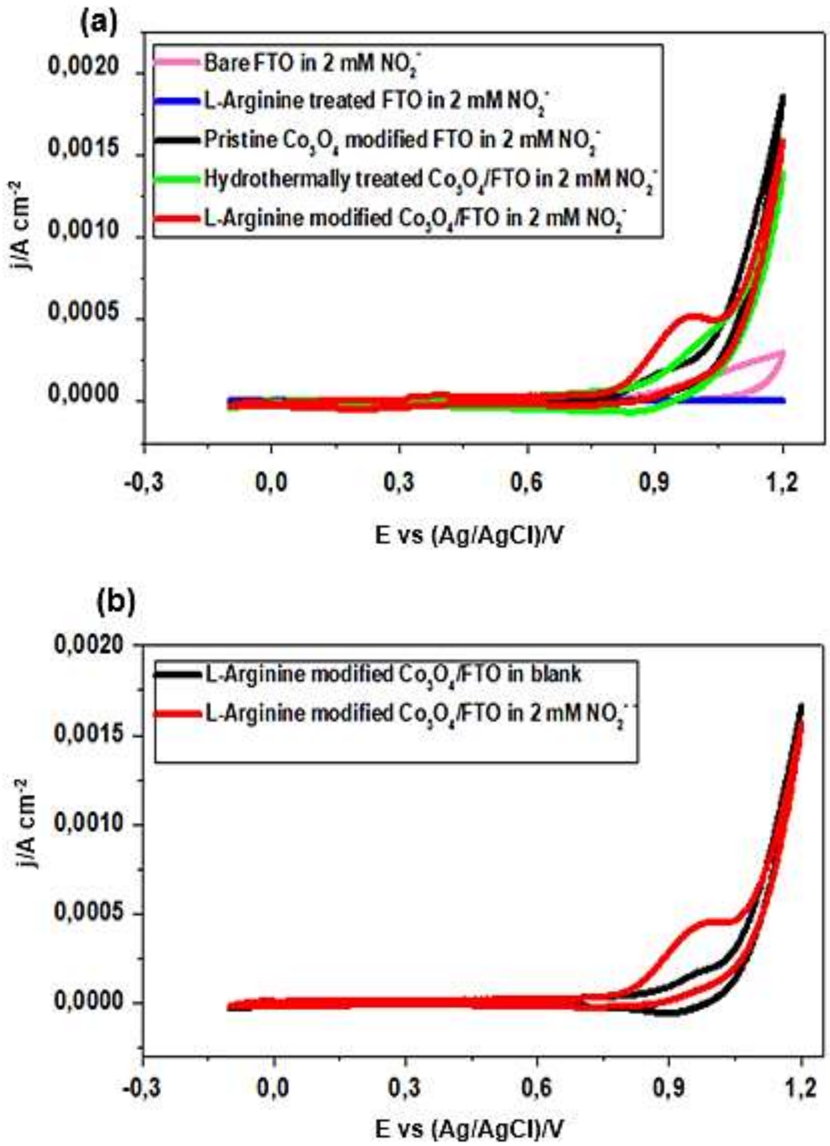

Figure 4.7: (a) CV for the electrooxidation of 2 mM nitrite in 0.1 M PBS (pH = 7.4) at 10 mVs^{-1} and (b) CV of L-Arginine/Co_3O_4/FTO in the presence and absence of 2 mM nitrite

The various scan rate study was conducted to determine the nature of the electrode process at L-Arginine/Co_3O_4/FTO in the presence of nitrite. As presented in Figure 4.8a, the anodic and cathodic (case of low k_{EC} in Figure 2.5) peak currents increased with increasing sweep rate in the range of 10-200 mVs^{-1}. Particularly, the oxidation peak current varied linearly with the square root of scan rate (Figure 4.8b, as is the case with a diffusion-controlled process (Sudha, Mohanty and Thangamuthu, 2018). Some nitrite adsorption on L-Arginine/Co_3O_4/FTO surface was confirmed by Figure 4.8c showing the nearly linear relationship between anodic peak current density and scan rate. It can be seen from Figure 4.8d that the peak potentials increases with scan rate (logv), which suggests that nitrite electro-oxidation at L-Arginine/Co_3O_4/FTO shows some degree of irreversibility (Bard and Faulkner, 2001).

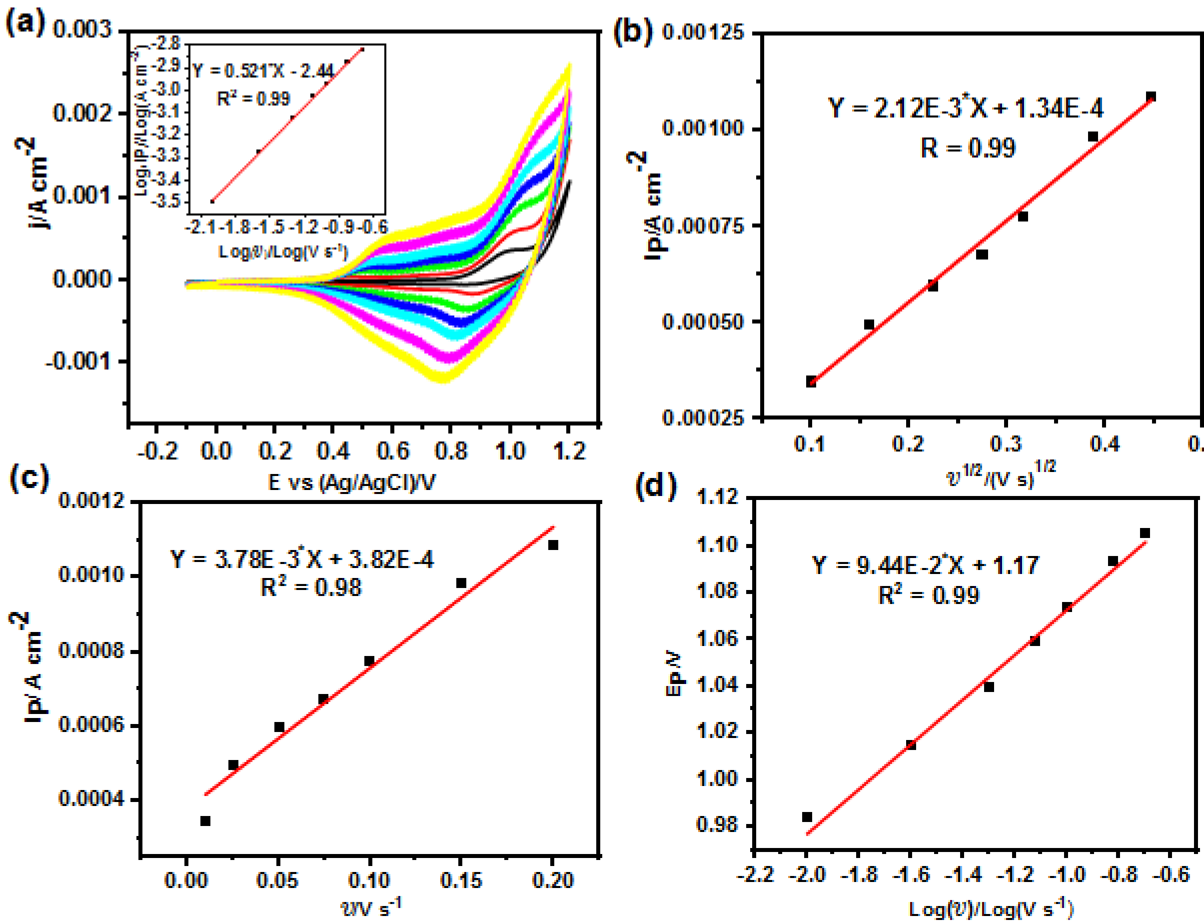

Figure 4.8: (a) Cyclic voltammograms of L-Arginine/Co_3O_4/FTO in 2 mM NO_2^- and 0.1 M PBS (pH = 7.4) at various scan rates (10, 25, 50, 75, 100, 150, and 200 mVs^{-1}). Inset graph shows a logarithmic plot of anodic peak current vs scan rate; (b) anodic peak current density vs square root of scan rate; (c) anodic peak current density vs scan rate, and (d) anodic peak potential vs logarithm of scan rate

The anodic transfer coefficient (α_a) can be derived from the equation given by (Bard and Faulkner, 2001):

$$E_{pa} = I + \frac{2.303RT}{2(\alpha_a)n_aF}\log(v) \tag{4.4}$$

Where E_{pa} is the anodic peak potential (V), I is the E_{pa}-intercept (V), R is the ideal gas constant (8.314 J/mol.K), T is room temperature (298 K), v is the scan rate (mVs^{-1}), and n_a is the number of electrons involved in the rate-determining step, F is the Faraday constant (96500). After mathematical treatment of Equation 4.4, a value of 0.31 was found for $(\alpha_a)n_a$. Considering n_a as unity, the value of α_a = 0.31 (< 0.5) suggests that the activation barrier is on the reactant (reduced species) side. Alternatively, in the absence of a plot of E_{pa} against $\log(v)$, α_a can be easily estimated from a cyclic voltammogram using Matsuda's equation (Matsuda and Ayabe, 1955). Hence, in case of Co_3O_4/FTO (0.883) and HT-Co_3O_4/FTO (0.619), α_a was determined by Matsuda:

$$E_p - E_{\frac{p}{2}} = \frac{0.0477}{(\alpha_a)n_a} \tag{4.5}$$

Where E_p and $E_{p/2}$ are the oxidation peak and half-peak potentials (V), respectively, obtained from Figure 4.7a. α_a for L-Arginine/Co_3O_4/FTO, HT-Co_3O_4/FTO, and Co_3O_4/FTO was used for the calculation of the heterogeneous electron transfer rate constant (k^0). The k^0 values for L-Arginine/Co_3O_4/FTO, HT-Co_3O_4/FTO, and Co_3O_4/FTO were calculated using Equation 4.6 as given below (Islam *et al.*, 2020):

$$I = E^{0\prime} + \frac{RT}{(\alpha_a)n_aF} \times \left\{0.78 + \left(\frac{2.3}{2}\right)\log\left[\frac{(\alpha_a)n_aFD}{(k^0)^2RT}\right]\right\} \tag{4.6}$$

Where, $E^{0\prime}$ is the formal electrode potential (V), estimated here from the cyclic voltammograms in Figure 4.7a using the procedure described in (Espinoza *et al.*, 2019), and D is the diffusion coefficient of nitrite ($1.7 \times 10^{-5}\ cm^2/s$) (Chen *et al.*, 2008). A faster electron transfer process, corresponding to a 50 % increase, occurs at L-Arginine/Co_3O_4/FTO electrode (k^0 = 0.00172 cm/s) compared to pristine Co_3O_4/FTO (k^0 = 0.00116 cm/s) and HT-Co_3O_4/FTO electrode (k^0 = 0.00113 cm/s). This highlights the superior electrochemical activity of the L-Arginine/Co_3O_4/FTO electrode compared to other electrodes studied.

The nitrite sensing capability of L-Arginine/Co_3O_4/FTO was determined in the concentration range from 2 to 19 mM NO_2^- and is shown in Figure 4.9a. The oxidation peak current response of L-Arginine/Co_3O_4/FTO was linearly (R^2 = 0.99) proportional to the nitrite concentration in PBS solution within the investigated range Figure 4.9b. Furthermore, progressive positive shifts of the anodic peak potential with increasing analyte concentration were detected. This phenomenon occurs due to analyte adsorption on the electrode surface as mentioned earlier. Each binding event due the interaction between nitrite and L-Arginine/Co_3O_4/FTO, establishes a new activation overpotential (Sandford *et al.*, 2019).

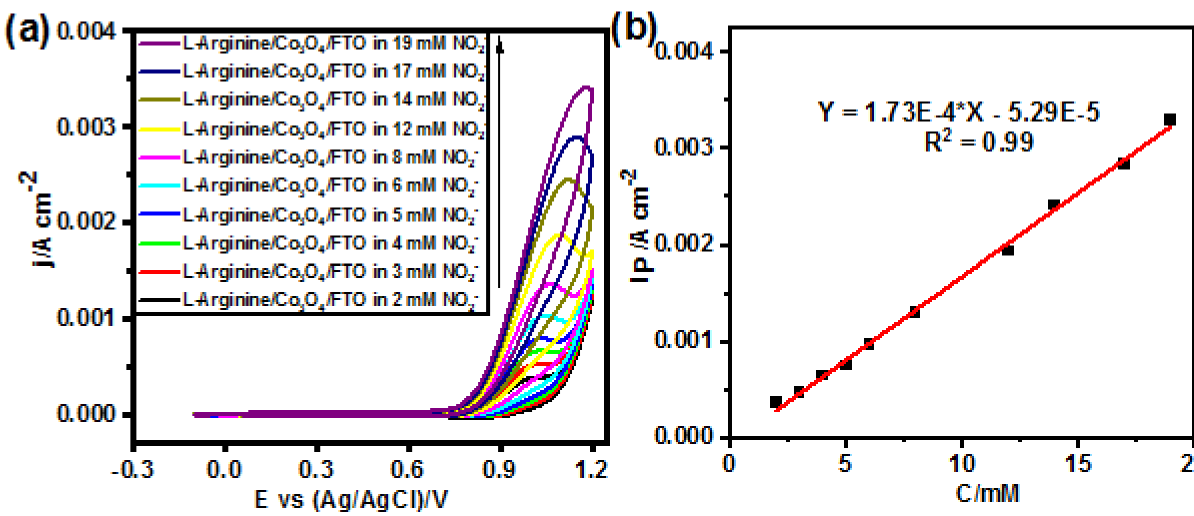

Figure 4.9: (a) Cyclic voltammograms for L-Arginine/Co_3O_4/FTO in the presence of 2 – 19 mM nitrite in 0.1 M PBS (pH = 7.4) at 10 mVs^{-1} and (b) Plot of oxidation peak current density vs nitrite concentration

4.2.2. Electrochemical impedance spectroscopy study of the as prepared electrodes

Electrochemical impedance spectroscopy (EIS) was used to further evaluate the electron transport kinetics of the L-Arginine/Co_3O_4/FTO, HT-Co_3O_4/FTO, and Co_3O_4/FTO electrodes. Corresponding Nyquist spectra are presented in Figure 4.10a. The Nyquist plot is fitted with Randles equivalent circuits as shown in Figure 4.10c, where R_S is the solution resistance, R_{CT} is the charge transfer resistance, C_{DL} is the double layer capacitance, CPE is the constant phase arising from surface inhomogeneity (Etesami *et al.*, 2016), R_W is the Warburg diffusion resistance, Z_W is the semi-infinite Warburg impedance, and $Z_{W\text{-}O}$ is the finite-length Warburg impedance, represented here by the parallel arrangement of CPE and R_W (Nguyen and Breitkopf, 2018). The diameter of the semicircle in the diffusion region for L-Arginine/Co_3O_4/FTO (R_W = 129.2 Ω) is less than that for HT- Co_3O_4/FTO (R_W = 329.5 Ω), which potentially implies better mass transport through L-Arginine/Co_3O_4/FTO owing to its porous surface. CPE exponent (n) for HT-Co_3O_4/FTO, Co_3O_4/FTO, and L-Arginine/Co_3O_4/FTO was found to be 0.79, 0.62, and 0.59, respectively. This decreasing trend can be related to an increase in electrode roughness, as per SEM images. It can be seen from Figure 4.10b that the L-Arginine/Co_3O_4/FTO (R_{CT} = 32.4 Ω) has a smaller charge transfer resistance compared to that of Co_3O_4/FTO (R_{CT} = 47.7 Ω) and HT-Co_3O_4/FTO (R_{CT} = 59.2 Ω) electrodes. The smaller charge transfer resistance for L-Arginine/Co_3O_4/FTO compared with Co_3O_4/FTO and HT-Co_3O_4/FTO is certainly promoted by positively charged functional groups creating more ionic pathways. Moreover, the semicircles in Figure 4.10b show a decreasing trend in the double layer capacitances (values retrieved from EIS data) of the three electrodes, from L-Arginine/Co_3O_4/FTO (C_{DL}= 0.156 µF) through Co_3O_4/FTO (C_{DL}= 0.105 µF) to HT-Co_3O_4/FTO (C_{DL}= 0.091 µF). Normalizing the double layer capacitance by specific capacitance of a smooth planar electrode (assumed C_S = 40 µF/cm^2) gives the electrochemical active surface area (ECSA) (Su *et al.*, 2019). The ECSA were found to be 0.0039, 0.00263 and 0.00228 cm^2 for L-Arginine/Co_3O_4/FTO, Co_3O_4/FTO, and HT-Co_3O_4/FTO, respectively. The higher ECSA for L-Arginine/Co_3O_4/FTO resulted in enhanced electrocatalytic activity compared with the other electrodes studied.

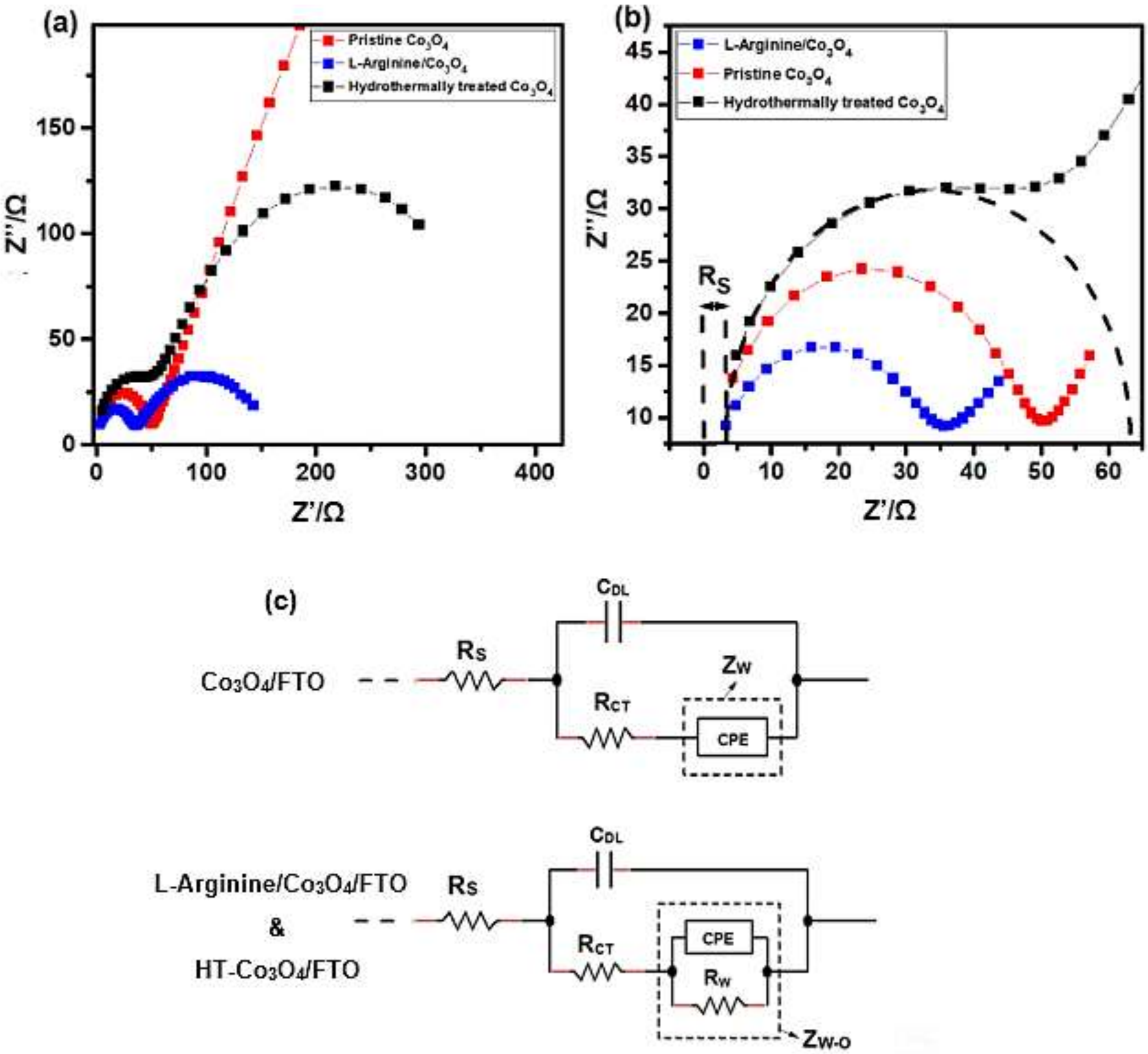

Figure 4.10: (a) Nyquist plots for Co_3O_4/FTO, HT-Co_3O_4/FTO, and L-Arginine/Co_3O_4/FTO in 0.1 M KCl + 5 mM $K_3[Fe(CN)_6]$; (b) The high frequency region of the Nyquist plots and (c) Randles equivalent circuits

Tafel plot was further utilized to support the EIS results, as seen in Figure C.1 (APPENDIX C). It was found that the Tafel slope for L-Arginine/Co_3O_4/FTO (110 mV) is smaller than that for Co_3O_4/FTO (116 mV) and HT-Co_3O_4/FTO (235 mV) due to reduced charge transfer resistance. Table 4.1 presents measured and calculated electrochemical parameters for the prepared electrodes.

Table 4.1. Measured and calculated electrochemical parameters for L-Arginine/Co_3O_4/FTO, Co_3O_4/FTO, and HT-Co_3O_4/FTO. Tafel slope, k^0, [R_{CT}, C_{DL}, R_W, and n], and ECSA were obtained from (1) Tafel plot in Figure C.1, (2) Equation 4.6, (3) EIS data using Randles equivalent circuit, and (4) the division of C_{DL} values by specific capacitance (C_S = 40 μF/cm^2), respectively

Electrode	Tafel Slope (mV)	$k^0 \times 10^3$ (cm/s)	R_{CT} (Ω)	$C_{DL} \times 10$ (μF)	ECSA $\times 10^3$ (cm^2)	R_W (Ω)	n ( )
L-Arginine/ Co_3O_4/ FTO	110	1.72	32.4	1.56	3.90	129.2	0.59
Co_3O_4/ FTO	116	1.16	47.7	1.05	2.63	-	0.62
HT-Co_3O_4/FTO	235	1.13	59.2	0.91	2.28	329.5	0.79

4.2.3. Nitrite sensing mechanism

Based on physical and electrochemical characterisations, it is evident that the low oxidation states of cobalt (Co^0 and Co^{2+}) behave as redox-active sites for the electro-oxidation of nitrite in neutral environment. The occurrence of nitrite oxidation at Co(II) rather than Co(III) in aqueous media can be due to a stabilization effect of nitrite on Co(III). Nitrite (N-bonded) as a strong field ligand (Tsuchida, 1938) can stabilize Co(III) (low spin), decreasing by that means the reducing tendency and oxidizing power of Co(III), and resulting into the preferential interaction of nitrite with Co(II) (Rizvi, 2015). The following reaction mechanism is proposed for the interaction of nitrite at L-Arginine/Co_3O_4/FTO:

a) The metallic phase of cobalt (Co^0) has additive effect on the amount of divalent cobalt (Co^{2+}) in solution (Equation 4.7);
b) The reaction proceeds via the formation of an adduct between cobalt oxide and nitrite through the divalent cobalt (Co^{2+}) (Equation 4.8);
c) A slow, one-electron transfer process involving the simultaneous oxidation of Co^{2+} and NO_2^- to Co^{3+} and NO_2, occurs (Equation 4.9). This is evidenced by the CV experiment in Figure 4.7b for L-Arginine/Co_3O_4/FTO;

d) Finally, NO_2 undergoes disproportionation (Equation 4.10-4.11) and Co^{3+} is reduced to Co^{2+} (Equation 4.12).

$$(Co^{0}Co^{2+})\ (\text{L-Arginine}/Co_3O_4/\text{FTO}) + H_2O \rightarrow Co^{2+}(\text{L-Arginine}/Co_3O_4/\text{FTO}) + 2e^{-} \quad (4.7)$$

$$Co^{2+}(\text{L-Arginine}/Co_3O_4/\text{FTO}) + NO_2^{-} \leftrightarrow Co^{2+}(NO_2^{-})(\text{L-Arginine}/Co_3O_4/\text{FTO}) \quad (4.8)$$

$$[Co^{2+}(NO_2^{-})(\text{L-Arginine}/Co_3O_4/\text{FTO})] \leftrightarrow Co^{3+}(\text{L-Arginine}/Co_3O_4/\text{FTO}) + NO_2 \quad (4.9)$$

$$2\ NO_2 + H_2O \leftrightarrow 2\ H^{+} + NO_3^{-} + NO_2^{-} \quad (4.10)$$

$$NO_2^{-} + H_2O \rightarrow 2\ H^{+} + NO_3^{-} + 2e^{-} \quad (4.11)$$

$$Co^{3+}(\text{L-Arginine}/Co_3O_4/\text{FTO}) \rightarrow Co^{2+}(\text{L-Arginine}/Co_3O_4/\text{FTO}) + e^{-} \quad (4.12)$$

4.3. Chronoamperometric study of the as prepared electrode

Chronoamperometry measurements (Figure 4.11a) were conducted in the presence of successive injection of nitrite under mild stirred condition and at a fixed potential of 0.96 V vs Ag/AgCl. The sensor exhibited a sensitivity of 158 µA/mM cm^{-2} and linear range of up to 16 mM (Figure 4.11b). An ultra-fast steady state response time of < 2 s was also observed. The limit of detection (LOD) was calculated using the formula 3σ/S (Zhao *et al.*, 2019), with σ, being the standard deviation of the response (estimated by the standard deviation of y-intercepts) (Shrivastava and Gupta, 2011) and S, is the sensitivity. The calculated LOD (1.95 nM) is significantly lower than the maximum allowable nitrite concentration in drinking water (65 µM) in accordance with WHO. This qualifies the fabricated sensor for practical applications, including nitrite detection in drinking water. The obtained sensor performance characteristics were compared with literature, as reported in Table 4.2. Most of the sensor data presented in the literature (Table 4.2) uses a glassy carbon as substrate. This approach is not commercially viable. Moreover, the as prepared sensor reported in this study showed a combination of ultra-low limit of detection, ultra-fast response time, high sensitivity & selectivity, and wide linear range. Such electrochemical nitrite sensor performance characteristics combination is rare in the reported literature. This makes the developed sensor a potential candidate for commercial application.

The selectivity of L-Arginine/Co_3O_4/FTO towards nitrite oxidation was evaluated in the presence of interfering species that may coalesce with nitrite during its detection. A five times higher concentration than that of nitrite was used in 0.1 M PBS solution for each of the following interfering substances: Na_2CO_3, $(NH_4)_2SO_4$, $NaNO_3$, glucose, KCl, NaCl, urea, oxone, and $MgSO_4$. As prepared L-Arginine/Co_3O_4/FTO sensor was only responsive to nitrite injection and the presence of interferents did not reduce the sensor response, as seen in Figure 4.11c. It is more likely that the interfering cations (Na^+, NH_4^+, K^+, and Mg^{2+}) will experience charge repulsion due to positively charged functional groups immobilized on L-Arginine/Co_3O_4/FTO. Also, the enrichment of neutral organic compounds like glucose and urea on the surface of L-Arginine/Co_3O_4/FTO can be prevented because of the competition with anionic species. The excellent selectivity of L-Arginine/Co_3O_4/FTO towards nitrite compared with the other anions investigated agrees largely with the Hofmeister series (Zare *et al.*, 2005), except for nitrate which deviated from Hofmeister pattern. Another possible explanation for the good selectivity could be the interfering anions (CO_3^{2-}, SO_4^{2-}, HSO_5^-, HSO_4^-, NO_3^-, and Cl^-) as weak-field ligands interact weakly with the divalent cobalt on L-Arginine/Co_3O_4/FTO in aqueous solution. Nitrite (N-bonded), on the contrary, is a stronger field ligand and gives rise to bigger coordination forces.

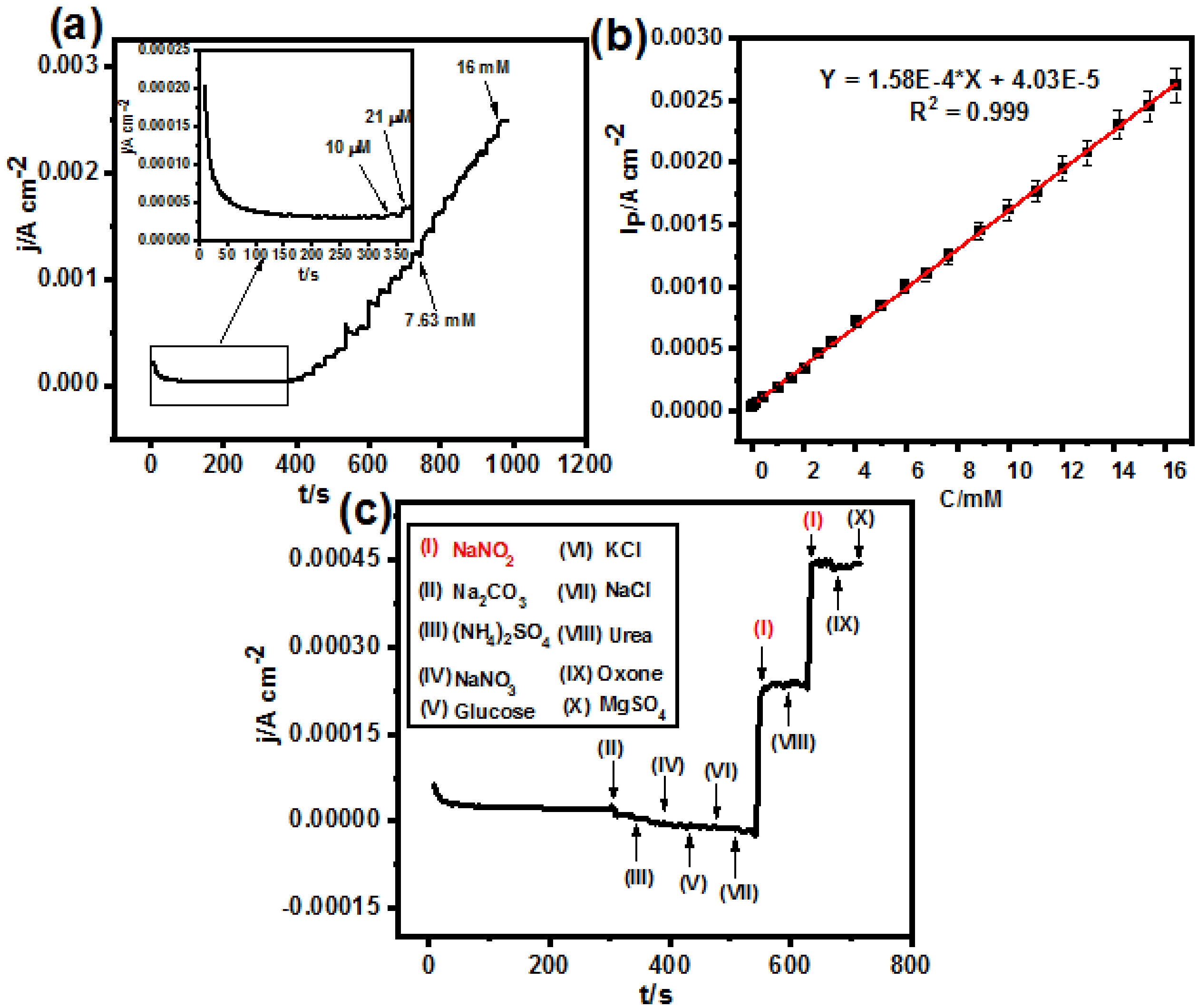

Figure 4.11: (a) Chronoamperometry data for L-Arginine/Co_3O_4/FTO in 0.1 M PBS (pH = 7.4), (b) Dose response curve of the as prepared electrode, and (c) Interference study of L-Arginine/Co_3O_4/FTO for nitrite in 0.1 M PBS and in the presence of Na_2CO_3, $(NH4)_2SO_4$, $NaNO_3$, glucose, KCl, NaCl, urea, oxone, and $MgSO_4$

Table 4.2. Comparison of performance characteristics of the developed electrochemical nitrite sensors with the reported sensors in literature

Modified Electrode	Technique	Electrolyte	pH	E/mV	C/μM	S/μA mM^{-1}	LOD/μM	Reference
[a](FeT4MPyP + CoTSPc)/GCE	Amperometry	PBS	7	850 vs SCE	0.2 - 8.6	0.37	0.04	(Santos *et al.*, 2006)
[b]Co_3O_4/RGO/GCE	Amperometry	KOH	14	-	1 - 380	2065	0.14	(Haldorai *et al.*, 2016)
[c]CoTBMPc-Au	CV	PBS	7.4	750 vs Ag/AgCl	100 - 1000	7.3×10^{-3}	-	(Agboola and Nyokong, 2007)
[d]CoTDMPc-Au	CV	PBS	7.4	770 vs Ag/AgCl	100 - 1000	7.1×10^{-3}	-	(Agboola and Nyokong, 2007)
[e]CoO_x/CNT/GCE	Amperometry	PBS	6.76	750 vs SCE	0.5 - 249	5.619×10^{-2}	0.3	(Meng *et al.*, 2011)
[f]polyNiCo/GCE	Amperometry	PBS	7	-	2.49 - 1700	0.027	0.45	(Islam *et al.*, 2020)
	CV	PBS	7	850 vs Ag/AgCl	100 - 5000	0.042	10	
[g]Co_3O_4-DCS/GCE	Amperometry	PBS	7	900 vs SCE	6.6 - 3000	0.318	0.22	(Sudha, Mohanty and Thangamuthu, 2018)
					3000 - 13830	0.6		
[h]Pt/CoO/GCE	Amperometry	PBS	6	900 vs SCE	0.2 - 3670	0.9014	0.067	(Lu, 2019)
					3670 - 23700	0.4085		
[i]NC/GCE	Amperometry	PBS	7	900 vs SCE	5 - 4000	1.21×10^{-4}	0.002	(Lu, Yang and Nie, 2017)
[j]$(CoTsPc/PDDA\text{-}Gr)_n$/GCE	Amperometry	PBS	5	800 vs SCE	2 - 36	5.3×10^{-3}	0.084	(Cui *et al.*, 2013)

[k]EPPGE-SWCNT-Co	CV	PBS	7.4	900 vs Ag/AgCl	0 - 189	0.2496	5.61	(Adekunle, Pillay and Ozoemena, 2010)
[L]CoPc/MWCNTs/GCE	DPV	PBS	7.4	972 vs Ag/AgCl	10 - 1050000	4×10^{-5}	2.11	(Lu *et al.*, 2020)
[m]CoPcF-MWCNTs/GCE	Amperometry	PBS	7	800 vs SCE	0.096 - 340	0.0299	0.062	(Li *et al.*, 2013)
[n]Co_3O_4-rGO/CNTs/GCE	Amperometry	PBS	7	800 vs Ag/AgCl	0.1 - 8000	0.08	0.016	(Zhao *et al.*, 2019)
[o]Co@Pt/Gr	Amperometry	PBS	6	850 vs Ag/AgCl	1 - 2000	4.596×10^{-2}	0.145	(Abdel Hameed and Medany, 2019)
					2000 - 15000	9.771×10^{-2}		
[p]CoNS/GO/PPy/GCE	CV	PBS	8	800 vs SCE	1 - 3167	0.5192	0.0147	(Wang and Hui, 2017)
[q]CoTM-QOPc/CNP/GCE	CV	PBS	7	790 vs Ag/AgCl	0.2−200	2.3	0.06	(Jilani *et al.*, 2020)
	DPV	PBS	7	740 vs Ag/AgCl	0.2−225	1.03	0.06	
	Amperometry	PBS	7	740 vs Ag/AgCl	0.1−350	1.24	0.033	
[r]CuO-NS/GCE	DPV	PBS	7	850 vs SCE	100-1400	6.17×10^{-3}	13.6	(Sudha *et al.*, 2018)
[s](HOOC-MWCNT)/GCE	DPV	PBS	7	720 vs SCE	100-700	0.2099	0.565	(Sudha, Senthil Kumar and Thangamuthu, 2018)
[t]L-Arginine/Co_3O_4/FTO	Amperometry	PBS	7.4	960 vs Ag/AgCl	10 - 16000	158	0.00195	This work

[a](FeT4MPyP + CoTSPc)/GCE: glassy carbon electrode modified with alternated layers of iron(III) tetra-(N-methyl-4-pyridyl)-porphyrin and cobalt(II) tetrasulfonated phthalocyanine. [b]Co_3O_4/RGO/GCE: cobalt oxide nanospindles-decorated reduced graphene oxide composite on GCE. [c]CoTBMPc-Au & [d]CoTDMPc-Au: Co(II) tetrakis (benzylmercapto) and tetrakis (dodecylmercapto) phthalocyanines electrodeposited onto a gold electrode. [e]CoO_x/CNT/GCE: cobalt oxide nanoparticles on multi-walled carbon nanotubes deposited on a conventional GCE. [f]polyNiCo/GCE: Ni(II) and Co(II)- bisterpyridine ligand based heterometallo SMP. [g]Co_3O_4-DCS/GCE: glassy carbon electrode modified with cobalt oxide disordered circular sheet. [h]Pt/CoO/GCE: platinum nanoclusters doped CoO nanohybrid on GCE. [i]NC/GCE: urchin-like nickel-cobalt carbonate hollow spheres on GCE. [j]$(CoTsPc/PDDA\text{-}Gr)_n$/GCE: graphene/cobalt phthalocyanine composite film on activated GCE. [k]EPPGE-SWCNT-Co: edge plane pyrolytic graphite electrode (with cobalt nanoparticles integrated with single-walled carbon nanotubes. [L]CoPc/MWCNTs/GCE: GCE modififed with cobalt (II) phthalocyanine immobilized on multiwalled carbon nanotubes. [m]CoPcF-MWCNTs/GCE: cobalt phthalocyanine functionalized multiwalled carbon nanotubes on GCE. [n]Co_3O_4-rGO/CNTs/GCE: cobalt oxide decorated reduced graphene oxide and carbon nanotubes on GCE. [o]Co@Pt/Gr: cobalt @ platinum nanoparticles-decorated graphene. [p]CoNS/GO/PPy/GCE: cobalt nanostructures, graphene oxide-doped polypyrrole modified GCE. [q]CoTM-QOPc/CNP/GCE: cobalt (II) tetra methyl-quinoline oxy bridged phthalocyanine carbon nano particles modified glassy carbon electrode. [r]CuO-NS/GCE: Copper oxide nanosheet modified GCE. [s](HOOC-MWCNT)/GCE: Acid-functionalized multi-walled carbon nanotubes modified GCE. [t]L-Arginine/Co_3O_4/FTO: L-Arginine modified cobalt oxide thin film on FTO.

4.4. Electrochemical stability and reproducibility study of the as prepared electrode

Cyclic voltammetry (CV) and chronoamperometry were used to study the stability and reproducibility of the L-Arginine/Co_3O_4/FTO sensor. The electrochemical stability test is shown in Figure 4.12a. The absence of any additional peaks after 25th cycle highlights the electrochemical stability of the as prepared sensor. For reproducibility, five independent electrodes were tested using CV and individual current responses were compared as depicted in the histogram presented in Figure 4.12b. A relative standard deviation (% RSD) of 1.52 % was obtained. This highlights the excellent reproducibility of L-Arginine/Co_3O_4/FTO electrode. In addition, long-term chronoamperometric study (Figure 4.12c) revealed that oxidation current response decreased only by 12 % over a period of 19 min.

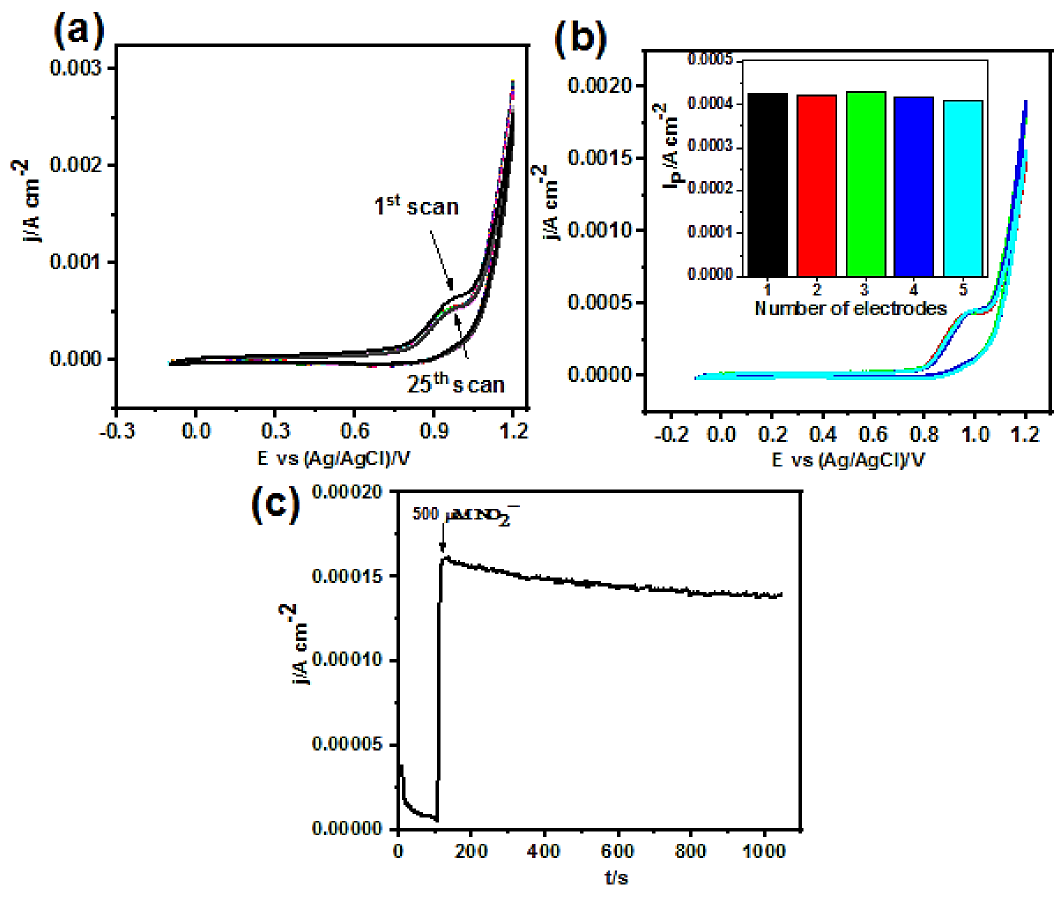

Figure 4.12: (a) Stability study of L-Arginine/Co_3O_4/FTO in the presence of 2 mM nitrite in 0.1 M PBS at 10 mVs^{-1} for 25 scans; (b) Reproducibility test of five different L-Arginine/Co_3O_4/FTO electrodes in the presence of 2 mM nitrite in 0.1 M PBS at 10 mVs^{-1} and (c) Long-term chronoamperometry of L-Arginine/Co_3O_4/FTO in the presence of 500 μM nitrite in in 0.1 M PBS over 19 min

4.5. Detection of nitrite in real sample

The real sample test was carried following the protocol described in (Shivakumar *et al.*, 2017). The recovery study in tap water sample was conducted to investigate the practical application of L-Arginine/Co_3O_4/FTO electrode for nitrite detection. For this reason, tap water samples were diluted with 0.1 M PBS solution (pH = 7.4) and tested for nitrite ions. The test results are summarized in Table 4.3. It can be seen from Table 4.2 that the sensor shows good recovery rates ranging from 96.8 % to 101.7 %, with an average value of 99.9 %.

Table 4.2. Recovery study of nitrite ions in tap water

Sample	Spiked (mM)	Found (mM)	Recovery (%)
Tap water	0.60	0.61	101,7
	1.40	1.41	100.7
	1.50	1.54	102.7
	1.70	1.66	97.6
	2.50	2.42	96.8

CHAPTER 5: CONCLUSIONS AND FUTURE RESEARCH

In summary, L-Arginine/Co_3O_4/FTO exhibited enhanced electrochemical nitrite detection compared to Co_3O_4/FTO and HT-Co_3O_4/FTO. The proposed nitrite sensor showed a combination of ultralow limit of detection (1.95 nM), fast response time (< 2 s), wide linear range (10 – 16000 µM), high sensitivity (158 µA/mM.cm^{-2}) and selectivity compared to the reported literature. The enhanced electrochemical performance originated from: 1) the faster electron transport kinetics, which is a result of nitrogen doping and surface functional groups (i.e., $CH_6N_3^+$ and NH_3^+), 2) the availability of higher ECSA (increased amount of Co^0 and Co^{2+} as active sites due to N doping), and 3) the easy access to active sites and better mass transport kinetics promoted by the porous surface of L-Arginine/Co_3O_4/FTO.

5.1. Conclusion

We have successfully improved the electrochemical properties of Co_3O_4 thin film via ($CH_6N_3^+$, NH_3^+)-functionalization and nitrogen doping of the film in the presence of L-Arginine under optimized hydrothermal conditions. Spectral evidence is presented on how hydrothermal treatment can reduce oxygen vacancy and how nitrogen atoms can compete for substitution into Co_3O_4 crystal lattice. This technique can serve as a new platform for post-deposition element doping and surface functionalization of metal oxides for various sensing applications.

5.2. Future scope and recommendations

- The soft chemical route presented in this study should be tested on a nanocomposite of Co_3O_4 and carbon/rGO for enhanced electrochemical nitrite detection.
- The influence of pH on the peak current and potential of nitrite oxidation at L-Arginine/Co_3O_4/FTO should be studied. However, L-Arginine side-chain has such high pKa-value that it remains acidic over a wide pH range and may resist the pH change, leading to stable anodic peak current.
- The electroanalysis for the oxygen evolution reaction at L-Arginine/Co_3O_4/FTO is suggested as the Co_3O_4 film is N-doped.
- HT-Co_3O_4/FTO electrode has high field emission properties and its application as field emission device should be demonstrated.

BIBLIOGRAPHY

1. Abdel Hameed, R. M. and Medany, S. S. 2019. Evaluation of core-shell structured cobalt@platinum nanoparticles-decorated graphene for nitrite sensing, *Synthetic Metals*, 247(November 2018), pp. 67–80. doi: 10.1016/j.synthmet.2018.11.011.
2. Abegunde, O.O., Akinlabi, E.T., Oladijo, O.P., Akinlabi, S. and Ude, A.U. 2019. Overview of thin film deposition techniques, *AIMS Materials Science*, 6(2), pp. 174–199. doi: 10.3934/MATERSCI.2019.2.174.
3. Adekunle, A. S., Pillay, J. and Ozoemena, K. I. 2010. Probing the electrochemical behaviour of SWCNT-cobalt nanoparticles and their electrocatalytic activities towards the detection of nitrite at acidic and physiological pH conditions, *Electrochimica Acta*, 55(14), pp. 4319–4327. doi: 10.1016/j.electacta.2009.02.102.
4. Agboola, B. and Nyokong, T. 2007. Comparative electrooxidation of nitrite by electrodeposited Co(II), Fe(II) and Mn(III) tetrakis (benzylmercapto) and tetrakis (dodecylmercapto) phthalocyanines on gold electrodes, *Analytica Chimica Acta*, 587(1), pp. 116–123. doi: 10.1016/j.aca.2007.01.031.
5. Amri, A., Duan, X., Yin, C., Jiang, Z., Rahman, M.M. and Pryor, T. 2013. Applied Surface Science Solar absorptance of copper – cobalt oxide thin film coatings with nano-size , grain-like morphology : Optimization and synchrotron radiation XPS studies, *Applied Surface Science*, 275, pp. 127–135. doi: 10.1016/j.apsusc.2013.01.081.
6. An, D., Wang, L., Zheng, Y., Guan, S., Gao, X., Tian, Y., Zhang, H., Wang, Z. and Liu, Y. 2009. In situ preparation and surface modification of magnesium hydroxide nanoparticles, *Colloids and Surfaces A: Physicochemical and Engineering Aspects*, 348(1–3), pp. 9–13. doi: 10.1016/j.colsurfa.2009.06.004.
7. Astier, Y., Canters, G.W., Davis, J.J., Hill, H.A.O, Verbeet, M.P. and Wijma, H.J. 2005. Sensing nitrite through a pseudoazurin-nitrite reductase electron transfer relay, *ChemPhysChem*, 6(6), pp. 1114–1120. doi: 10.1002/cphc.200400384.
8. Bard, A. J. and Faulkner, L. R. 200. *Electrochemical methods: fundamentals and applications*. 2nd ed. Edited by D. Harris et al. New York: John Wiley & Sons, Inc.
9. Beckel, D., Hütter, A.B., Harvey, A., Infortuna, A., Muecke, U.P., Prestat, M., Rupp, J.L.M. and Gauckler, L.J. 2007. Thin films for micro solid oxide fuel cells, *Journal of Power Sources*, 173(1), pp. 325–345. doi: 10.1016/j.jpowsour.2007.04.070.
10. Betancur, Y., Sanchez, A., Bueno-Lopez, A. and Lopez, D. 2018. Potassium Catalytic Effect on Gasification Reactions of Coal and Coal/Biomass Blends under Oxy-combustion Conditions. An Isotopic Study Using $^{13}C^{18}O2$, *Energy and Fuels*, 32(2), pp. 2439–2449. doi: 10.1021/acs.energyfuels.7b03399.
11. Biswas, B. K., Inoue, K., Ghimire, K.N., Ohta, S., Harada, H., Ohto, K. and Kawakita, H. 2007. The adsorption of phosphate from an aquatic environment using metal-loaded orange waste, *Journal of Colloid and Interface Science*, 312(2), pp. 214–223. doi: 10.1016/j.jcis.2007.03.072.
12. Biswas, M. and Su, P.-C. 2017. Chemical Solution Deposition Technique of Thin-Film Ceramic Electrolytes for Solid Oxide Fuel Cells, *Modern Technologies for Creating the Thin-film Systems and Coatings*, (May). doi: 10.5772/66125.
13. Bochenkov, V. E. and Sergeev, G. B.(2007. Nanomaterials for sensors, *Russian Chemical Reviews*, 76(11), pp. 1084–1093. doi: 10.1070/rc2007v076n11abeh003735.
14. Bora, D. K., Braun, A., Erni, R., Fortunato, G., Graule, T. and Constable, E.C. 2011. Hydrothermal treatment of a hematite film leads to highly oriented faceted nanostructures with enhanced photocurrents, *Chemistry of Materials*, 23(8), pp. 2051–2061. doi: 10.1021/cm102826n.
15. Braida, W. and Ong, S. K. 2000. Decomposition of nitrite under various pH and aeration conditions, *Water, Air, and Soil Pollution*, 118(1–2), pp. 13–26. doi:

10.1023/a:1005193313166.
16. Brender, J. D., Olive, J.M., Felkner, M., Suarez, L., Marckwardt, W. and Hendricks, K.A. 2004. Dietary nitrites and nitrates, nitrosatable drugs, and neural tube defects, *Epidemiology*, 15(3), pp. 330–336. doi: 10.1097/01.ede.0000121381.79831.7b.
17. Brinker, C. J., Frye, G.C., Hurd, A.J. and Ashley, C.S. 1991. Fundaments of sol-gel coating, *Thin Solid Films*, 201, pp. 97–108.
18. Butler, L. R. P., Laqua, K. and Strasheim, A. 1986. Nomenclature, symbols, units and their usage in spectrochemical analysis—V radiation sources, *Spectrochimica Acta - Part B Atomic Spectroscopy*, 41(5), pp. 507–544. doi: 10.1016/0584-8547(86)80190-2.
19. Cao, A. M., Hu, J.S., Liang, H.P., Song, W.G., Wan, L.J., He, X.L., Gao, X.G. and Xia, S.H. 2006. Hierarchically structured cobalt oxide (Co_3O_4): The morphology control and its potential in sensors, *Journal of Physical Chemistry B*, 110(32), pp. 15858–15863. doi: 10.1021/jp0632438.
20. Cao, H. and Wang, J. 2008. Amino-acid-assisted synthesis and size-dependent magnetic behaviors of hematite nanocubes, *Applied Physics Letters*, 92(1), pp. 1–4. doi: 10.1063/1.2830699.
21. Chen, J., Wu, X. and Selloni, A. 2011. Electronic structure and bonding properties of cobalt oxide in the spinel structure, *Physical Review B - Condensed Matter and Materials Physics*, 83(24), pp. 1–24. doi: 10.1103/PhysRevB.83.245204.
22. Chen, L. H., Zang, J.B., Wang, Y.H. and Byan, L.Y. 2008. Electrochemical oxidation of nitrite on nanodiamond powder electrode, *Electrochimica Acta*, 53(8), pp. 3442–3445. doi: 10.1016/j.electacta.2007.12.023.
23. Cho, S., Yoon, K.R., Shin, K., Jung, J., Kim, C., Cheong, J.Y., Youn, D., Song, S.W., Henkelman, G. and Kim, I. 2018. Synergistic Coupling of Metallic Cobalt Nitride Nano fi bers and IrO_x Nanoparticle Catalysts for Stable Oxygen Evolution, *Chemistry of Materials*, 30, pp. 5941–5950. doi: 10.1021/acs.chemmater.8b02061.
24. Chowdhury, M., Cummings, F., Kebede, M.A. and Fester, V. 2017. Binderless Solution Processed Zn Doped Co_3O_4 Film on FTO for Rapid and Selective Non-enzymatic Glucose Detection, *Electroanalysis*, 29(2), pp. 578–586. doi: 10.1002/elan.201600440.
25. Chowdhury, M., Ossinga, C., Cummings, F., Chamier, J. and Kebede, M. 2017. Novel Sn Doped Co_3O_4 Thin Film for Nonenzymatic Glucose Bio-Sensor and Fuel Cell, *Electroanalysis*, 29(8), pp. 1876–1886. doi: 10.1002/elan.201700184.
26. Coşofreţ, V. V. and Buck, R. P. 2018. *Pharmaceutical applications of membrane sensors*, *Pharmaceutical Applications of Membrane Sensors*. doi: 10.1201/9781351075497.
27. Cui, C., Lin. R., Xu, C., Wang, J. and Li, Z. 2018. Hybrid cobalt-based electrocatalysts with adjustable compositions for electrochemical water splitting derived from Co^{2+}-Loaded MIL-53(Fe) particles, *Electrochimica Acta*, 53. doi: 10.1016/j.electacta.2018.08.046.
28. Cui, L., Pu, T., Liu, Y. and He, X. 2013. Layer-by-layer construction of graphene/cobalt phthalocyanine composite film on activated GCE for application as a nitrite sensor, *Electrochimica Acta*, 88, pp. 559–564. doi: 10.1016/j.electacta.2012.10.127.
29. Cui, Y., Yang, C., Zeng, W., Oyama, M., Pu, W. and Zhang, J. 2007. Electrochemical determination of nitrite using a gold nanoparticles-modified glassy carbon electrode prepared by the seed-mediated growth technique, *Analytical Sciences*, 23(12), pp. 1421–1425. doi: 10.2116/analsci.23.1421.
30. Deng, Y., Wang, T., Zhu, L., Jia, A., Lu, J. and Luo, M. 2018. Enhanced performance of CO oxidation over $Pt/CuCrO_x$ catalyst in the presence of CO_2 and H_2O, *Applied Surface Science*, 442, pp. 613–621. doi: 10.1016/j.apsusc.2018.02.099.
31. Diallo, A., Beye, A.C., Doyle, T.B., Park, E. and Maaza, M. 2015. Green synthesis of Co_3O_4 nanoparticles via Aspalathus linearis: Physical properties, *Green Chemistry Letters and Reviews*, 8(3–4), pp. 30–36. doi: 10.1080/17518253.2015.1082646.

32. Dou, M., He, D., Shao, W., Liu, H., Wang, F. and Dai, L. 2016. Pyrolysis of Animal Bones with Vitamin B12 : A Facile Route to Efficient Transition Metal – Nitrogen – Carbon TM-*N*-C) Electrocatalysts for Oxygen Reduction, 44106, pp. 2896–2901. doi: 10.1002/chem.201504983.
33. Dupin, J.C., Gonbeau, D., Vinatier, P. and Levasseur, A. 2000. Systematic XPS studies of metal oxides, hydroxides and peroxides, *Physical Chemistry Chemical Physics*, 2(6), pp. 1319–1324. doi: 10.1039/a908800h.
34. Eby, D.M., Artyushkova, K., Paravastu, A.K. and Johnson, G.R. 2012. Probing the molecular structure of antimicrobial peptide-mediated silica condensation using X-ray photoelectron spectroscopy, *Journal of Materials Chemistry*, 22(19), pp. 9875–9883. doi: 10.1039/c2jm30837a.
35. Eskalen, H., Kerli, S. and Özgan, Ş. 2017. Hydrothermally Produced Cobalt Oxide Nanostructures at Different Temperatures and Effect on Phase Transition Temperature and Threshold Voltage of Nematic Liquid Crystal Host, in *Cobalt*, pp. 71–85. doi: 10.5772/intechopen.70946.
36. Espinoza, E. M., Clark, J.A., Soliman, J., Derr, J.B., Morales, M. and Vulley, V.I. 2019. Practical Aspects of Cyclic Voltammetry : How to Estimate Reduction Potentials When Irreversibility Prevails Practical Aspects of Cyclic Voltammetry : How to Estimate Reduction Potentials When Irreversibility Prevails, *Journal of The Electrochemical Society,* 166(5). doi: 10.1149/2.0241905jes.
37. Etesami, M., Nurul, S.N., Chandran, M.S., Hussin, M.H., Ripin, A., Adnan, R., Ngilmi, A., Suraji, A. and Mohammed, N. 2016. Electrooxidation of Nitrite Ions on Gold / Polyaniline / Carbon Paste Electrode, *International Journal of Electrochemical Science,* 11 (2016), pp. 8332–8345. doi: 10.20964/2016.10.32.
38. Bufaical, L., Finkler, R., Coutrim, L.T., Pagliuso, P.G., Grossi, C., Stavale, F., Saitovitch, B. and Bittar, E.M. 2018. Training-induced inversion of spontaneous exchange bias field on $La_{1.5}Ca_{0.5}CoMnO_6$, *Journal of Magnetism and Magnetic Materials,* 433 pp. 271–277.
39. Fisher, A. C. 2010. *Electrochemistry Teaching Notes*, Department of Chemical Engineering and Biiotechnology, University of Cambridge.
40. Freire, P. T. C., Barboza, F.M., Lima, J.A., Melo, F.E.A. and Filho, J.M. 2017. Raman Spectroscopy of Amino Acid Crystals, *Raman Spectroscopy and Applications*. doi: 10.5772/65480.
41. Gangarajula, Y. and Gopal, B. 2012. Spinel cobalt oxide catalyzed controlled hydration of aromatic nitriles, *Chemistry Letters*, 41(1), pp. 101–103. doi: 10.1246/cl.2012.101.
42. Gota, T., Chowdhury, M. and Ojumu, T. 2017. Non-enzymatic Fructose Sensor Based on Co_3O_4 Thin Film, *Electroanalysis*, 29(12), pp. 2855–2862. doi: 10.1002/elan.201700503.
43. Haldorai, Y., Kim, J.Y., Vilian, A.T.E., Heo, N.S., Huh, Y.S. and Han, Y.K. 2016. An enzyme-free electrochemical sensor based on reduced graphene oxide/Co_3O_4 nanospindle composite for sensitive detection of nitrite, *Sensors and Actuators B: Chemical*, 227, pp. 92–99. doi: 10.1016/j.snb.2015.12.032.
44. Halim, J., Cook, K.M., Naguib, M., Eklund, P., Gogotsi, Y., Rosen, J. and Barsoum, M.W. 2016. X-ray photoelectron spectroscopy of select multi-layered transition metal carbides (MXenes), *Applied Surface Science*, 362, pp. 406–417. doi: 10.1016/j.apsusc.2015.11.089.
45. Han, B., Choi, K.H., Park, K. and Han, W.S. 2012. Low-temperature atomic layer deposition of cobalt oxide thin films using dicobalt hexacarbonyl tert-butylacetylene and ozone, *Electrochemical and Solid-State Letters*, 15(2), pp. 2012–2015. doi: 10.1149/2.008202esl.
46. Hao, Q., Morton, S.M., Wang, B., Zhao, Y., Jensen, L. and Huang, T.J. 2013. Tuning surface-enhanced Raman scattering from graphene substrates using the electric field effect and chemical doping, *Applied Physics Letters*, 102(1). doi: 10.1063/1.4755756.
47. Harry, M., Chowdhury, M., Cummings, F. and Arendse, C.J. 2019. Elemental Cu doped

Co_3O_4 thin film for highly sensitive non-enzymatic glucose detection, *Sensing and Bio-Sensing Research*, 23, p. 100262. doi: 10.1016/J.SBSR.2019.100262.
48. He, D., Zhang, Z. Huang, Y. and Hu, Y. 2007. Chemiluminescence microflow injection analysis system on a chip for the determination of nitrite in food, *Food Chemistry*, 101(2), pp. 667–672. doi: 10.1016/j.foodchem.2006.02.024.
49. Herrera, A.P., Corrales, L.P., Chvez, E., Bolivar, J.C., Uwakweh, O.N.C. and Rinaldi, C. 2013. Influence of aging time of oleate precursor on the magnetic relaxation of cobalt ferrite nanoparticles synthesized by the thermal decomposition method, *Journal of Magnetism and Magnetic Materials*, 328, pp. 41–52. doi: 10.1016/j.jmmm.2012.09.069.
50. Herrklotz, J.V. 2012. *Analysis of the vibrational spectra of L-lysine and L-arginine*, p. 140.
51. Honikel, K. O. 2008. The use and control of nitrate and nitrite for the processing of meat products, *Meat Science*, 78(1–2), pp. 68–76. doi: 10.1016/j.meatsci.2007.05.030.
52. Hosoya, S. 1999. Sulfuric acid bleaching of kraft pulp II: Behavior of lignin and carbohydrate during sulfuric acid bleaching, *Journal of Wood Science*, 45(4), pp. 313–318. doi: 10.1007/bf00833496.
53. Hou, Y., Hou, C., Zhai, Y., Li, H., Chen, T., Fan, Y., Wang, H. and Wang, W. 2019. Enhancing the electrocatalytic activity of 2D micro-assembly Co_3O_4 nanosheets for Li–O_2 batteries by tuning oxygen vacancies and Co^{3+}/Co^{2+} ratio, *Electrochimica Acta*, 324, p. 134884. doi: 10.1016/j.electacta.2019.134884.
54. Houk, R. J. T., Tobey, S. L. and Anslyn, E. V. 2005. Abiotic guanidinium receptors for anion molecular recognition and sensing, *Topics in Current Chemistry*, 255, pp. 199–229. doi: 10.1007/b101167.
55. Hua, F., Swihart, M. T. and Ruckenstein, E. 2005. Efficient surface grafting of luminescent silicon quantum dots by photoinitiated hydrosilylation, *Langmuir*, 21(13), pp. 6054–6062. doi: 10.1021/la0509394.
56. Islam, T., Hasan, M.M., Akter, S.S., Alharti, N.H., Karim, M.R., Aziz, M.A., Hossain, M.D. and Ahammad, A.J.S. 2020. Fabrication of Ni–Co-Based Heterometallo-Supramolecular Polymer Films and the Study of Electron Transfer Kinetics for the Nonenzymatic Electrochemical Detection of Nitrite, *ACS Applied Polymer Materials*, 2(2), pp. 273–284. doi: 10.1021/acsapm.9b00797.
57. Itoh, H., Nagata, A., Toyomasu, T., Sakiyama, T., Nagai, T., Saeki, T. and Nakanishi, K. 1995. Adsorption of β-Lactoglobulin onto the Surface of Stainless Steel Particles, *Bioscience, Biotechnology, and Biochemistry*, 59(9), pp. 1648–1651. doi: 10.1271/bbb.59.1648.
58. Jack, K. S., Vizcarra, T.G. and Trau, M. 2007. Characterization and Surface Properties of Amino-Acid-Modified Carbonate-Containing Hydroxyapatite Particles Kevin, *Langmuir*, pp. 12233–12242. Available at: https://doi.org/10.1021/la701848c.
59. Jeon, H. S., Jee, M.S., Kim, H., Ahn, S.J., Hwang, Y.J. and Min, B.K. 2015. Simple Chemical Solution Deposition of Co_3O_4 Thin Film Electrocatalyst for Oxygen Evolution Reaction, *ACS Applied Materials and Interfaces*, 7(44), pp. 24550–24555. doi: 10.1021/acsami.5b06189.
60. Jiang, Y., Wu, Y., Xie, B., Xie, Y. and Zhou, Y. 2002. Moderate temperature synthesis of nanocrystalline Co_3O_4 via gel hydrothermal oxidation, *Materials Chemistry and Physics*, 74(2), pp. 234–237. doi: 10.1016/s0254-0584(01)00463-1.
61. Jilani, B. S., Nayaka, M., Pari, M., Devendrachari, M.C. and Venegopala, K. 2020. Cobalt (II) tetra methyl-quinoline oxy bridged phthalocyanine carbon nano particles modified glassy carbon electrode for sensing nitrite: A voltammetric study, *Materials Chemistry and Physics*, 239(August), p. 121920. doi: 10.1016/j.matchemphys.2019.121920.
62. Kim, D. H., Kwak, D.H., Han, S.B., Park, H.S., Park, J.Y., Won, J.E., Ma, K.B., Yun, S.H., Kwon, S.H., Koh, M.H. and Park, K.W. 2018. The role of arginine as nitrogen doping and carbon source for enhanced oxygen reduction reaction, *International Journal of Hydrogen Energy*, 43(3), pp. 1479–1488. doi: 10.1016/j.ijhydene.2017.11.173.

63. Kittaka, S. and Morimoto, T. 1980. Isoelectric point of metal oxides and binary metal oxides having spinel structure, *Journal of colloid and interface science*, 75(2), pp. 398–403. doi: 10.1016/0021-9797(80)90464-6.
64. Kolesov, B. A. 2006. Raman spectra of single H_2O molecules isolated in cavities of crystals, *Journal of Structural Chemistry*, 47(1), pp. 21–34. doi: 10.1007/s10947-006-0261-4.
65. Kroupova, H., Machova, J. and Svobodova, Z. 2005. Nitrite influence on fish: A review, *Veterinarni Medicina*, 50(11), pp. 461–471. doi: 10.17221/5650-VETMED.
66. Kumar, S. and Rai, S. B. 2010. Spectroscopic studies of L-arginine molecule, *Indian Journal of Pure and Applied Physics*, 48(4), pp. 251–255.
67. Kuo, C. C., Liu, C.C., He, S.C., Chang, J.T. and He, J.L. 2011. The influences of thickness on the optical and electrical properties of dual-ion-beam sputtering-deposited molybdenum-doped zinc oxide layer, *Journal of Nanomaterials*, 2011. doi: 10.1155/2011/140697.
68. Lamine, M., Fall, B., Diedhiou, I., Dieye, E.H., Lo, M., Diaw, A.K.D., Sall, D.G., Raouafi, N. and Fall, M. 2020. Toxicity and Electrochemical Detection of Lead, Cadmium and Nitrite Ions by Organic Conducting Polymers : A Review, *Chemistry Africa*, (0123456789). doi: 10.1007/s42250-020-00157-0.
69. Larkin, P. 2011. IR and Raman Spectra-Structure Correlations: Characteristic Group Frequencies, in Larkin, P. (ed.) *IR and Raman Spectroscopy Principles and Spectral Interpretation*. Elsevier, pp. 73–115. doi: https://doi.org/10.1016/B978-0-12-386984-5.10006-0.
70. Lewis, C., Hughes, B.H., Vasquez, M., Wall, A.M., Northrup, V.L., Witzleb, T.J., Billiot, E.J., Fang, Y., Billiot, F.H. and Morris, K.F. 2016. Effect of pH on the Binding of Sodium, Lysine, and Arginine Counterions to l-Undecyl Leucinate Micelles, *Journal of Surfactants and Detergents*, 19(6), pp. 1175–1188. doi: 10.1007/s11743-016-1875-y.
71. Lewis, C. A. and Wolfenden, R. 2014. The nonenzymatic decomposition of guanidines and amidines, *Journal of the American Chemical Society*, 136(1), pp. 130–136. doi: 10.1021/ja411927k.
72. Li, H., Meininger, C. J. and Wu, G. 2000. Rapid determination of nitrite by reversed-phase high-performance liquid chromatography with fluorescence detection, *Journal of Chromatography B: Biomedical Sciences and Applications*, 746(2), pp. 199–207. doi: 10.1016/S0378-4347(00)00328-5.
73. Li, M., Yao, J., Liu, Y., Wu, X., Yu, Y., Xing, B., Yan, X., Guo, W., Tan, M., Sha, J. and Wang, Y. 2020. Air stable and reversible n-type surface functionalization of MoS_2 monolayer using Arg and Lys amino acids, *Journal of Materials Chemistry C*. doi: 10.1039/d0tc02939d.
74. Li, P., Ding, Y., Wang, A., Zhou, L., Wei, S., Zhou, Y., Tang, Y., Chen, Y., Cai, C. and Lu, T. 2013. Self-assembly of tetrakis (3-trifluoromethylphenoxy) phthalocyaninato cobalt(II) on multiwalled carbon nanotubes and their amperometric sensing application for nitrite, *ACS Applied Materials and Interfaces*, 5(6), pp. 2255–2260. doi: 10.1021/am400152k.
75. Liu, H., Guo, K., Lv, J., Gao, Y., Duan, C., Deng, L. and Zhu, Z. 2017. A novel nitrite biosensor based on the direct electrochemistry of horseradish peroxidase immobilized on porous Co_3O_4 nanosheets and reduced graphene oxide composite modified electrode, *Sensors and Actuators, B: Chemical*, 238, pp. 249–256. doi: 10.1016/j.snb.2016.07.073.
76. Lu, L. 2019. Highly sensitive detection of nitrite at a novel electrochemical sensor based on mutually stabilized Pt nanoclusters doped CoO nanohybrid, *Sensors and Actuators, B: Chemical*, 281, pp. 182–190. doi: 10.1016/j.snb.2018.10.074.
77. Lu, S., Hummel, M., Kang, S. and Gu, Z. 2020. Selective Voltammetric Determination of Nitrite Using Cobalt Phthalocyanine Modified on Multiwalled Carbon Nanotubes, *Journal*

of The Electrochemical Society, 167(4), p. 046515. doi: 10.1149/1945-7111/ab7982.
78. Lu, S., Yang, C. and Nie, M. 2017. Hydrothermal synthesized urchin-like nickel-cobalt carbonate hollow spheres for sensitive amperometric detection of nitrite, *Journal of Alloys and Compounds*, 708, pp. 780–786. doi: 10.1016/j.jallcom.2017.03.059.
79. Lu, Z., Shanli, Y., Qiong, Y., Shenglian, L., Chengbin, L. and Yanhong, T. 2013. A glassy carbon electrode modified with graphene, gold nanoparticles and chitosan for ultrasensitive determination of lead(II), *Microchimica Acta*, 180(7–8), pp. 555–562. doi: 10.1007/s00604-013-0959-x.
80. Lynne, D. and Kay, C. 1982. *G. Dillard, Chairman *. Virginia Polytechnic Institute and State University. Available at: http://hdl.handle.net/10919/88722.
81. Ma, Y., Song, X., Ge, X., Zhang, H., Wang, G., Zhang, Y. and Zhao, H. 2017. In situ growth of α-Fe_2O_3 nanorod arrays on 3D carbon foam as an efficient binder-free electrode for highly sensitive and specific determination of nitrite, *Journal of Materials Chemistry A*, 5(9), pp. 4726–4736. doi: 10.1039/c6ta10744c.
82. Mansournia, M. and Rakhshan, N. 2016. Amine ligand-based hydrothermal synthesis of Co_3O_4 nanoparticles, characterization and magnetic study, *Journal of Molecular Structure*, 1125, pp. 714–720. doi: 10.1016/j.molstruc.2016.07.080.
83. Matsuda, H. and Ayabe, Y. 1955. Zur Theorie der Randles-Sevčikschen Kathodenstrahl-Polarographie, *Zeitschrift für Elektrochemie, Berichte der Bunsengesellschaft für physikalische Chemie*, 59(6), pp. 494–503.
84. McCormick, R. M. and Karger, B. L. 1980. Guidelines For Data Acquisition And Data Quality Evaluation In Environmental Chemistry, *Analytical Chemistry*, 52(14), pp. 2242–2249. doi: 10.1021/ac50064a004.
85. Meng, Z., Liu, B., Zheng, J., Sheng, Q. and Zhang, H. 2011. Electrodeposition of cobalt oxide nanoparticles on carbon nanotubes, and their electrocatalytic properties for nitrite electrooxidation', *Microchimica Acta*, 175(3–4), pp. 251–257. doi: 10.1007/s00604-011-0688-y.
86. Morishita, M., Ochial, S., Kakeya, T., Ozaki, T., Kawabe, Y., Watada, M. and Sakai, T. 2009. Structural Analysis Using Synchrotron XRD and XAFS for Cobalt Oxyhydroxides Heat-Treated under Sodium Hydroxide Solution for Nickel Hydroxide Electrode, *Journal of The Electrochemical Society*, 156(5), p. A366. doi: 10.1149/1.3079421.
87. Mubarak, A. T., Mohamed, A.A., Fawy, K.F. and Al-Shihry, A.S. 2007. A novel kinetic determination of nitrite based on the perphenazine-bromate redox reaction, *Microchimica Acta*, 157(1–2), pp. 99–105. doi: 10.1007/s00604-006-0661-3.
88. Najem, R. M. 2004. *Chapter 3 Amperometric electrodes for enantioanalysis*. University of Pretoria. Available at: https://repository.up.ac.za/bitstream/handle/2263/24676/03chapter3.pdf?sequence=4 (Accessed: 27 September 2018).
89. Nakaoka, K., Nakayama, M. and Ogura, K. 2002. Electrochemical Deposition of Spinel-Type Cobalt Oxide from Alkaline Solution of Co[sup 2+] with Glycine, *Journal of The Electrochemical Society*, 149(3), p. C159. doi: 10.1149/1.1446871.
90. Nguyen, T. Q. and Breitkopf, C. 2018. Determination of Diffusion Coefficients Using Impedance', 165(14), pp. 826–831. doi: 10.1149/2.1151814jes.
91. Ouyang, C., Wang, X. and Wang, S. 2015. Phosphorus-doped CoS_2 nanosheet arrays as ultra-efficient electrocatalysts for the hydrogen evolution reaction, *Chemical Communications*, 51(75), pp. 14160–14163. doi: 10.1039/c5cc05541e.
92. Palmer, M., Masikini, M., Jiang, L.W., Wang, J.J., Cummings, F., Chamier, J., Inyang, O. and Chowdhury, M. 2021. Enhanced electrochemical glucose sensing performance of CuO:NiO mixed oxides thin film by plasma assisted nitrogen doping, *Journal of Alloys and Compounds*, 853, p. 156900. doi: https://doi.org/10.1016/j.jallcom.2020.156900.
93. Pan, H., Wu, D., Huang, X., Xie, K., He, B., Lu, Z., Liu, P., Cheng, J., Zhao, X., Masa, J. and Chen, X. 2019. Microwave-Assisted Synthesis of Co/CoO_x Supported on Earth-

Abundant Coal-Derived Carbon for Electrocatalysis of Oxygen Evolution Microwave-Assisted Synthesis of Co/CoO_x Supported on Earth-Abundant Coal-Derived Carbon for Electrocatalysis of Oxygen, *Journal of The Electrochemical Society,* 166(8), pp. F479-F486. doi: 10.1149/2.0281908jes.

94. Park, J., An, K., Hwang, Y., Park, J.G., Noh, H.J., Kim, J.Y., Park, J.H., Hwang, N.M. and Hyeon, T. 2004. Ultra-large-scale syntheses of monodisperse nanocrystals, *Nature Materials*, 3(12), pp. 891–895. doi: 10.1038/nmat1251.
95. Patel, D., Chang, Y. and Lee, G. H. 2009. Amino acid functionalized magnetite nanoparticles in saline solution, *Current Applied Physics*, 9(1 SUPPL.), pp. S32–S34. doi: 10.1016/j.cap.2008.08.027.
96. Qiu, W., Tanaka, H., Gao, F., Wang, Q. and Huang, M. 2019. Synthesis of porous nanododecahedron Co_3O_4/C and its application for nonenzymatic electrochemical detection of nitrite, *Advanced Powder Technology*, 30(10), pp. 2083–2093. doi: 10.1016/j.apt.2019.06.022.
97. Rao, G. R. and Nozoye, H. 2003. Photoemission study of the reaction of CO with Sm films on the Ru(001) surface, *Surface Review and Letters*, 10(6), pp. 917–923. doi: 10.1142/S0218625X03005700.
98. De Rivas, B., Lopez-Fonseca, R., Jimenez-Gonzalez, C., Gutierrez-Ortiz, J.I. 2011. Synthesis, characterisation and catalytic performance of nanocrystalline Co_3O_4 for gas-phase chlorinated VOC abatement, *Journal of Catalysis*, 281(1), pp. 88–97. doi: 10.1016/j.jcat.2011.04.005.
99. Rizvi, M. A. 2015. Complexation modulated redox behavior of transition metal systems (review), *Russian Journal of General Chemistry*, 85(4), pp. 959–973. doi: 10.1134/S1070363215040337.
100. Rossi, L. M., Costa, N.J.S., Silva, F.P. and Wojcieszak, R. 2014. Magnetic nanomaterials in catalysis: Advanced catalysts for magnetic separation and beyond, *Green Chemistry*, 16(6), pp. 2906–2933. doi: 10.1039/c4gc00164h.
101. Roth, W. L. 1964. The magnetic structure of Co_3O_4, *Journal of Physics and Chemistry of Solids*, 25(1), pp. 1–10. doi: 10.1016/0022-3697(64)90156-8.
102. Rumplecker, A., Kleitz, F., Salabas, E.L. and Schuth, F. 2007. Hard templating pathways for the synthesis of nanostructured porous Co_3O_4, *Chemistry of Materials*, 19(3), pp. 485–496. doi: 10.1021/cm0610635.
103. Salimi, A., Mamkhezri, H., Hallaj, R. and Soltanian, S. 2008. Electrochemical detection of trace amount of arsenic(III) at glassy carbon electrode modified with cobalt oxide nanoparticles, *Sensors and Actuators, B: Chemical*, 129(1), pp. 246–254. doi: 10.1016/j.snb.2007.08.017.
104. Salimi, A., Hallaj, R., Mamkhezri, H. and Hosaini, S.M.T. 2008. Electrochemical properties and electrocatalytic activity of FAD immobilized onto cobalt oxide nanoparticles: Application to nitrite detection, *Journal of Electroanalytical Chemistry*, 619–620(1–2), pp. 31–38. doi: 10.1016/j.jelechem.2008.03.003.
105. Sandford, C., Edwards, M., Klunder, K., Hickey, D.P., Li, M., Barman, K., Sigman, M., White, H. and Minteer, S. 2019. A synthetic chemist's guide to electroanalytical tools for studying reaction mechanisms, *Chemical Science*, pp. 6404–6422. doi: 10.1039/c9sc01545k.
106. Santos, A. R., Blundell, R. K. and Licence, P. 2015. XPS of guanidinium ionic liquids: A comparison of charge distribution in nitrogenous cations, *Physical Chemistry Chemical Physics*, 17(17), pp. 11839–11847. doi: 10.1039/c5cp01069a.
107. Santos, W. J. R., Sousa, A.L., Luz, R.C.S., Damos, F.S., Kubota, L.T., Tanaka, A.A. and Tanaka, S.M.C.N. 2006. Amperometric sensor for nitrite using a glassy carbon electrode modified with alternating layers of iron(III) tetra-(N-methyl-4-pyridyl)-porphyrin and cobalt(II) tetrasulfonated phthalocyanine, *Talanta*, 70(3), pp. 588–594. doi: 10.1016/j.talanta.2006.01.023.

108. Saranya, S., Justin, S.J.S., Solomon, R.V. and Wilson, P. 2018. L-arginine directed and ultrasonically aided growth of nanocrystalline hydroxyapatite particles with tunable morphology, *Colloids and Surfaces A: Physicochemical and Engineering Aspects*, 538, pp. 270–279. doi: 10.1016/j.colsurfa.2017.11.012.
109. Sayato, Y. 1989. WHO Guidelines for Drinking-Water Quality, *Eisei kagaku*, 35(5), pp. 307–312. doi: 10.1248/jhs1956.35.307.
110. Schmidt, H. 1981. Chemistry of material preparation by the sol-gel process, *Journal of Non-Crystalline Solids*, 100(1988), pp. 51–64. Available at: https://doi.org/10.1016/0022-3093(88)90006-3.
111. Schumacher, L.C., Holzhueter, I.B., Hill, I.R. and Dignam, M.J. 1990. Semiconducting and electrocatalytic properties of sputtered cobalt oxide films, *Electrochimica Acta*, 35(6), pp. 975–984. doi: 10.1016/0013-4686(90)90030-4.
112. Schwartz, R.W. 1997. Chemical Solution Deposition of Perovskite Thin Films, *Chemistry of Materials*, 9(11), pp. 2325–2340. doi: 10.1021/cm970286f.
113. Schwartz, R. W., Voigt, J.A., Tuttle, B.A., Payne, D.A., Reichert, T.L. and DaSalla, R.S. 1997. Comments on the effects of solution precursor characteristics and thermal processing conditions on the crystallization behavior of sol-gel derived lead zirconate titanate thin films, *Journal of Materials Research*, 12(2), pp. 444–456. doi: 10.1557/JMR.1997.0066.
114. Sharma, S. 2018. Glassy Carbon: A promising material for microand nanomanufacturing, *Materials*, 11(10). doi: 10.3390/ma11101857.
115. Shi, W., Yang, W., Li, Qi., Gao, S., Shang, P. and Shang, J.K. 2012. The synthesis of nitrogen/sulfur co-doped TiO_2 nanocrystals with a high specific surface area and a high percentage of {001} facets and their enhanced visible-light photocatalytic performance, *Nanoscale Research Letters*, 7, pp. 1–9. doi: 10.1186/1556-276X-7-590.
116. Shinde, V. R., Mahadik, S.B., Gujar, T.P., Lokhande, C.D. 2006. Supercapacitive cobalt oxide (Co_3O_4) thin films by spray pyrolysis, *Applied Surface Science*, 252(20), pp. 7487–7492. doi: 10.1016/j.apsusc.2005.09.004.
117. Shivakumar, M., K L, N., Manjappa, S. and Dharmaprakash, M.S. 2017. Electrochemical Detection of Nitrite Using Glassy Carbon Electrode Modified with Silver Nanospheres (AgNS) Obtained by Green Synthesis Using Pre-hydrolysed Liquor, *Electroanalysis*, 29(5), pp. 1434–1442. doi: 10.1002/elan.201600775.
118. Shrivastava, A. and Gupta, V. 2011. Methods for the determination of limit of detection and limit of quantitation of the analytical methods, *Chronicles of Young Scientists*, 2(1), p. 21. doi: 10.4103/2229-5186.79345.
119. Smirnova, A. L., Hu, Y-L., Zhang, L., Aindow, M., Menard, P., Singh, P., Goberman, D., Shaw, L., Wan, X. and Rhine, W. 2019. Synthesis of Novel Electrode Materials Using Supercritical Fluids, *ECS Transactions*, 19(21), pp. 9–21. doi: 10.1149/1.3242512.
120. Long, D.A. 2004. Infrared and Raman characteristic group frequencies: Tables and Charts 3rd ed. *Journal of Raman Spectroscopy*, 35(10), p. 905. doi: 10.1002/jrs.1238.
121. Su, L., Cui, X., He, T., Zeng, L., Tian, H., Song, Y. Qi, K. and Xia, B.Y. 2019. Surface reconstruction of cobalt phosphide nanosheets by electrochemical activation for enhanced hydrogen evolution in alkaline solution, *Chemical Science*, 10(7), pp. 2019–2024. doi: 10.1039/C8SC04589E.
122. Sudha, V., Krishnamoorthy, K., Kumar, S.M.S. and Thangamuthu, R. 2018. Copper oxide nanosheet modified electrodes for simultaneous determination of environmentally hazardous anions, *Journal of Alloys and Compounds*, 764, pp. 959–968. doi: 10.1016/j.jallcom.2018.06.077.
123. Sudha, V., Mohanty, S. A. and Thangamuthu, R. 2018. Facile synthesis of Co_3O_4 disordered circular sheets for selective electrochemical determination of nitrite, *New Journal of Chemistry*, 42(14), pp. 11869–11877. doi: 10.1039/c8nj02639d.
124. Sudha, V., Senthil Kumar, S. M. and Thangamuthu, R. 2018. Simultaneous

electrochemical sensing of sulphite and nitrite on acid-functionalized multi-walled carbon nanotubes modified electrodes, *Journal of Alloys and Compounds*, 749, pp. 990–999. doi: 10.1016/j.jallcom.2018.03.287.
125. Sun, L., Li, H., Ren, L. and Hu, C. 2009. Synthesis of Co_3O_4 nanostructures using a solvothermal approach, *Solid State Sciences*, 11(1), pp. 108–112. doi: 10.1016/j.solidstatesciences.2008.05.013.
126. Sun, X., Wang, S., Zhang, X., Chen, J.P., Li, X., Gao, B. and Ma, Y. 2009. Spectroscopic study of Zn^{2+} and Co^{2+} binding to extracellular polymeric substances (EPS) from aerobic granules, *Journal of Colloid And Interface Science*, 335(1), pp. 11–17. doi: 10.1016/j.jcis.2009.03.088.
127. Tsuchida, R. 1938. Absorption Spectra of Co-ordination Compounds II, *Bulletin of the Chemical Society of Japan*, 13(6), pp. 436–450. doi: 10.1246/bcsj.13.436.
128. Wachter, A. 1945. Sodium Nitrite as Corrosion Inhibitor for Water, *Industrial & Engineering Chemistry*, 37(8), pp. 749–751. doi: 10.1021/ie50428a021.
129. Wang, F. and Hu, S. 2009. Electrochemical sensors based on metal and semiconductor nanoparticles, *Microchimica Acta*, 165(1–2), pp. 1–22. doi: 10.1007/s00604-009-0136-4.
130. Wang, J., Gao, R., Zhou, D., Chen, Z., Wu, Z., Schumacher, G., Hu, Z. and Liu, X. 2017. Boosting the electrocatalytic activity of Co_3O_4 nanosheets for a Li-O_2 Battery through modulating inner oxygen vacancy and exterior Co^{3+}/Co^{2+} ratio, *ACS Catalysis*, 7(10), pp. 6533–6541. doi: 10.1021/acscatal.7b02313.
131. Wang, J. and Hui, N. 2017. A nanocomposite consisting of flower-like cobalt nanostructures, graphene oxide and polypyrrole for amperometric sensing of nitrite, *Microchimica Acta*, 184(7), pp. 2411–2418. doi: 10.1007/s00604-017-2247-7.
132. Wang, J. J., Hu, Y., Toth, R., Fortunato, G. and Braun, A. 2016. A facile nonpolar organic solution process of a nanostructured hematite photoanode with high efficiency and stability for water splitting, *Journal of Materials Chemistry A*, 4(8), pp. 2821–2825. doi: 10.1039/c5ta06439b.
133. Wang, Q. H., Yu, L.J., Liu, Y., Lin, L., Lu, R.G., Zhu, J.P., He, L. and Lu, Z.L. 2017. Methods for the detection and determination of nitrite and nitrate: A review, *Talanta*, 165, pp. 709–720. doi: 10.1016/j.talanta.2016.12.044.
134. Wang, Y., Laborda, E. and Compton, R. G. 2012. Electrochemical oxidation of nitrite: Kinetic, mechanistic and analytical study by square wave voltammetry, *Journal of Electroanalytical Chemistry*, 670, pp. 56–61. doi: 10.1016/j.jelechem.2012.02.016.
135. Willis, B. 2003. Fundamentals of Microsystems Packaging, *Soldering & Surface Mount Technology*, 15(1), doi: 10.1108/ssmt.2003.21915aae.006.
136. Wolfenden, R., Lewis Jr, C.A., Yuan, Y. and Carter Jr., C.W. 2015. Temperature dependence of amino acid hydrophobicities, *Proceedings of the National Academy of Sciences of the United States of America*, 112(24), pp. 7484–7488. doi: 10.1073/pnas.1507565112.
137. Wu, S., Cao, H., Yin, S., Liu, X. and Zhang, X. 2009. Amino acid-assisted hydrothermal synthesis and photocatalysis of SnO_2 nanocrystals, *Journal of Physical Chemistry C*, 113(41), pp. 17893–17898. doi: 10.1021/jp9068762.
138. Xiao, Z., Wang, Y., Huang, Y.C., Wei, Z., Dong, C.L., Ma, J., Shen, S., Li, Y. and Wang, S. 2017. Filling the oxygen vacancies in Co_3O_4 with phosphorus: An ultra-efficient electrocatalyst for overall water splitting, *Energy and Environmental Science*, 10(12), pp. 2563–2569. doi: 10.1039/c7ee01917c.
139. Xu, B., Jacobs, M.I., Kostko, O. and Ahmed, M. 2017. Guanidinium Group Remains Protonated in a Strongly Basic Arginine Solution, *ChemPhysChem*, 18(12), pp. 1503–1506. doi: 10.1002/cphc.201700197.
140. Xu, R., Wang, J., Li, Q., Sun, G., Wang, E., Li, S., Gu, J. and Ju, M. 2009. Porous cobalt oxide (Co_3O_4) nanorods: Facile syntheses, optical property and application in lithium-ion batteries, *Journal of Solid State Chemistry*, 182(11), pp. 3177–3182. doi:

10.1016/j.jssc.2009.08.033.
141. Yilong, Z., Dean, Z. and Daoliang, L. 2015. Electrochemical and other methods for detection and determination of dissolved nitrite: A review, *International Journal of Electrochemical Science*, 10(2), pp. 1144–1168.
142. Yu, M., Wang, Z., Hou, C., Wang, Z., Liang, C., Zhao, C., Tong, Y., Lu, X. and Yang, S. 2017. Nitrogen-Doped Co_3O_4 Mesoporous Nanowire Arrays as an Additive-Free Air-Cathode for Flexible Solid-State Zinc–Air Batteries, *Advanced Materials*, 29(15), pp. 1–7. doi: 10.1002/adma.201602868.
143. Zare, H. R., Memarzadeh, F., Gorji, A. and Ardakani, M.M. 2005. Iodide-selective membrane electrode based on salophen complex of cobalt (III), *Journal of the Brazilian Chemical Society*, 16(3 B), pp. 571–577. doi: 10.1590/S0103-50532005000400013.
144. Zhan, S., Zhang, H., Mi, X., Zhao, Y., Hu, C. and Lyu, L. 2020. Efficient Fenton-like Process for Pollutant Removal in Electron-Rich / Poor Reaction Sites Induced by Surface Oxygen Vacancy over Cobalt-Zinc Oxides, *Environmental Science & Technology,* 54(13), pp. 8333-8343. doi: 10.1021/acs.est.9b07245.
145. Zhao, K., Song, H., Zhuang, S., Dai, L., He, P. and Fang, Y. 2007. Determination of nitrite with the electrocatalytic property to the oxidation of nitrite on thionine modified aligned carbon nanotubes, *Electrochemistry Communications*, 9(1), pp. 65–70. doi: 10.1016/j.elecom.2006.07.001.
146. Zhao, Z., Zhang, J., Wang, W., Sun, Y., Li, P., Hu, J., Chen, L. and Gong, W. 2019. Synthesis and electrochemical properties of Co_3O_4-rGO/CNTs composites towards highly sensitive nitrite detection, *Applied Surface Science*, 485, pp. 274–282. doi: 10.1016/j.apsusc.2019.04.202.
147. Zheng, Y., Liu, Y., Zhou, H., Huang, W. and Pu, Z. 2017. Complete combustion of methane over Co_3O_4 catalysts: Influence of pH values, *Journal of Alloys and Compounds*, 734, pp. 112-120. doi: 10.1016/j.jallcom.2017.11.008.
148. Zheng, Y., Yu, Y., Zhou, H., Huang, W. and Pu, Z. 2020. Combustion of lean methane over Co_3O_4 catalysts prepared with different cobalt precursors, *RSC Advances*, 10(8), pp. 4490–4498. doi: 10.1039/c9ra09544f.
149. Zhu, G., Zhu, X., Fan, Q. and Wan, X. 2011. Raman spectra of amino acids and their aqueous solutions, *Spectrochimica Acta - Part A: Molecular and Biomolecular Spectroscopy*, 78(3), pp. 1187–1195. doi: 10.1016/j.saa.2010.12.079.
150. Zhu, Z., Lu, G., Zhang, Z., Guo, Y., Guo, Y. and Wang, Y. 2013. Highly active and stable Co_3O_4/ZSM-5 catalyst for propane oxidation: Effect of the preparation method, *ACS Catalysis*, 3(6), pp. 1154–1164. doi: 10.1021/cs400068v.

APPENDIX A: Optimization of experimental conditions

Layer study

This study was conducted to determine the number of deposited layers that would promote excellent electro-catalytic activity of Co_3O_4 thin film towards nitrite oxidation based on response current. We discovered that as the number of deposited layers was varied from one to six (i.e., increase in film thickness), the peak current increased to a maximum (0.45 mA) then suddenly decreased. This trend was found to be very much similar to that observed on the variation of the electrical resistivity of Mo-doped ZnO layer with film thickness (Kuo *et al.*, 2011). Thus, the parabolic trend in peak current was attributed to a corresponding change in electrical resistivity of the deposited films. These observations were consistent even after treatment of pristine Co_3O_4 thin film with water and L-Arginine.

Effect of dipping time and pH

Co_3O_4 thin film was dipped into L-Arginine solution under normal temperature and pressure for various times. The outcome of the dipping test revealed that anodic peak current increased with dipping time as more and more time was allowed for L-Arginine to interact with the film surface and consequently improve its nitrite sensing properties. The effect of dipping pH on anodic peak current was investigated; however, no change in peak current with pH was observed. This was attributed to the repulsive interactions between Co_3O_4 (IEP ≈ 8 (Kittaka and Morimoto, 1980)) and L-Arginine (IEP = 10.75 (Saranya *et al.*, 2018)) as they have isoelectric point (IEP) values that are close to each other (i.e., chances for efficient physical adsorption of L-Arginine on Co_3O_4 are slim). The outcome of the dipping pH study suggests that L-Arginine will adsorb more strongly on the Co_3O_4 film surface through chemical interactions (chemisorption).

Effect of different treatment processes

Co_3O_4 thin film was treated in the presence of L-Arginine under hydrothermal, dipping, and reflux conditions to determine the treatment process which would promote excellent current response of the film towards nitrite electro-oxidation. We found that the film treated under hydrothermal conditions showed higher anodic peak current than those treated via the dipping and reflux processes due to more chemical interactions between L-Arginine and the film surface, which resulted from the high-temperature and pressure treatment. The hydrothermal treatment process was adopted for subsequent experiments.

Effect of hydrothermal treatment time

The influence of hydrothermal time on anodic peak current for L-Arginine/Co_3O_4/FTO was then investigated. The outcome of the study revealed that the peak current increased with hydrothermal treatment time until it reached a plateau after 24-hour treatment. This was expected as a longer treatment time entailed a higher probability for more L-Arginine attachments onto Co_3O_4 thin film, which would alter the electrode surface chemistry and raise its affinity for nitrite ion, thereby increasing the current signal. The plateau obtained after 24-h treatment was deemed to be the result of L-Arginine saturation at the film surface. 24 h was therefore selected as the optimum hydrothermal treatment time.

Effect of hydrothermal treatment temperature

The peak current for L-Arginine/Co_3O_4/FTO was further optimized with respect to hydrothermal treatment temperature. As the hydrothermal treatment temperature was raised from 20 to 60 ºC, a gentle increase in anodic peak current was observed. The peak current continued to rise more abruptly to a maximum within 60-90 ºC before dropping to 0.36 mA at 120 ºC. Itoh and co-authors (Itoh *et al.*, 1995) reported the temperature dependence of the adsorption of β-Lactoglobulin onto the surface of stainless steel nanoparticles in aqueous solution. Within 25-60 ºC, they observed no significant change in the amount of adsorbed β-Lactoglobulin, which increased with further increase in temperature to approximately 86 ºC.

This sudden rise in the amount of β-Lactoglobulin adsorbed was ascribed to thermal denaturation and aggregation of the protein. Similarly, the hydrophobicity of most amino acids increases with temperature (Wolfenden *et al.*, 2015). As the temperature of the hydrothermal medium was elevated, L-Arginine molecules became more hydrophobic and possibly aggregated in larger amount at the film surface. This facilitated more L-Arginine adsorption and resulted in high nitrite affinity and therefore increased anodic current signal. Also, some L-Arginine molecules slowly decomposed at 90 ºC to produce ammonia (nitrogen doping agent), as per Raman and XPS results. Thus, the maximum current at 90 ºC was assigned to the synergistic effect of L-Arginine functionalization and nitrogen implantation into Co_3O_4 lattice. However, the decline in anodic peak current after 90 ºC could be due to a great extent of L-Arginine decomposition. 90 ºC was the optimum value retained.

Effect of L-Arginine bulk concentration

The impact of L-Arginine concentration on the current response of L-Arginine/Co_3O_4/FTO towards nitrite electro-oxidation was confirmed. It was observed that the anodic peak current increased with L-Arginine bulk concentration up to a point of saturation at 0.15 M, beyond which no significant increase in peak current was detected. This was expected as an increase in L-Arginine bulk concentration would lead to greater uptake of L-Arginine on Co_3O_4 thin film, which in turn would maximize nitrite-sensing abilities of L-Arginine/Co_3O_4/FTO.

Effect of hydrothermal pH

Adjusting the pH can give control over the type of amino acid-surface interaction (Jack *et al.*, 2007). The hydrothermal pH played a major role in the stability of Co_3O_4 thin film and its interaction with L-Arginine. It was found that treatment at pH 2.5 caused complete leaching of Co_3O_4 thin film from FTO substrate. Cation exchange possibly occurred between Co^{2+} (or Co^{3+}) on the film surface and L-Arginine cations (net charge = +2) or H^+ ions, detaching Co_3O_4 film from the FTO glass. When the film was treated at pH 7.5, it leached to a much lesser degree owing to a decrease in the number of H^+ ions and positive net charge of L-Arginine (net charge = +1) with increasing pH. Hence, we were able to test this electrode for nitrite oxidation and compare its response current with those of Co_3O_4 thin films treated at pH 11 and 13.9. It was found that anodic peak current parabolically increased with the medium pH and attained its maximum value at pH 11. The zwitterionic form of L-Arginine (net charge = 0) was dominant at that pH (11), hence cation exchange was unlikely. Complexation of cobalt cations on the film surface by L-Arginine took place instead, which considerably minimized leaching losses and enriched L-Arginine in the film. At pH 13.9, the increased concentration of OH^- ions more likely decreased the adsorption efficiency of L-Arginine anions (net charge = -1) due to a competitive effect (Biswas *et al.*, 2007). This is reflected by the drop in current at pH 13.9. Hydrothermal pH 11 was used for further experimental studies.

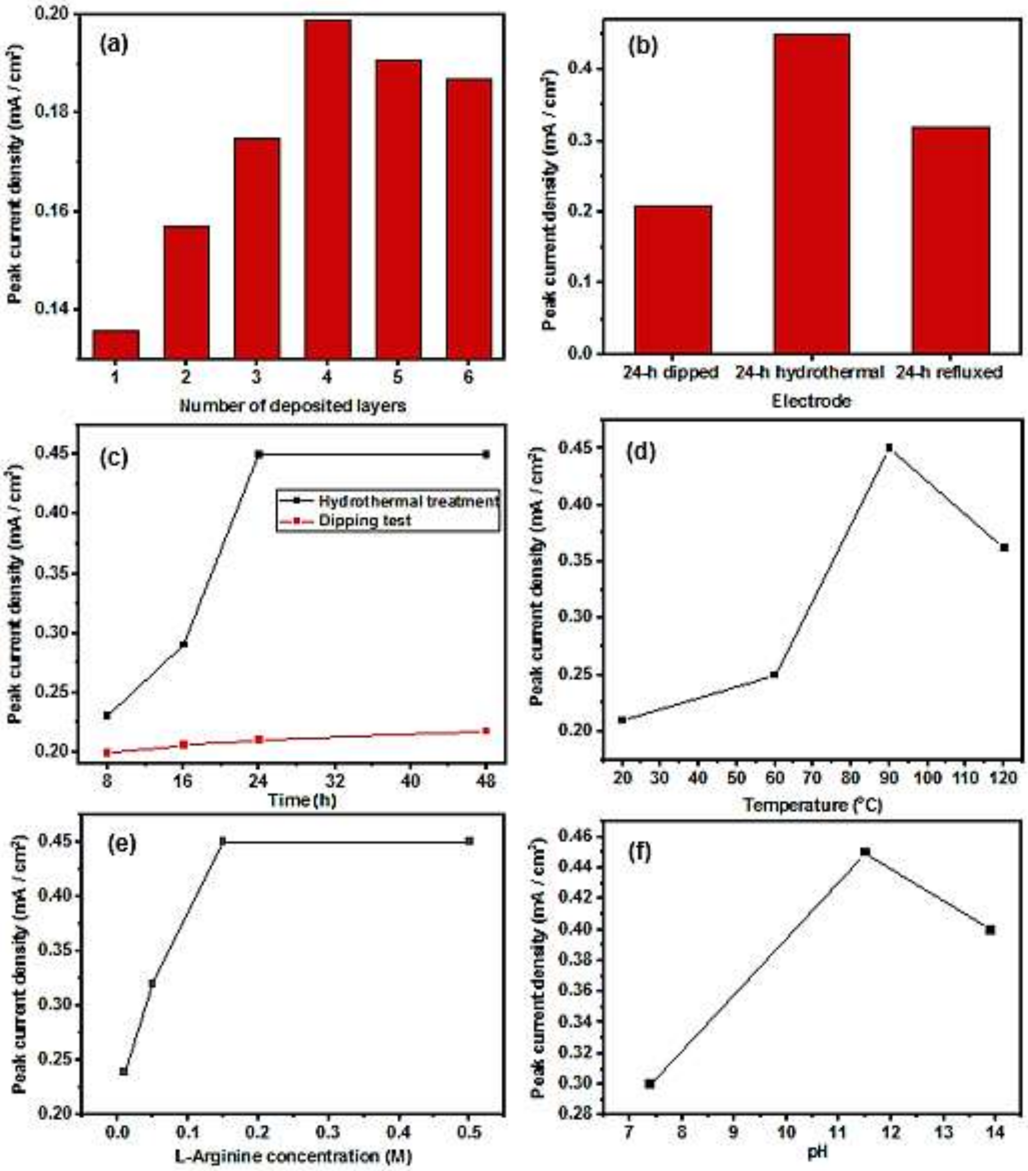

Figure A.1: Effect of (a) number of deposited layers varying from 1-6, (b) different treatment processes, (c) dipping vs hydrothermal treatment times (8, 16, 24, and 48 h), (d) hydrothermal treatment temperature (20, 60, 90, and 120 ºC), (e) L-Arginine concentration under hydrothermal conditions (0.01, 0.05, 0.15, and 0.5 M), and (f) hydrothermal pH (2.5, 7.5, 11, and 13.9) on anodic peak current

APPENDIX B: XRD patterns and cross-sectional SEM image of Co_3O_4 thin film

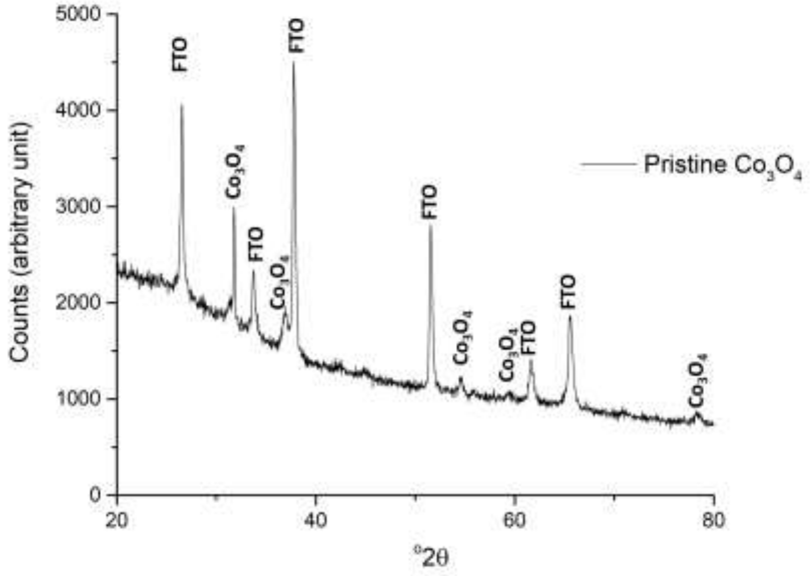

Figure B.1: XRD patterns of the MOD-derived Co_3O_4 Electrode

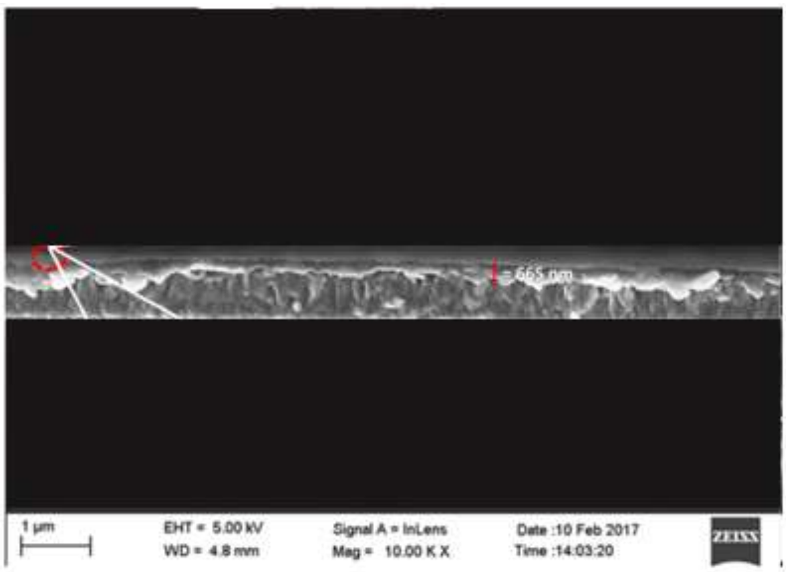

Figure B.2: Cross-sectional SEM image of the MOD-derived Co_3O_4 thin film

APPENDIX C: Surface atomic compositions, summary of the binding energy peak positions for Co 2*p* XPS analysis and their respective peak assignments, Tafel plot, and spectral weight ratio results of O1s and Co 2*p*$_{3/2}$ XPS.

Table C.1. Surface atomic compositions [%]

Electrode	**C 1*s***	**O1s**	**N1s**	**Co 2*p***
Co_3O_4/FTO	76.2	21.2	1.72	0.80
HT-Co_3O_4/FTO	77.6	19.1	1.98	1.31
L-Arginine/Co_3O_4/FTO	77.1	18.9	3.30	0.74

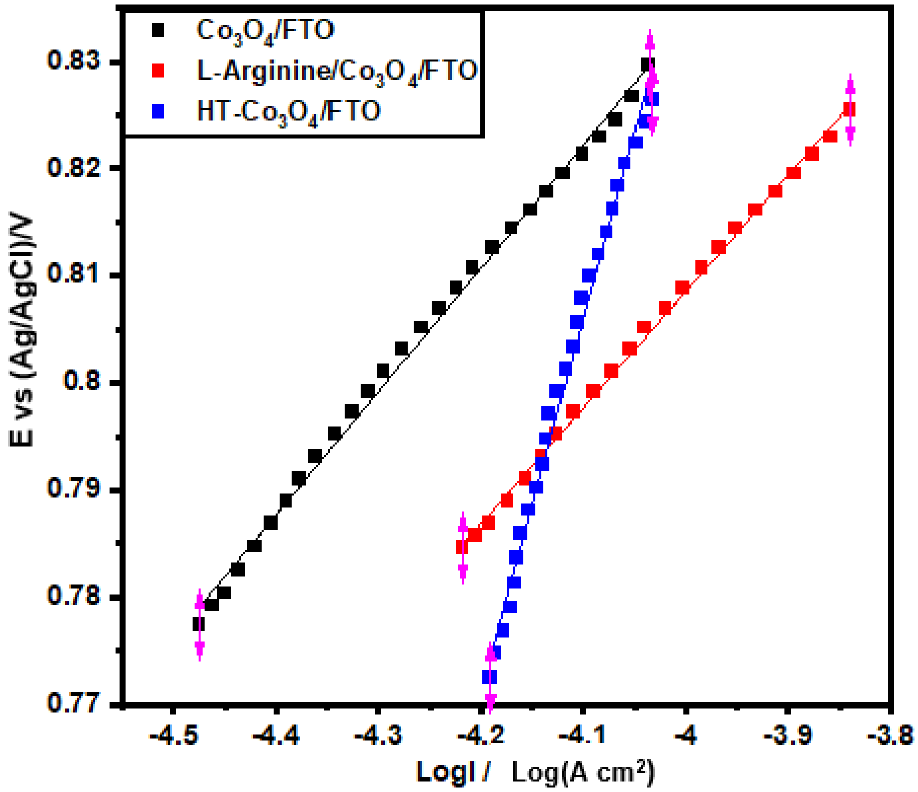

Figure C.1: Tafel plots of the L-Arginine/Co_3O_4/FTO, HT-Co_3O_4/FTO, and Co_3O_4/FTO electrodes

Table C.2. Summary of binding energy peak positions for Co 2*p*$_{3/2}$ XPS deconvolution for Co_3O_4/FTO, HT-Co_3O_4/FTO, and L-Arginine/Co_3O_4/FTO

Electrode	**Co 2*p*$_{3/2}$ eV**	**(Co 2*p*$_{1/2}$ – Co 2*p*$_{3/2}$) eV**	**$Co^{3+}(O_h)$* eV**	**Co^0 eV**	**$Co^{2+}(T_d)$* eV**	**$Co^{3+}(S)$* eV**	**$Co^{2+}(S)$ eV**	**$Co^{2+}(ss)$***	
Co_3O_4/FTO	779.1	15.1	779.1	-	780.2	781.7	780.9/782.6	784.0	788.3
HT-Co_3O_4/FTO	779.3	14.9	779.3	-	780.4	781.6	-	784.1	788.9
L-Arginine/ Co_3O_4/FTO	779.3	14.6	779.5	778.8	780.2	781.6	780.8/782.4	785.9	790.0
Reference	(Zhu *et al.*, 2013)	(Zhu *et al.*, 2013)	(Finkler *et al.*, 2018)	(Cho *et al.*, 2018)	(Finkler *et al.*, 2018)	(Zhan *et al.*, 2020)	(Cui *et al.*, 2018),(X. Sun *et al.*, 2009)	(Amri *et al.*, 2013)	(Amri *et al.*, 2013)

*ss: paramagnetic satellite peaks. *S: surface Co^{2+} and Co^{3+}.

Table C.3. O 1*s* and Co 2*p3/2* XPS spectral weight ratios for Co_3O_4/FTO, HT-Co_3O_4/FTO, and L-Arginine/Co_3O_4/FTO

Electrode	$O_{Latt}/(O_{Latt}+O_{Ads})$	O_{Ads}/O_{Latt}	Co^{3+}/Co^{2+}	Co^{0}/Co^{2+}	$(Co^{0}+Co^{3+})/Co^{2+}$	$(Co^{0}+Co^{2+})/Co^{3+}$
Co_3O_4/FTO	0.42	1.37	2.27	-	2.27	0.44
HT-Co_3O_4/FTO	0.72	0.38	2.70	-	2.70	0.37
L-Arginine/Co_3O_4/FTO	0.69	0.44	1.20	0.94	2.14	1.62

Page left blank intentionally.